# HIGH CURRENT, LONG-PULSE GYROTRON-BACKWARD-WAVE OSCILLATOR EXPERIMENTS

by

## Thomas Allen Spencer

A dissertation submitted in partial fulfillment
of the requirements for the degree of
Doctor of Philosophy
(Nuclear Engineering)
in The University of Michigan
1991

Doctoral Committee:

Professor Ronald M. Gilgenbach, Chairman
Associate Professor Mary Brake
Professor Terry Kammash
Assistant Professor Yasuo Kuga

19981202 042

# REPORT DOCUMENTATION PAGE

AFRL-SR-BL-TR-98-

*0750*

| 1. AGENCY USE ONLY (Leave Blank) | 2. REPORT DATE 1991 | 3. RE Final |
|---|---|---|

**4. TITLE AND SUBTITLE**
High Current, Long-Pulse, Gyrotron-Backward-Wave Oscillator Experiments

**5. FUNDING NUMBERS**

**6. AUTHORS**
Thomas Allen Spencer

**7. PERFORMING ORGANIZATION NAME(S) AND ADDRESS(ES)**
University of Michigan

**8. PERFORMING ORGANIZATION REPORT NUMBER**

**9. SPONSORING/MONITORING AGENCY NAME(S) AND ADDRESS(ES)**
AFOSR/NI
4040 Fairfax Dr, Suite 500
Arlington, VA 22203-1613

**10. SPONSORING/MONITORING AGENCY REPORT NUMBER**

**11. SUPPLEMENTARY NOTES**

**12a. DISTRIBUTION AVAILABILITY STATEMENT**
Approved for Public Release

**12b. DISTRIBUTION CODE**

**13. ABSTRACT** *(Maximum 200 words)*
None Included in the Document

**14. SUBJECT TERMS**

**15. NUMBER OF PAGES**

**16. PRICE CODE**

| 17. SECURITY CLASSIFICATION OF REPORT | 18. SECURITY CLASSIFICATION OF THIS PAGE | 19. SECURITY CLASSIFICATION OF ABSTRACT | 20. LIMITATION OF ABSTRACT |
|---|---|---|---|
| Unclassified | Unclassified | Unclassified | UL |

# HIGH CURRENT, LONG-PULSE GYROTRON-BACKWARD-WAVE OSCILLATOR EXPERIMENTS

by

**Thomas Allen Spencer**

A dissertation submitted in partial fulfillment
of the requirements for the degree of
Doctor of Philosophy
(Nuclear Engineering)
in The University of Michigan
1991

Doctoral Committee:

> Professor Ronald M. Gilgenbach, Chairman
> Associate Professor Mary Brake
> Professor Terry Kammash
> Assistant Professor Yasuo Kuga

This thesis is dedicated to my family.

# ACKNOWLEDGEMENTS

First of all, I thank my advisor, Dr. Ronald Gilgenbach, for all his help, confidence, and inspiration. If it hadn't been for his keen interest in my automobile repair abilities, I might be 'fissioning' somewhere in front of a computer screen at this very moment. I also thank him for the opportunity to become involved in the world of electron beams and microwaves which I knew little about when I first started my graduate studies at the University of Michigan. His exceptional insight and experimental intuition in microwaves and e-beams never ceases to amaze me. His endless enthusiasm for conducting experiments has been infectious, and his guidance towards the completion of this dissertation is greatly appreciated. It's too bad he can only spend part of his research time doing what he loves best: experimenting.

I thank Dr. Mary Brake, whose continuous smiling face is enough to brighten anyone's day (or perhaps drive them crazy during those early morning classes), for finding time to read this thesis without her eyes dropping out. I thank her for her enthusiasm in teaching the introductory plasma physics course which truly peaked my interest, and her helpful comments in the lab. I also thank her for those humorous moments (the phantom of the Macintosh), and for just being there to talk.

I thank Dr. Terry Kammash for his teachings of the advanced plasma physics courses (NE 676, NE671, and NE672), especially the lectures on absolute instabilities. It's sometimes hard to tell if he's joking, but he always makes time if you have any questions.

I thank Dr. Yasuo Kuga for reading this thesis on such short notice. I really appreciated his help when I was using the HP8510 ('Have you seen the cables,

# TABLE OF CONTENTS

# LIST OF FIGURES

xv

# LIST OF TABLES

# LIST OF APPENDICES

# CHAPTER I

# INTRODUCTION

## 1.1 Background and Description of Research

During the past few decades, considerable interest has been generated in the production of efficient, high-power, high frequency (centimeter, millimeter, and submillimeter) coherent electromagnetic sources. Several devices exist in which coherent microwaves can be generated, such as the relativistic magnetron [Gra87], klystrons [Mil82], gyro-klystrons [Law91], magnetically insulated line oscillators (MILOs), virtual cathode oscillators (VIRCATORS) [Sul87, Tho87], backward wave oscillators (BWOs) [Kan79, Lei86], electron cyclotron resonance masers [Hir77], the cusptron [Kuo88], as well as many others. The class of electron cyclotron resonance masers includes the peniotron [Bai87], the gyrotron which is defined as having a large phase velocity ($\beta_{ph}$ >>1) [And78, Chu81, Fly77, Hir79], the cyclotron autoresonance maser (CARM) which is defined as device in which the phase velocity is approximately the speed of light ($\beta_{ph}$ ~1) [Bek87, Lin87, Che89, Wan89, Kho90, Cho91] and the gyrotron-backward-wave oscillator (gyro-BWO) which is defined as a device with both the phase and group velocities less than zero. The above devices produce microwaves (for amplification and for oscillation) by the radiative emission from relativistic electrons in intense electron beams, which brings about the acronym MASER (Microwave Amplification by Stimulated Emission of Radiation). Radiation from the electrons occurs when the electrons undergo oscillations caused by the action of external forces, such as spatially and temporally uniform electromagnetic fields, periodic electromagnetic fields, or crossed electromagnetic fields [Lau87]. Coherent radiation exists when the radiation from the

1

electrons reinforces the initial electromagnetic radiation created by an oscillator, or by reinforcing an initial wave introduced into the system (in an amplifier).

The applications for coherent, high-power, high frequency radiation sources are seemingly endless. Some of the applications are: measuring energy levels of molecular states; measuring specific absorption of resonant frequencies, ion and electron cyclotron resonant heating (ICRH and ECRH), lower hybrid current drive for tokamaks (fusion), metal vapor lasers, bulk material heating, curing processes, high resolution radar, deep-space communication, and electronic warfare (EW). For many of these applications, it is necessary to deliver several hundreds of joules of energy [Gil80, Gil81, Lau87]. To achieve this goal, multimicrosecond pulselength, multimegawatt microwave sources are required.

A particular class of devices mentioned above, the electron cyclotron resonance masers, readily lend themselves as long-pulse, high power microwave sources, due to the electron cyclotron resonance instability when using relativistic electron beams. In the late 1950s, basic understanding of the physical processes of generating electromagnetic radiation at millimeter and submillimeter wavelengths from the electron cyclotron resonance maser were presented by Gapanov (USSR) [Gap59], Twiss (Australia) [Twi58], and Schneider (USA) [Sch59]. The first successful cyclotron resonance maser experiment is generally attributed to Hirshfield and Wachtel in 1964 [Hir64]. Since then, the cyclotron resonance maser has been shown to have the potential for efficient (30% and more), high power (kilowatts to gigawatts), high frequency microwave emission. Extensive theoretical analysis, including linear and non-linear analysis, of the cyclotron resonance mechanism to study the resonance condition, growth rates, and starting currents, as well as experimental investigations of the various types of devices have been explored [Hir77, Gra87, Fli86].

One of the cyclotron resonance maser devices, the CARM, is an especially interesting device, in that the CARM takes advantage of the large doppler frequency upshift, as shown by

$$\omega = \frac{\Omega_e}{\gamma} + k_z v_z \qquad (1.1)$$

where $\Omega_e$ is the non-relativistic gyrofrequency, $\gamma$ is the relativistic factor, $k_z$ is the axial wave propagation number and $v_z$ is the axial velocity of the electron beam, to obtain high frequencies at low magnetic fields. Also, the frequency mismatch given by (1.1) tends to remain zero (in resonance) over a long interaction time, if the frequency mismatch initially starts out as being zero. Although a promising device, CARM experiments have been conducted with limited success in obtaining an efficient device [Bek87, Pen91, Cho91]. Mode competition from the lower frequency gyrotron, higher harmonic gyrotron, and the fundamental and higher harmonic gyro-BWO, as well as sensitivity to the beam velocity spread and voltage fluctuation of the electron beam, tend to deprive the CARM of its full potential as an efficient microwave device.

Another device, the gyrotron, has also been extensively investigated. The advantages of the gyrotron are that it produces high frequency interactions with high efficiencies (when compared to other vacuum tube microwave devices). A disadvantage is that the high frequency interaction is linearly dependent on the external magnetic field available, and inversely proportional to the relativistic factor. This is evident from the resonance condition of the gyrotron, when operated near $k_z = 0$,

$$\omega = \frac{eB}{m\gamma} \qquad (1.2)$$

where e is the electron charge, m is the mass of the electron, and B is the externally applied magnetic field. Equation (1.2) also shows that when the energy of the electron is increased (as in highly-relativistic electron beams) leading to the possibility of greater efficiencies, the corresponding interaction frequency is reduced. The available magnetic field is generally the limiting factor in the uses of gyrotrons. Gyrotron experiments using

high current (~1 kA), high voltage (≥ 400 kV), field emission cathodes have shown multimegawatt microwave emission, but the pulselengths have been relatively short (< 100 nanoseconds) which is generally limited by the electron beam accelerator used in the experiments [Gin79, Gol87]. On the other hand, thermionic cathode experiments (current ≤ 30 amps, voltage ≤ 100 kV) have demonstrated long-pulse (millisecond and continuous wave (CW) ) capabilities of the gyrotron, but with moderate microwave output power (hundreds of kilowatts for CW, to megawatts for pulsed) [Rea80, Gra87, Bra90].

Accelerator technology exists to produce intense electron beams with high currents and high voltages over microsecond pulselengths, which give the possibility of delivering several hundreds of joules of microwave emission and thereby overcoming the above gyrotron limitations. An example of such an accelerator is MELBA (Michigan Electron Long Beam Accelerator) with parameters of: peak voltage = - 1 MV, currents = 10 - 50 kA, pulselengths = 0.5 - 5 μs. The general problem with this type of accelerator is that it employs a field (explosive) emission cathode, which tends to produce a relatively large velocity spread on the e-beam (especially when compared to a thermionic cathode) and has a voltage fluctuation, both of which degrade the efficiency and may even detune the resonance condition of gyrotron and CARM devices.

The gyro-BWO, another cyclotron resonance maser device, is an excellent device for this type of accelerator since it is relatively insensitive to the beam velocity spread and voltage fluctuation of the electron beam. This can be seen from Figure 1.1. Since the interaction of the gyro-BWO occurs on the left-hand side of the dispersion curve, the possibility exists that the interaction will remain in resonance for a long interaction period, even if there is some velocity spread or voltage fluctuation in the electron beam. Some theoretical analysis of the gyro-BWO exists [Lau81, Par84, Ahn89], as well as some initial gyro-BWO experiments involving small currents (< 10 amps) and low
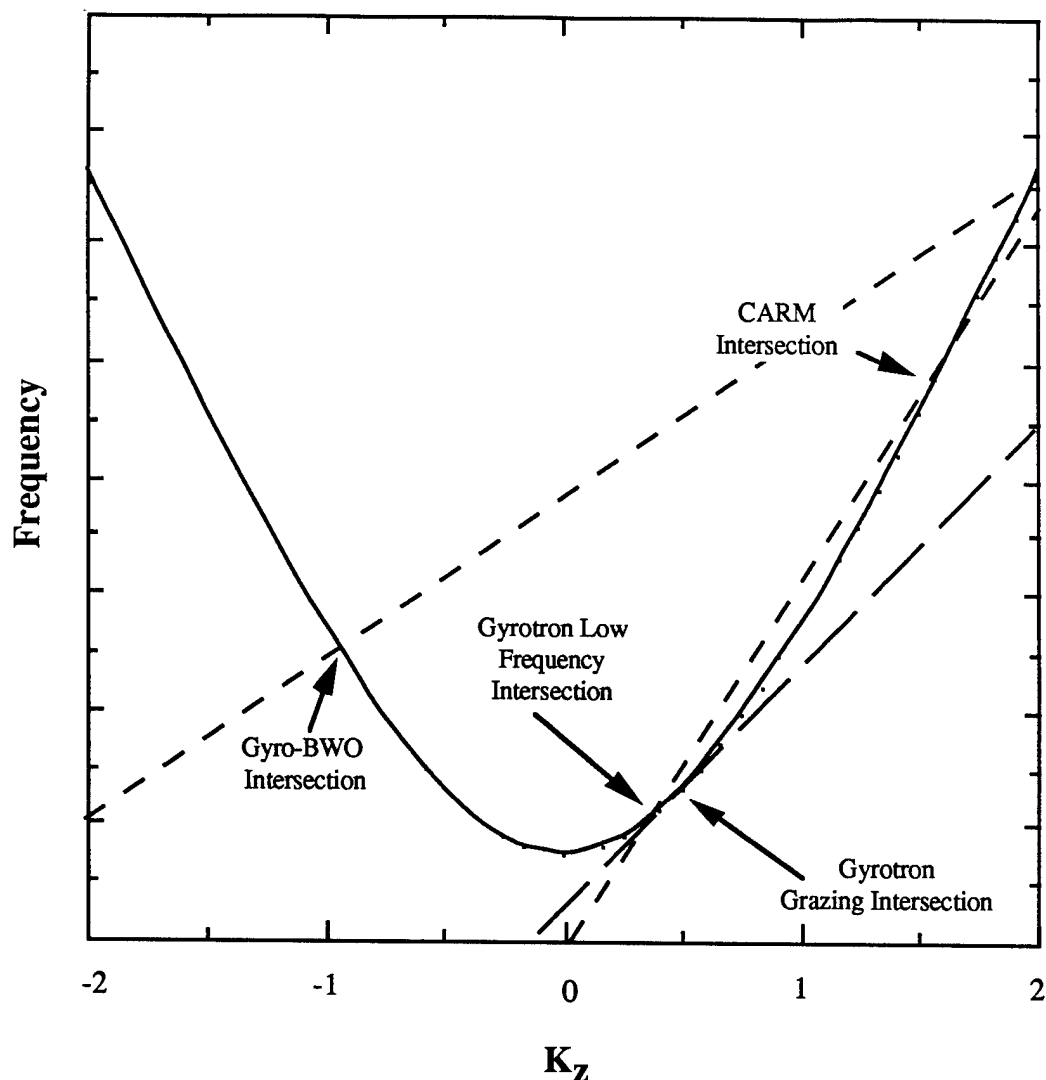
**Figure 1.1. Dispersion relation showing the different types of electron cyclotron resonance interactions. The solid line is the interaction cavity dispersion curve, while the dashed lines are the electron beam dispersion lines.**

voltages (< 50 kV) [Gus89, Par90, Bas90] which generated relatively low power ( ~ 10

kW) but reasonable efficiencies of ~ 15 %. High current, high voltage gyro-BWO

questions remain unanswered, which leads to the experimental investigation presented

here. Particular questions addressed are the magnetic tunability of the interaction

frequency, effects of high current (1 - 2 kA) solid electron beams and annular (150 - 250

amps) electron beams, broadband frequency interactions over long pulselengths, mode

competition from higher order modes or higher harmonics, and extraction of the
generated microwave emission from the gyro-BWO.

To interpret the results from the experimental investigation, a brief overview of
the basic electron cyclotron resonance interactions is presented in Chapter II. Chapter III
describes the experimental set up and diagnostics, as well as experimental results
obtained from diode closure experiments which were conducted to test effects of different
diode magnetic field configurations and cathode designs on the closure velocity of the
cathode plasma in the diode region. Chapter IV describes the gyro-BWO experimental
results, and Chapter V presents conclusions and the direction for future research.

## 1.2 Differences Between the Conventional Backward-Wave Oscillator and the Gyro-BWO

A conventional BWO (referred to from here on as BWO) differs in many respects
from a gyro-BWO. For example, a BWO is a slow-wave device, that is the interaction
occurs below the light line, $\omega/k = c$, on the dispersion curve. In order to take advantage
of the slow-wave of the electron beam, a periodic structure must be employed in the
interaction cavity to slow down the electromagnetic wave that exists in the interaction
region. The gyro-BWO, on the other hand, is a fast-wave device, and needs no periodic
structure. This leads to three advantages in using the gyro-BWO. One is the
construction of the interaction region. For the gyro-BWO, a simple hollow tube is all that
is needed, as opposed to a precisely machined periodic structure. The second is that a
simple hollow tube has the potential for greater power-handling capabilities than a
corresponding periodic structure. The third is the theoretical analysis of the BWO is
much more difficult than for the gyro-BWO, and usually requires numerical simulation to
describe the interactions. A brief description of the BWO dispersion relations appears in
Appendix B.

Another difference between the BWO and the gyro-BWO is the BWO is typically
run in the transverse magnetic (TM) modes which takes advantage of the axial bunching

of the electron beam (the TM modes are used to increase the power handling capability of the slow-wave structure). The gyro-BWO is predominately a transverse electric (TE) interaction, in that it obtains electron energy from the azimuthal bunching of the electron beam.

The greatest difference between the two devices is perhaps the amount of research done on the two different devices. Extensive theoretical and experimental research has been conducted on the BWO [Swe86, Lei86, Kan79, Car90]. This research has produced high-power (from MW to several hundreds of MW), high frequency (from 1 - 150 GHz), microwave emission with efficiencies ranging from 2 - 30 % [Lei86, Car90]. Pulselengths have ranged from tens of nanoseconds to several microseconds depending on the type of cathode used (field emission for tens of nanoseconds, thermionic for several microseconds), as was the case for gyrotrons stated above. Also as discussed for the gyrotron above, the highest powers were obtained with the shortest pulselengths in the BWO experiments. Even though the gyro-BWO appears to have some advantages over the conventional BWO, gyro-BWO research has been limited to just a few theoretical discussions [Wac80, Par84], and to a few low current (< 10 amps), low voltage (< 100 kV) thermionic cathode experiments, thus motivating the experimental research presented here.

# CHAPTER II
# ELECTRON CYCLOTRON RESONANCE MASER THEORY

## 2.1 Introduction

The theory for the electron cyclotron resonance interaction has been studied for the past three decades, beginning with Twiss [Twi58], Gapanov [Gap59], and Schneider [Sch59]. The interaction has been described by both quantum mechanics [Sch59] and by classical mechanics [Twi58, Gap59]. Due to the large quantum numbers, the energy levels can be considered a 'continuum' and thus the interaction can be completely described by classical theory. For this reason, the quantum theory is not presented here.

Classical theory presents the cyclotron resonance maser (CRM) interaction as the azimuthal bunching process of gyrating electrons in an electromagnetic field. This phase bunching is produced by the change in $\gamma$ (the relativistic factor) as electrons lose or gain energy in a transverse electric (TE) field that exists in the interaction region. The change in $\gamma$ results in a corresponding change in the relativistic cyclotron frequency of the electron as evidenced by equation (2.1),

$$\Omega_r = \frac{eB}{m\gamma} \tag{2.1}$$

where e is the electronic charge, m is the mass of the electron, and B is the externally applied magnetic field.

The cyclotron frequency change is opposite for electrons in opposite phases of the orbit, that is electrons that lead the TE field have a decrease in the cyclotron frequency whereas the electrons that lag the TE field have an increase in their cyclotron frequency. This leads to a drifting of the electrons to the position of the electric field phase. An example of the drift motion is given in Figure 2.1. If the cyclotron frequency, $\Omega$, (in the

moving frame of the electrons) is greater than that of the TE field ($\omega < \Omega$), then the TE

field will gain energy from the electrons, and will experience a growth in its relative

amplitude. However, if the opposite is true ($\Omega < \omega$) then the electrons will gain energy

from the TE field, and thus the TE field will decay. Converting the condition for TE field

growth to the lab frame leads to the doppler-shifted condition of

$$\omega < \frac{\Omega}{\gamma} + k_z v_z \qquad (2.2)$$

where $\Omega$ is the non-relativistic gyrofrequency, $\gamma$ is the relativistic factor, $k_z$ is the axial

wave propagation number and $v_z$ is the axial velocity of the electron beam
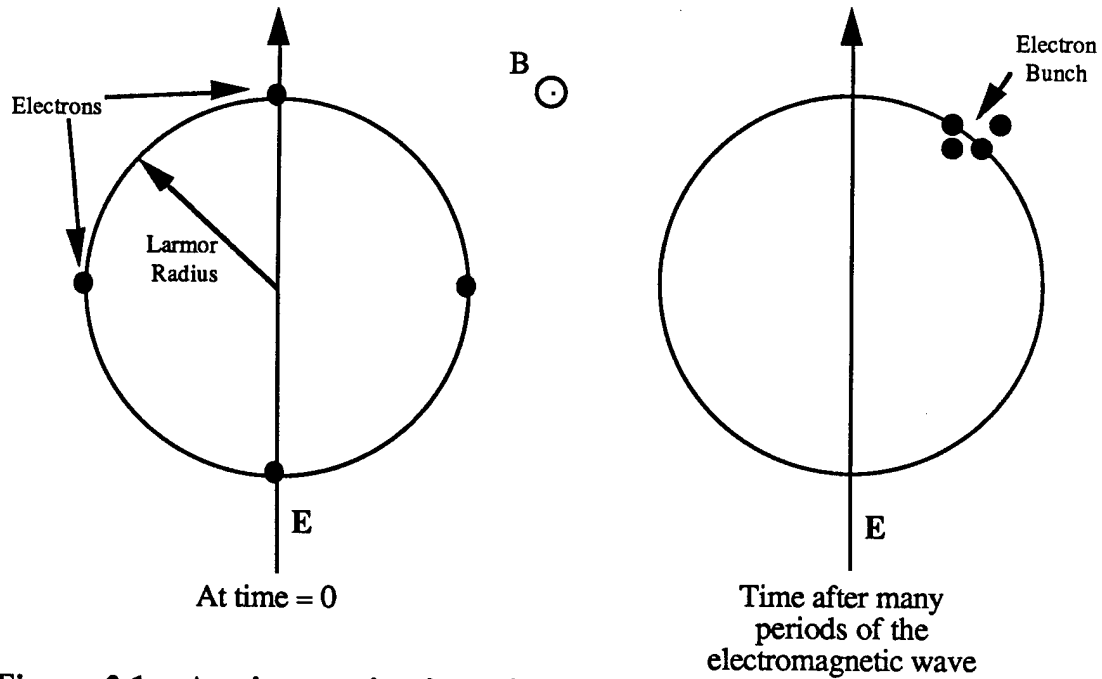


Figure 2.1. A microscopic view of the electron drift that leads to bunching due to the change in the relativistic cyclotron frequency of the electrons.

The CRM theory is generally presented in two regimes, the linear and non-linear.

Linear theory is used to describe threshold currents (the current at which the oscillation

begins), threshold lengths of the interaction cavity, growth rates, etc., which come about

from small signal interactions. Non-linear theory is used to describe the saturation

mechanisms as well as the stabilization of the overall system that comes about from the

large signal interaction. A brief review of both the linear and non-linear theory is presented in this chapter, as well as the criteria for the existence of the absolute instabiltity which is the mechanism behind the gyrotron-backward-wave instability.

The theory of the ECM is described extensively in the literature, beginning with the classical [Twi58, Gap59] and quantum [Sch59] descriptions. Reviews of the linear and non-linear theories can be found in [Bra81] for CARMs and gyrotrons, [Chu81] for gyrotrons, [Fli86] for TE and TM cylindrical waveguide modes for CARMs and gyrotrons, and simulation results can be found in [Lin87]. Gyro-BWO linear theory is available in [Wac80] for rectangular waveguides, as well as [Par84] which gives a more complete description of the linear theory for the $TE_{n0}$ modes for rectangular waveguides and $TE_{0n}$ modes for cylindrical waveguides. A three-dimensional non-linear analysis is presented in [Gan89]. The derivation of the ECM dispersion relation that follows will be that presented in [Fli86], since it describes the interaction for all TE and TM modes. A review of the absolute instability can be found in [Lau81, Par84, Dav89, Dav90], and the presentation described below will follow [Lau81].

Unless otherwise noted, all equations that follow are in MKS, and the subscript zero denotes an initial value associated with the electron beam or electromagnetic parameters.

## 2.2 Dispersion Relation for the ECM and Gyro-BWO (Linear Theory)

The small signal kinetic theory model for the dispersion relation is based on the following:

1) An annular electron beam of average radius $r = r_b$ propagating in a cylindrical interaction cavity of radius $r = r_c$ in the z-direction.

2) The electrons move along helical trajectories due to the external uniform magnetic field, applied in the z-direction, $B_{0z} \hat{z}$.

3) The assumption that the electron beam is 'sufficiently tenuous', that is the electron beam has a small current density, that its space charge electric field can be neglected (neglect self-fields).

4) The spatial structure of the vacuum waveguide (interaction cavity) modes are unaffected by the presence of the electron beam.

The linearized relativistic Vlasov equation is used to describe the dynamics of the electron beam,

$$\frac{d}{dt} f_1(\mathbf{x},\mathbf{p},t) = \left[\frac{\partial}{\partial t} + \frac{\mathbf{p}}{\gamma} \cdot \frac{\partial}{\partial \mathbf{x}} - e \left(\frac{\mathbf{p}}{\gamma} \times B_0 \mathbf{e}_z\right) \cdot \frac{\partial}{\partial \mathbf{p}}\right] f_1(\mathbf{x},\mathbf{p},t)$$
$$= e \left(\mathbf{E} + \mathbf{v} \times \mathbf{B}\right) \cdot \frac{\partial f_0(\mathbf{x},\mathbf{p})}{\partial \mathbf{p}} \tag{2.3}$$

where $f_0$ is the meta-equilibrium distribution function, $f_1$ is the perturbed distribution function, and $\mathbf{E}$ and $\mathbf{B}$ are the electromagnetic fields governed by Maxwell's equations, (A.13) and (A.14).

Adding the TE mode electromagnetic Maxwell wave equation in a cylindrical cavity,

$$\left(\frac{1}{c^2} \frac{\partial^2}{\partial t^2} - \nabla^2\right) B_z = \frac{\mu_0}{r} \left[\frac{\partial (r J_\theta)}{\partial r} - \frac{\partial (J_r)}{\partial \theta}\right] \tag{2.4}$$

where $B_z$ is given by (A.32f), and $J_\theta$ and $J_r$ are components of the perturbed electron beam currents described by

$$J_\theta = - e \int d^3 p f_1 v_\theta = - e \int d^3 p f_1 v_\perp \sin(\phi - \theta) \tag{2.5}$$

$$J_r = - e \int d^3 p f_1 v_r = - e \int d^3 p f_1 v_\perp \cos(\phi - \theta) \tag{2.6}$$

leads to a closed set of equations, (2.3) - (2.6) along with (A.32).

The meta-equilibrium function is specified in terms of the constants of motion of the system which are the beam radius, $r_0$, the perpendicular momentum, $p_\perp$, and the parallel momentum, $p_z$. The meta-equilibrium distribution function becomes,

$$f_0(\mathbf{x},\mathbf{p}) = N_0 R_0(r_0) P_0(p_\perp, p_z) \tag{2.7}$$

12

where $N_0$ is the electron beam number density. Using (2.3) - (2.7) and (A.32), and after much algebra, leads to the TE mode interaction dispersion equation (see [Fli86 or Bra81]),

$$\omega^2 - k_c^2 c^2 - k_z^2 c^2 = L_{mn} \int_0^{r_c} r_0 dr_0 \int_0^\infty p_\perp dp_\perp \int_{-\infty}^{+\infty} p_z dp_z \, R_0(r_0)P_0(p_\perp, p_z)[T_{sm} - U_{sm}] \quad (2.8)$$

where $k_c$ is the cutoff wavenumber given by (A.39), and

$$L_{mn} = \frac{-2N_0\mu_0 e^2 c^2}{m_0 r_c^2 K_{mn}} \quad (2.9)$$

$$K_{mn} = \left[ 1 - \frac{m^2}{\chi_{mn}^2} \right] J_m^2(\chi_{mn}) \quad (2.10)$$

$$T_{sm} = \frac{(\omega^2 - k_z^2 c^2)p_\perp^2 H_{sm}}{\gamma^3 m_0^2 c^2 (\omega - k_z v_z - s\Omega_r)^2} \quad (2.11)$$

$$H_{sm} = J_{s-m}^2(k_c r_0)J_s'^2(k_c r_L) \quad (2.12)$$

$$U_{sm} = \frac{(\omega - k_z v_z)Q_{sm}}{\gamma(\omega - k_z v_z - s\Omega_r)} \quad (2.13)$$

$$Q_{sm} = 2H_{sm} + k_c r_L \left[ J_{s-m}^2(k_c r_0)J_s'(k_c r_L)J_s''(k_c r_L) \right.$$

$$\left. + \frac{1}{2}J_{s-m-1}^2(k_c r_0)J_s'(k_c r_L)J_{s-1}'(k_c r_L) - \frac{1}{2}J_{s-m+1}^2(k_c r_0)J_s'(k_c r_L)J_{s+1}'(k_c r_L) \right] \quad (2.14)$$

where $J_m(x)$ is the Bessel function of order m, $\chi_{mn}'$ is the nth root of $J_m'(x) = 0$, $\mu_0$ is the magnetic permeability, $\Omega_r$ is the relativistic cyclotron frequency, $r_L$ is the Larmor radius, s is the harmonic number (s = 1 is generally referred to as the fundamental mode, with s = 2, 3,.... referred to as the second, third, .... harmonics), and

$$J_m'(x) = \frac{\partial J_m(x)}{\partial x} \quad (2.15)$$

Using an infinitely thin, annular ideal cold electron beam,

$$R_0(r_0) = \frac{A_b}{r_0} \delta(r_0 - r_b) \qquad (2.16)$$

$$P_0(p_\perp, p_z) = \frac{1}{2\pi p_\perp} \delta(p_\perp - p_{\perp 0}) \delta(p_z - p_{z0}) \qquad (2.17)$$

where $A_b$ is the cross-sectional area of the electron beam, and $r_b$ is the average radius of the electron beam, the dispersion equation can be reduced to

$$\omega^2 - k_c^2 c^2 - k_z^2 c^2 = -\frac{\omega_{pe}^2}{K_{mn}} [W_{sm} - Y_{sm}] \qquad (2.18)$$

with

$$W_{sm} = \frac{(\omega^2 - k_z^2 c^2)\beta_{\perp 0}^2 H_{sm}}{(\omega - k_z v_{z0} - s\Omega_r)^2} \qquad (2.19)$$

$$Y_{sm} = \frac{(\omega - k_z v_{z0})Q_{sm}}{(\omega - k_z v_{z0} - s\Omega_r)} \qquad (2.20)$$

and

$$\omega_{pe}^2 = \left( \frac{N_0 e^2 \mu_0 c^2 A_b}{m_0 \pi r_c^2} \right) \qquad (2.21)$$

is the 'effective' plasma frequency that includes a beam-waveguide fill factor [She81]. Note that the linear equations given in [Par84] for the gyro-BWO can be derived from equation (2.18) by setting the azimuthal variation number 'm' to zero and doing a little algebraic manipulation, thus the following analysis is also valid for the gyro-BWO.

$W_{sm}$, equation (2.19), which is the first term of the right-hand side of equation (2.18) is the source of the instability, while the second term, $Y_{sm}$ (equation 2.20)), is the stabilizing term, or the threshold beam energy for the instability. One can also find the uncoupled vacuum mode dispersion relations from equation (2.18)

$$(\omega^2 - k_c^2 c^2 - k_z^2 c^2)(\omega - k_z v_z - s\Omega_r)^2 = 0 \qquad (2.21)$$

where the first term,

$$\omega^2 - k_c^2 c^2 - k_z^2 c^2 = 0 \qquad (2.22)$$

is the vacuum waveguide dispersion relation (A.38), and

$$\omega - k_z v_z - s\Omega_r = 0 \qquad (2.23)$$

is the doppler-shifted electron beam cyclotron mode dispersion relation. When equation

(2.23) is near resonance, the frequencies and wavenumbers are determined by the

simultaneous solution of equations (2.22) and (2.23), which gives

$$\omega_0 = C_0 \pm \sqrt{C_0^2 - C_1^2} \qquad (2.24)$$

with

$$C_0 = \frac{s\Omega_r \gamma_0^2 (1 + \alpha^2)}{1 + \gamma_0^2 \alpha^2} \qquad (2.25)$$

$$C_1 = \frac{\omega_c^2 (\gamma_0^2 - 1) + s\Omega_r^2 \gamma_0^2 (1 + \alpha^2)}{1 + \gamma_0^2 \alpha^2} \qquad (2.26)$$

and

$$k_{z0} = \frac{\gamma_0 (\omega_0 - s\Omega_r)}{c} \sqrt{\frac{1 + \alpha^2}{\gamma_0^2 - 1}} \qquad (2.27)$$

where $\alpha$ is the ratio of the beam perpendicular velocity to beam parallel velocity, $\alpha = v_\perp / v_z$, and $\omega_c$ is the waveguide (interaction cavity) cutoff frequency given in equation

(A.41). This leads to the dispersion graph which demonstrates some of the possible

ECM interactions shown in Figure 1.1, which is reproduced here as Figure 2.2 for

convenience.

The gyrotron grazing intersection shown in Figure 2.2 occurs when,

$$\left( \frac{\partial \omega}{\partial k_z} \right)_{beam} = \left( \frac{\partial \omega}{\partial k_z} \right)_{waveguide} \qquad (2.28)$$
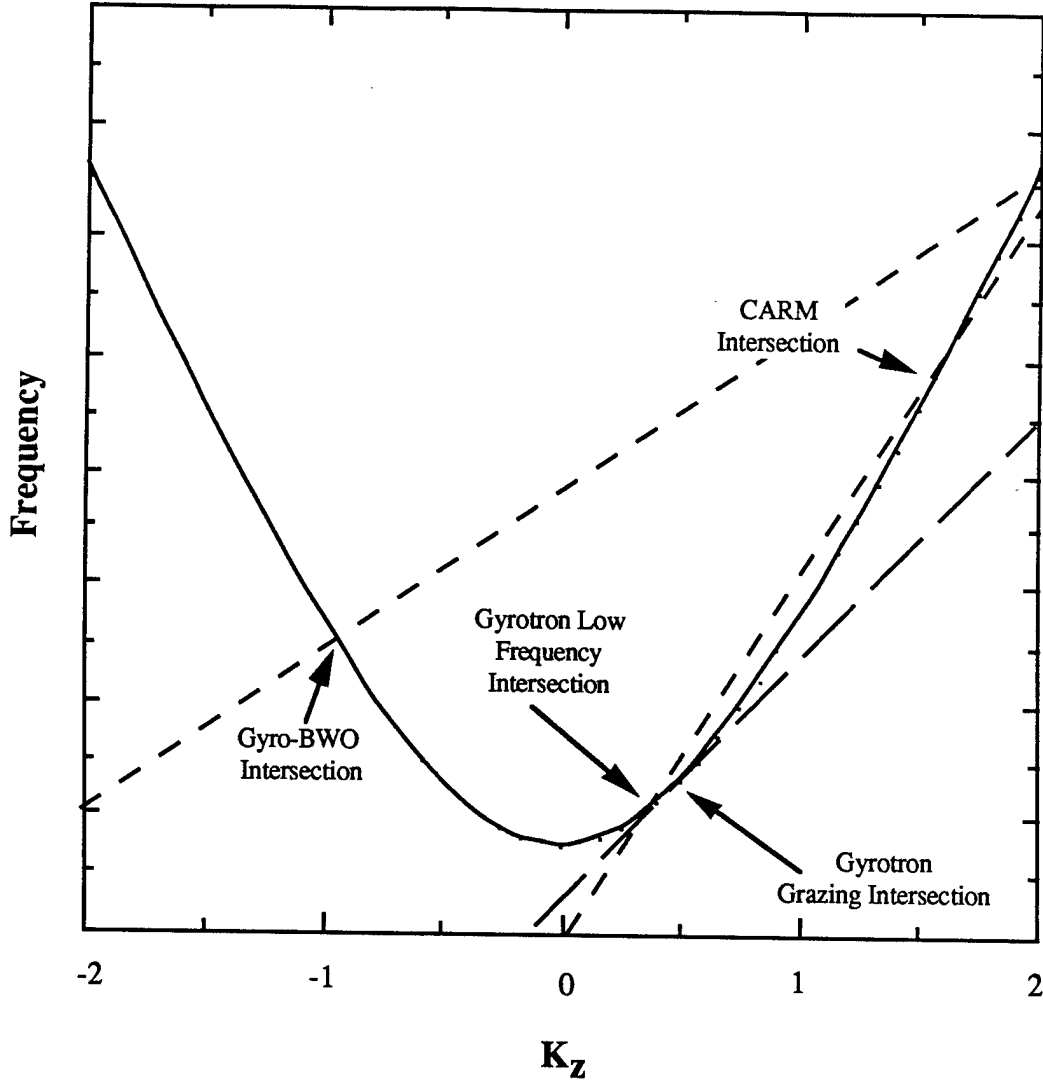
Figure 2.2. Dispersion graph showing the different types of electron cyclotron resonance interactions. The solid line is the interaction cavity dispersion curve (equation 2.22), while the dashed lines are the electron beam dispersion lines (equation 2.23).

or

$$\frac{k_c}{k_z} = \sqrt{\frac{2 - \gamma_0^2}{\gamma_0^2 - 1}}$$

(2.29)

which leads to only one intersection from equation (2.24) and (2.27) of

$$\omega_0 = \frac{\omega_c^2}{s\Omega_r}, \qquad k_{z0} = \frac{\omega_0 \beta_{z0} \gamma_{z0}}{c}$$

(2.30)

where

$$\beta_{z0} = \frac{v_{z0}}{c}, \qquad \gamma_{z0}^2 = \frac{1}{1-\beta_{z0}^2} \tag{2.31}$$

When

$$\frac{k_c}{k_z} \neq \sqrt{\frac{2 - \gamma_0^2}{\gamma_0^2 - 1}} \tag{2.32}$$

then two intersections exist as shown by Figure 2.2. These intersections can occur in two different regimes, one regime occurring with both intersections on the right hand side of the dispersion plot with a low frequency gyrotron intersection and a high frequency intersection (referred to as the CARM if $\beta_{ph0}$ is approximately one). The other regime is when the low frequency intersection occurs on the left hand side of the dispersion plot (the gyro-BWO intersection with both the group and phase velocities less than zero) and the high frequency intersection remains on the right hand side of the dispersion plot (which could still be a CARM intersection).

The temporal growth rate for the electron cyclotron resonance instability can be found in two ways. The first way is to substitute $\omega = \omega_0 + \Delta\omega$, $k_z = k_{z0}$ into the dispersion equation (2.18), where $\omega_0$ and $k_{z0}$ are solutions given by equation (2.24) and (2.27), and neglecting small terms leads to,

$$\Delta\omega^3 = -\frac{\omega_{pe}^2 \omega_c^2 \beta_{\perp 0}^2 H_{sm}}{2 K_{mn} \omega_0} \tag{2.33}$$

Breaking $\Delta\omega$ into real and imaginary parts, $\Delta\omega = \omega_r + i\omega_i$ then equation (2.33) has the solution:

$$\omega_r = \left(\frac{\omega_{pe}^2 \omega_c^2 \beta_{\perp 0}^2 H_{sm}}{16 K_{mn} \omega_0}\right)^{\frac{1}{3}} \tag{2.34a}$$

$$\omega_i = \sqrt{3}\, \omega_r \tag{2.34b}$$

The real part of $\Delta\omega$, equation (2.34a) gives the beam-wave interaction width, while the imaginary part of $\Delta\omega$, equation (2.34b) gives the temporal growth rate. From equation

(2.34b) the largest growth rate will occur for waves closest to the cutoff frequency of the waveguide (interaction cavity), and will also occur for electrons with a large transverse velocity. Note the growth rate decreases monotonically as the resonance frequency increases away from the waveguide cutoff frequency. This shows the competition that exists between the gyrotron and CARM, or the gyro-BWO and the CARM, mentioned in Chapter I. Since the gyrotron and gyro-BWO operate near cutoff, their growth rate will always be greater than the growth rate for the CARM. It should be noted that equation (2.34b) does not apply when the instability becomes absolute. The onset of absolute instability, a non-linear phenomena, is discussed in section 2.6.

The second way to obtain the temporal growth rate is by numerically solving equation (2.18). It should be noted that equation (2.18) is still a linear approximation and is still not applicable to the absolute instability regime. Figures 2.3, 2.4, and 2.5 show examples of the growth rates obtained by solving the coupled dispersion equation (2.18) numerically. These numerical results are superimposed on the dispersion plots for different operating parameters used in the experiments presented in Chapter I. Notice that the growth rates are largest for intersections near the grazing intersection (Figure 2.4 and 2.5) than away from grazing (Figure 2.3). Also notice that the lower frequency intersection of Figure 2.3 has a larger growth rate than the upper frequency intersection which is expected, as discussed above.

The spatial growth rate can also be obtained by allowing $\omega = \omega_0$ and $k_z = k_{z0} + \Delta k$, and sustituting $\omega$ and $k_z$ into the dispersion equation (2.18). Again ignoring small terms leads to the spatial growth rate

$$k_i = \left(\frac{\beta_{ph0}}{\beta_{z0}^2}\right)^{\frac{1}{3}} \frac{\omega_i}{c}$$

$$= \sqrt{3} \left(\frac{\beta_{ph0}\omega_{pe}^2\omega_c^2\alpha_0^2 H_{sm}}{16 K_{mn}\omega_0}\right)^{\frac{1}{3}} \qquad (2.35)$$

18
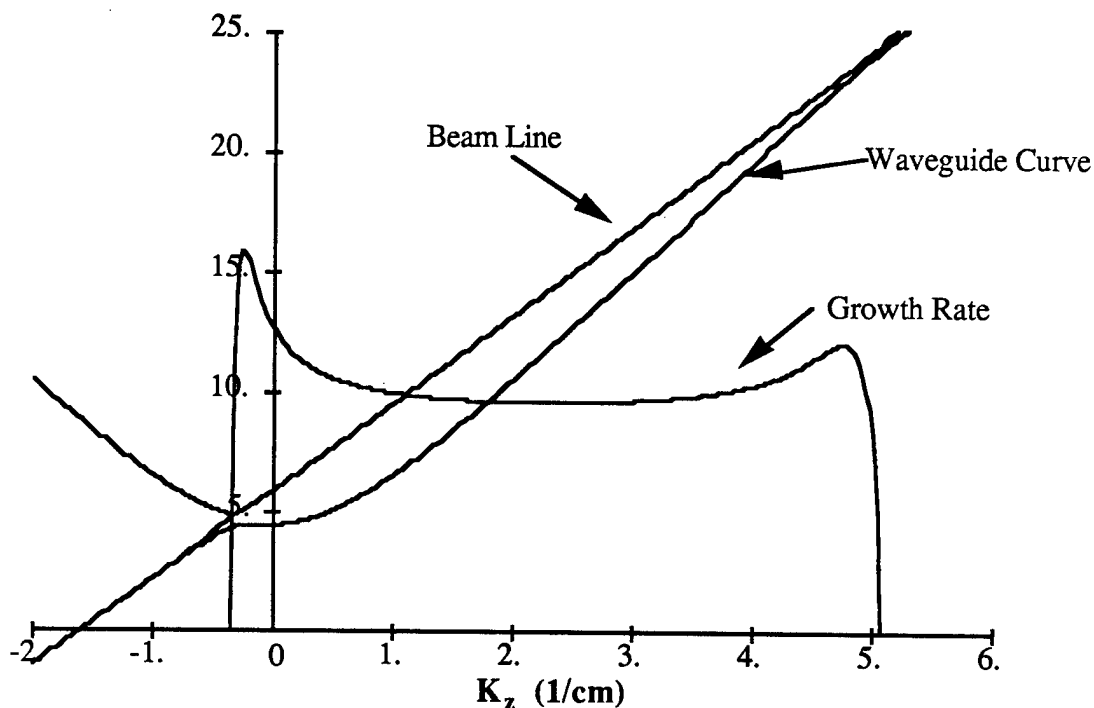


Figure 2.3.  The temporal growth rate superimposed on the dispersion
curves for the TE$_{11}$ mode at parameters of: beam voltage = 750 kV,
beam current = 150 amps, $\alpha$ = 0.65, average beam radius = 1.2 cm,
cavity radius = 1.93 cm, and B = 5.2 kG.  The y-axis is the
frequency, with the dispersion curves in GHz, and the growth rate in
1 x 10$^7$ per second.
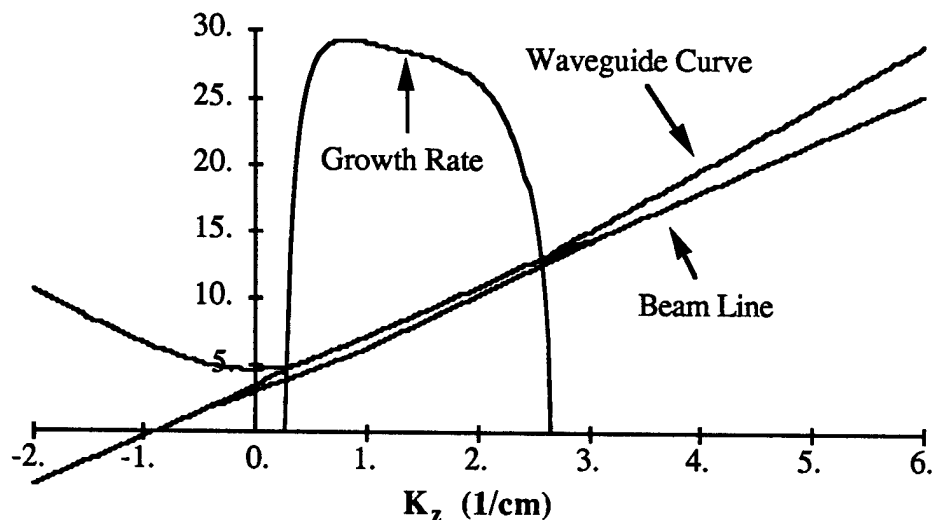


Figure 2.4.  The temporal growth rate superimposed on the dispersion
curves for the TE$_{11}$ mode at parameters of: beam voltage = 750 kV,
beam current = 150 amps, $\alpha$ = 0.65, average beam radius = 1.2 cm,
cavity radius = 1.93 cm, and B = 3.0 kG.  The y-axis is the
frequency, with the dispersion curves in GHz, and the growth rate in
1 x 10$^7$ per second.
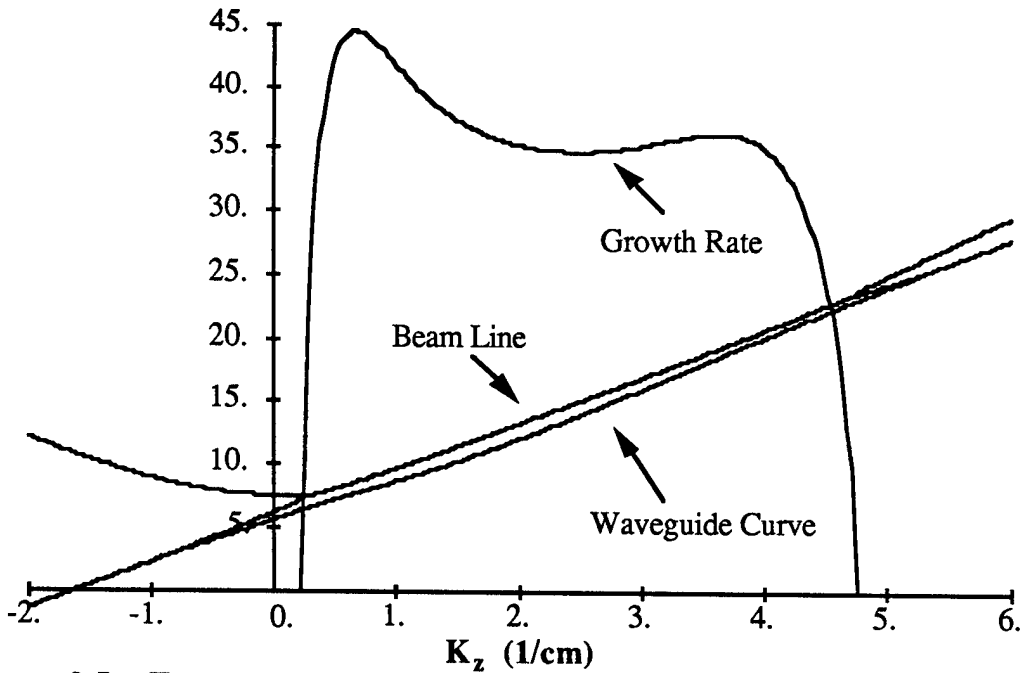
**Figure 2.5.** The temporal growth rate superimposed on the dispersion curves for the TE$_{21}$ mode at parameters of: beam voltage = 750 kV, beam current = 150 amps, $\alpha$ = 0.65, average beam radius = 1.2 cm, cavity radius = 1.93 cm, and B = 5.2 kG. The y-axis is the frequency, with the dispersion curves in GHz, and the growth rate in 1 x 10$^7$ per second.

which shows the spatial growth rate depends on the two-thirds power of $\alpha$. Again, the instability depends on the transverse energy of the electrons, as in equation (2.34b).

The TM modes are a competing interaction in the CRM process, but due to the small growth rates and weak coupling between the beam and the TM waveguide modes, the TE modes dominate, so the TM modes are not presented here. The TM mode dispersion relation and growth rates are presented in [Fli86].

## 2.3 Non-Linear Theory

Non-linear single particle theory is used to describe the saturation and stabilization mechanisms of the electron cyclotron resonance interaction. Two mechanisms responsible for the saturation of the CRM instability are the depletion of rotational energy (transverse energy) and phase trapping of the gyrating particles in relation to the electromagnetic wave. The depletion of transverse energy occurs if the transverse energy

of the electron beam is slightly greater than the threshold beam energy represented by equation (2.20). This results in all the transverse energy of the electrons being converted to electromagnetic wave energy before phase trapping (or thermalization) takes place, producing a linear stabilization of the system. However, if the transverse energy of the electron beam is much greater than the stabilization term of equation (2.20), which could be the case for very- or ultra-relativistic electron beams, the electrons will become phase trapped in relation to the electromagnetic wave and saturation will occur without all the transverse energy of the electrons being converted to electromagnetic wave energy.

### 2.3.1 Electron Bunching

The following three equations are used in the non-linear analysis of the CRM. The first is the relativistic Lorentz force equation

$$\frac{d\mathbf{p}}{dt} = -e\left[\mathbf{E} + \frac{\mathbf{p}}{\gamma m_0} \times (\mathbf{B} + B_0\mathbf{e}_z)\right] \tag{2.36}$$

The second is the energy equation,

$$\frac{d\varepsilon}{dt} = m_0 c^2 \frac{d\gamma}{dt} = -e\mathbf{v} \cdot \mathbf{E} \tag{2.37}$$

The third equation is the general energy-momentum relation

$$\varepsilon^2 = m_0^2 c^4 + p_\perp^2 c^2 + p_z^2 c^2 \tag{2.38}$$

These three equations, (2.36) - (2.38), can be used to give a simplified view of the electron bunching mechanism [Bai87]. One begins with the doppler-shifted frequency described in equation (2.23)

$$\omega = k_z v_z + s\Omega_r \tag{2.39}$$

Taking the time derivative will describe the change in $\omega$ as the electron velocity changes through interaction with the electromagnetic fields. Using equation (2.37), the z-component of equation (2.36), and Faraday's law from Maxwell's equations (A.13b)

$$B_\perp = \frac{k_z}{\omega} \hat{z} \times E_\perp \tag{2.40}$$

leads to a result,

$$\frac{d\omega}{dt} = \frac{-ek_z^2}{m_0 \gamma \omega} \left[ 1 - \frac{\omega^2}{k_z^2 c^2} \right] v_\perp \cdot E_\perp \tag{2.41}$$

There are two terms on the right-hand side of equation (2.41) which can be used to describe the electron bunching. The first term comes about from the Lorentz force term, and produces a phase bunching along the z-direction. This phase bunching is associated with the slow-wave, or Weibel [Bai87], mechanism. This type of phase bunching is also referred to as force bunching. The second term in the right-hand side of equation (2.41) comes from the energy change due to acceleration or deceleration of the electron (the time rate of change of $\gamma$) and produces the azimuthal phase bunching associated with the CRM (fast-wave) mechanism. This type of bunching is also referred to as inertial bunching. Figure 2.6 gives an example of two electrons placed in orbital positions where $v_\perp \cdot E_\perp$ in equation (2.41) is maximum. Since the sign of $v_\perp \cdot E_\perp$ in equation (2.41) is opposite for the two electrons in Figure 2.6, phase bunching will occur as the two electrons begin to drift towards each other around the orbital path.
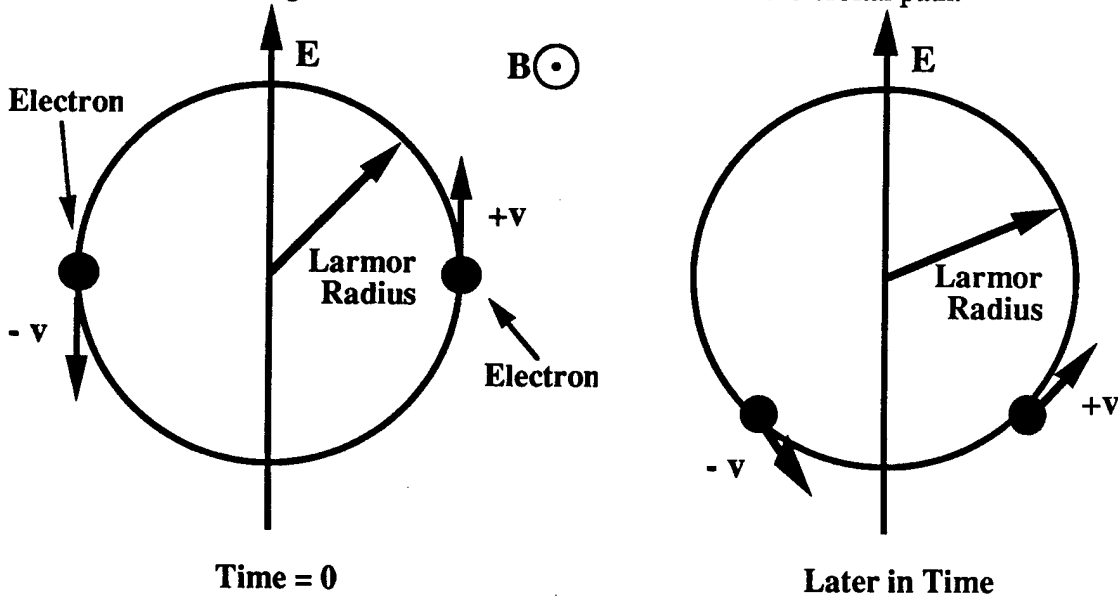


Figure 2.6. Example of electron bunching along an orbital path.

The relative magnitude of the second term in the right-hand side of equation (2.41) determines the rate and direction of the phase bunching, and which mechanism (slow-wave or fast-wave) dominates. If $\omega > k_z c$, then the phase bunching associated with the CRM mechanism dominates. If $\omega < k_z c$, then the phase bunching occurs toward the opposite side of the orbit path and the slow-wave mechanism dominates. If $\omega \cong k_z c$, then $d\omega/dt$ is zero which leads to the autoresonance condition of the CARM mentioned previously in section 2.2.

## 2.3.2 Efficiencies of the CRM

The efficiency of the CRM can be expressed by a single-particle efficiency, and by an efficiency associated with the electron bunching.

The single-particle efficiency can be derived by combining equation (2.36) with (2.40) and obtaining the z-component,

$$\frac{dp_z}{dt} = -e\left[E_z + (\mathbf{v} \cdot \mathbf{E})\frac{k_z}{\omega} - \frac{(\mathbf{v} \cdot \mathbf{k})E_z}{\omega}\right] \tag{2.42}$$

Substituting equation (2.37) into equation (2.42), and using the TE mode condition of $E_z = 0$, leads to the following time rate of change of energy,

$$\frac{d\varepsilon}{dt} = v_{ph}\frac{dp_z}{dt} \tag{2.43}$$

Equation (2.38) shows that the change in electron energy is also accompanied by a corresponding change in the electron axial momentum which is a result of the electron recoil. This was first pointed out by [Bra81].

One can obtain an approximate equation for the electron energy change, $\Delta\varepsilon$, by combining equation (2.43) and equation (2.37), and using the condition of $2\varepsilon(1-\beta_{z0}/\beta_{ph})$ $\gg \Delta\varepsilon(1-1/\beta_{ph})$. This leads to

$$\Delta\varepsilon \cong \frac{c^2\,(2p_{\perp 0}\Delta p_\perp + \Delta p_\perp^2)}{2\varepsilon_0\left(1 - \dfrac{\beta_{z0}}{\beta_{ph}}\right)} \tag{2.44}$$

The maximum energy that is available from the electrons depends on the initial transverse momentum, thus once the initial transverse momentum becomes zero, $\Delta p_\perp = -p_{\perp 0}$, the maximum relative loss of the kinetic energy of a single particle becomes

$$\eta_{sp} = \frac{\varepsilon_0 - \varepsilon}{\varepsilon_0 - m_0 c^2} \cong \frac{\beta_{\perp 0}^2}{2 \left(1 - \frac{\beta_{z0}}{\beta_{ph}}\right)\left(1 - \frac{1}{\gamma_0}\right)} \qquad (2.45)$$

In theory, the single-particle efficiency given in equation (2.45) can be close to unity if the transverse energy of the electron is dominant ($\beta_{\perp 0} \sim \beta_0$) which is generally associated with the operation of a gyrotron (or gyro-BWO operating close to the waveguide cutoff).

The efficiency associated with the electron bunching takes into account an averaging over the initial electron phase. The electron bunching is compact if the electrons are shifted by the electromagnetic wave field at half a cyclotron turn. The bunch then begins to lag in phase (the deceleration phase) and energy extraction from the electrons occurs. The magnitude of the energy change in the process of bunching can be approximated as [Bra81]

$$\frac{\Delta \varepsilon}{\varepsilon} \cong \frac{1}{sN} \frac{\left(1 - \frac{\beta_{z0}}{\beta_{ph}}\right)}{\left(1 - \frac{1}{\beta_{ph}^2}\right)} \qquad (2.46)$$

where N is the number of turns made by an electron in the interaction space. Averaging over the initial electron phase gives an efficiency of

$$\eta \cong \frac{1}{sN} \frac{\left(1 - \frac{\beta_{z0}}{\beta_{ph}}\right)}{\left(1 - \frac{1}{\beta_{ph}^2}\right)\left(1 - \frac{1}{\gamma_0}\right)} \qquad (2.47)$$

which may be close to the single-particle efficiency in equation (2.45) if the bunching is compact and an optimum number of cyclotron turns exists as defined by

$$sN_{opt} \cong \frac{2}{\beta_{\perp 0}^2} \frac{\left(1 - \frac{\beta_{z0}}{\beta_{ph}}\right)^2}{\left(1 - \frac{1}{\beta_{ph}^2}\right)} \qquad (2.48)$$

Figure 2.7 shows an example of the efficiency given by equation (2.47) as a function of α for a given set of beam parameters close to those used in the gyro-BWO experiments. Notice that as α increases, the efficiency also increases, showing the dependence on the transverse energy of the electrons. The efficiency saturates at ~ 43% (at an α ~ 1.0) for the given parameters which, in practice, is unobtainable due to the velocity spread, voltage fluctuations, and non-optimization of the number of cyclotron turns in the actual gyro-BWO experiments.
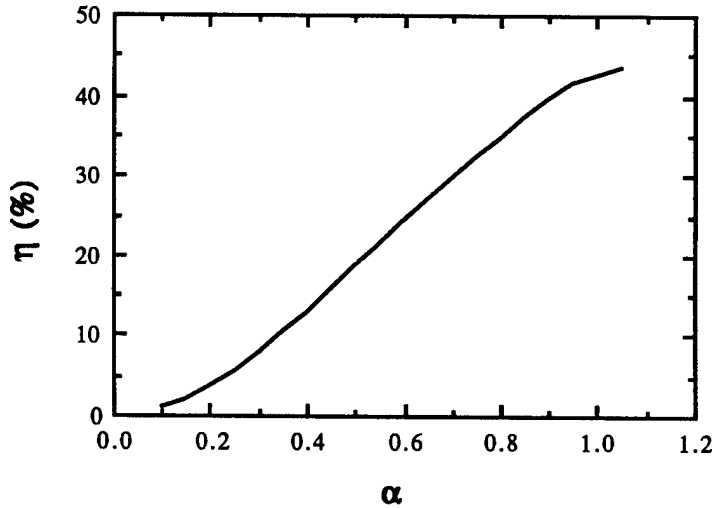


Figure 2.7. Efficiency versus α obtained from the combination of equations (2.47) and (2.48).

A non-linear numerical three-dimensional modeling of the gyro-BWO has been presented in [Gan89], and efficiencies for a uniform axial magnetic field are estimated at ~10 - 15% for a gyro-BWO that has the power extracted at the diode end, and ~3 -5% less for a reflection type gyro-BWO where the power is extracted from the forward end of the experimental set up for parameters of: beam voltage = 50 kV, beam current = 3 amps, α = 1.5, radius of the waveguide = 0.113 cm, and a magnetic field of ~45 kG.

[Gan89] has shown that if a small positive taper in the magnetic field on the exit end of the interaction cavity is employed, the efficiency can be increased to over 30%. This increase in efficiency would be due to both the dynamical change in the resonance condition given by equation (2.23) and a corresponding increase in $\alpha$, as demonstrated by Figure 2.6.

## 2.4. Threshold Beam Current for the CRM

The following equations for the beam threshold current are presented as a brief overview of the derivation given in [Fli86]. The derivation consists of using the relativistic Lorentz force equation (2.36) and the uniform external magnetic field, expressing the equations of motion in cylindrical coordinate interaction space, applying Maxwell's equations (A.32), the energy equation (2.37), and applying slow-time-scale variables to obtain slow-time-scale equations describing the interaction with a given sth harmonic.

The small signal efficiency for a uniform electromagnetic field amplitude will be the starting point presented here, and is

$$\eta_{ss} = \frac{\beta_{\perp 0}^2 F_s^2 \mu^2 \left[ -(s-b)\phi - (1-b\Delta)\mu\phi' \right]}{4 \left( 1 - \frac{\beta_{z0}}{\beta_{ph}} \right) \left( 1 - \frac{1}{\gamma_0} \right)} \tag{2.49}$$

where $F_s$ is a normalized wave amplitude given by

$$F_s = \frac{4e\omega B_{zo}}{\gamma_0 m_0 c^2 k_c^2} \frac{\left( 1 - \frac{\beta_{z0}}{\beta_{ph}} \right)^2 J_{m-s}(k_c r_0) s^s}{\beta_{\perp 0}^3 \left( 1 - \frac{1}{\beta_{ph}^2} \right)^{\frac{1}{2}} 2^s s!} \left[ \frac{\left( 1 - \frac{1}{\beta_{ph}^2} \right)^{\frac{1}{2}}}{\left( 1 - \frac{\beta_{z0}}{\beta_{ph}} \right)} \beta_{\perp 0} \right]^{s-1} \tag{2.50}$$

with s denoting the sth harmonic, $\phi$ is the characterization of the external magnetic field force acting on the electrons,

$$\phi = \frac{1 - \cos(\Delta\mu)}{(\Delta\mu)^2} \qquad (2.51)$$

$\phi'$ describes the additional inertial bunching due to the dependence of the electron axial momentum on its energy (equation (2.43))

$$\phi' = \frac{d\phi}{d(\Delta\mu)} = \frac{\sin(\Delta\mu)}{(\Delta\mu)^2} - \frac{2\phi}{\Delta\mu} \qquad (2.52)$$

$\mu$ corresponds to the total length of the interaction region

$$\mu = \frac{\beta_{\perp 0}^2}{2\beta_{z0}} \frac{\left(1 - \dfrac{1}{\beta_{ph}^2}\right)}{\left(1 - \dfrac{\beta_{z0}}{\beta_{ph}}\right)} \frac{\omega L}{c} \qquad (2.53)$$

with L being the interaction length, b characterizes the strength of the axial momentum and velocity change with the change in energy (b = 0 corresponds to the gyrotron, whereas b ~0.5 corresponds to the CARM regime)

$$b = \frac{\beta_{\perp 0}^2}{2\beta_{z0}\beta_{ph}\left(1 - \dfrac{\beta_{z0}}{\beta_{ph}}\right)} \qquad (2.54)$$

and $\Delta$ represents the kinematic phase shift

$$\Delta = sN_{opt}\delta_0 \qquad (2.55)$$

where $sN_{opt}$ is given by equation (2.48) and $\delta_0$ is the initial normalized frequency mismatch

$$\delta_0 = 1 - \frac{\beta_{z0}}{\beta_{ph}} - \frac{s\Omega_r}{\omega} \qquad (2.56)$$

The required beam threshold power is determined by the power balance equation

$$\eta I_0 V_0 = \frac{\omega W}{Q} \qquad (2.57)$$

where $V_0$ is the beam voltage, $I_0$ is the beam current, $\eta$ is the efficiency, W is the stored energy in the interaction cavity, and Q is the quality factor (neglecting wall losses)

described in section 2.5. The stored energy for a cavity that has a high reflectivity at both the input and output ends (which implies the field amplitude is essentially uniform) is given by

$$W = \frac{1}{2} \epsilon_0 L \left| B_{zo} \right|^2 \tag{2.58}$$

For small signal considerations, combining equations (2.57), (2.49), and (2.58) leads to a normalized threshold beam current of

$$\hat{I}_{thr} = \frac{b}{Q\mu \left(1 - \frac{1}{\beta_{ph}^2}\right) \left[ - (s - b)\phi - (1 - b\Delta)\mu\phi' \right]} \tag{2.59}$$

where the normalized current, $\hat{I}$, is given by

$$\frac{\hat{I}}{I_0} = \frac{8e\omega\mu_0\beta_{ph}}{\gamma_0 m_0 c k_c^2 \beta_{\perp 0}^4} \frac{\left(1 - \frac{\beta_{z0}}{\beta_{ph}}\right)^3 J_{m-s}(k_c r_o)}{\left(1 - \frac{1}{\beta_{ph}^2}\right)} \left\{ \frac{s^s}{2^s s!} \left[ \frac{\left(1 - \frac{1}{\beta_{ph}^2}\right)^{\frac{1}{2}}}{\left(1 - \frac{\beta_{z0}}{\beta_{ph}}\right)} \beta_{\perp 0} \right]^{s-1} \right\}^2 \tag{2.60}$$

## 2.5. The Quality Factor

The quality factor of an open microwave cavity mentioned in equation (2.59) and equation (2.57) consists of two parts: a resistive (or ohmic) quality factor that comes about from wall losses, and a diffractive quality factor which results from the microwave energy coupling out of the cavity. The total quality factor acts as capacitors in series, that is

$$\frac{1}{Q} = \frac{1}{Q_R} + \frac{1}{Q_D} \tag{2.61}$$

where $Q_R$ is the resistive quality factor, and $Q_D$ is the diffractive quality factor.

Typically $Q_R$ is much greater than $Q_D$, and thus $Q \sim Q_D$. The diffractive quality factor for open microwave cavities with sufficiently large wave reflections at both the input and output ends is [Fli86]

$$Q = 2 \beta_{ph} \frac{\omega L}{c} \frac{1}{1 - R_1 R_2} \qquad (2.61)$$

where L is the length of the cavity, and $R_1$ and $R_2$ are the reflection coefficients at the two ends of the cavity. Since the interaction cavity employed in the gyro-BWO experiment is a straight section of copper tubing, the reflection coefficients can be calculated using transmission line theory,

$$R = \frac{Z_{dt} - Z_{ic}}{Z_{dt} + Z_{ic}} \qquad (2.62)$$

where the subscript 'dt' refers to the surrounding drift tube, and subscript 'ic' refers to the interaction cavity. Z is the wave impedence given by equation (A.46).

## 2.6. Absolute Instability

The absolute instability of the gyro-BWO has been investigated extensively, and relevent literature on the subject appears in [Lau81, Par84, Dav89, Dav90]. The following discussion follows that of [Lau81].

From the dispersion relation described in equation (2.18), one can see that near resonance where the instabilities occur, the $W_{sm}$ term will dominate the $Y_{sm}$ term, thus the $Y_{sm}$ term can be neglected. Also near resonance, equation (2.22) is valid which leads to the following simpler dispersion equation of,

$$(\omega^2 - k_c^2 c^2 - k_z^2 c^2)(\omega - k_z v_z - s\Omega_r)^2 = \frac{- \omega_{pe}^2 \beta_\perp^2 H_{sm} k_c^2 c^2}{K_{mn}} \qquad (2.63)$$

Normalizing with respect to the cutoff frequency, $\omega_c$, leads to the following dispersion equation,

$$D = (\hat{\omega}^2 - \hat{k}^2 - 1)(\hat{\omega} - \hat{k}\beta_z - sb)^2 = - \varepsilon \qquad (2.64)$$

where

$$\hat{\omega} = \frac{\omega}{\omega_c}$$

$$\hat{k} = \frac{k}{k_c}$$

$$b = \frac{\Omega_r}{\omega_c}$$

$$\varepsilon = \frac{\omega_{pe}^2 \beta_\perp^2 H_{sm}}{\omega_c^2 K_{mn}} \qquad (2.65)$$

Here b is proportional to the magnetic field, and $\varepsilon$ is a measure of the electron beam strength (through the plasma frequency). The parameters used in the gyro-BWO experiments ($TE_{11}$, s=1, $\alpha$ = 0.65, E = 650 kV, B = 5.0 kG, cavity radius = 1.93 cm) gives an $\varepsilon$ of

$$\varepsilon = 3.30 \times 10^{-7} \, I_b \qquad (2.66)$$

where $I_b$ is the electron beam current in amps.

For frequency intersections that occur on the right-hand side ($k_z > 0$) of the dispersion plot (see, for example, Figure 2.4), the uncoupled ($\varepsilon$ = 0) dispersion equation, D = 0, must be solved along with,

$$\left. \frac{\partial D}{\partial k} \right|_{\omega_s, k_s} = 0 \qquad (2.67)$$

to obtain the saddle-point (or pinch-point) values at which the roots of the k-plane merge together. After finding the saddle point, the solutions are placed into equation (2.64) and a critical value for $\varepsilon$ is obtained at which the absolute instability occurs.

An absolute instability exists only if two of the imaginary roots of the k-plane, one in the positive imaginary plane, and the other in the negative imaginary plane, merge together at a single point (see Figure 2.8) as $\omega_s$ tends to $\omega_s$ - i$\infty$. Figure 2.8(a) shows the convective instability, in that the merging roots occur from the same side of the imaginary plane. Note that only one of the roots tends towards +$\infty$ and is the waveguide mode that travels in the opposite direction of the beam velocity (the 'backward-wave') From Figure 2.8(b), it becomes obvious that an absolute instability exists only if one of

the merging roots is from the backward wave mode of the waveguide, since only this mode exists on the opposite side of the imaginary plane from the other roots of k. Note that this shows that whenever $k_z < 0$ and the electron beam current is greater than zero, the absolute instability will always occur. This is the instability associated with the gyro-BWO mechanism. Also note that even though an absolute instability exists only for a root involving the backward wave mode of the waveguide, forward wave intersections can still exhibit an absolute instability at very high currents, since both modes (the forward and backward) will be strongly coupled and will provide an internal feedback mechanism allowing for the possible excitation of the absolute instability.
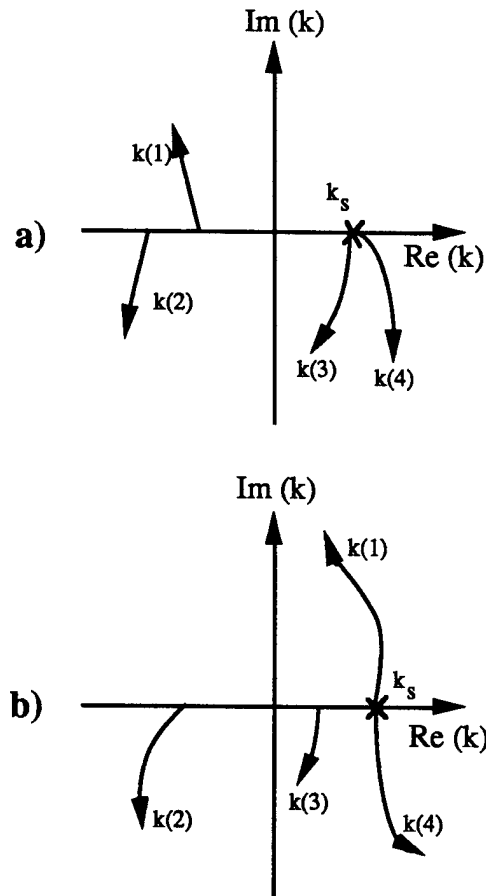


Figure 2.8. A plot showing the merging of the k-plane roots; a) is the convective instability; b) is the absolute instability. k(1) corresponds to the backward-wave mode of the waveguide.

## 2.6.1 Absolute Instability Growth Rates

The growth rates for the absolute instability (and the existence of the absolute instability) can be found using the formalism presented by Davies [Dav90]. Beginning with the normalized Green's function, which gives the response of the mode to a delta-function disturbance $\delta(z)\delta(t)$,

$$\hat{G}(z = vt, t) = \frac{G}{\omega_c} \tag{2.68}$$

This Green's function has a time-asymptotic behavior of:

$$\frac{\ln(\hat{G})}{t} \sim \frac{Im(\hat{\omega}'_s)}{\gamma_v} \tag{2.69}$$

where $\hat{\omega}'_s$ is the saddle-point (or pinch-point) coordinate for the general reference frame moving at $\beta_v = v/c$ in the spatial direction (z) in relation to the laboratory frame, and $\gamma_v = (1-\beta_v^2)^{-1/2}$. Growth rates of the convective or absolute instabilities can be found by plotting $Im(\hat{\omega}'_s)/\gamma_v$ versus $\beta_v$. If the curve encompasses the origin ($\beta_v = 0$) then absolute instability exists, and its growth rate is given by the height of the curve at $\beta_v = 0$.

The general frame (the primed system) is related to the laboratory frame (the unprimed system) by

$$ck_z = \gamma_v(ck'_z + \beta_v\omega') \tag{2.70}$$

$$\omega = \gamma_v(\omega' + \beta_v ck'_z) \tag{2.71}$$

Using equations (2.64) and (2.67) with the general frame coordinates gives,

$$\hat{k}'(\hat{\omega}' - \beta'_z\hat{k}' - sb') + \beta'_z(\hat{\omega}'^2 - \hat{k}'^2 - 1) = 0 \tag{2.72}$$

$$\beta'_z\epsilon' = \hat{k}'(\hat{\omega}' - \beta'_z\hat{k}' - sb')^3 \tag{2.73}$$

where

$$\beta'_z = \frac{(\beta_z - \beta_v)}{(1 - \beta_z\beta_v)} \tag{2.74}$$

and the $\wedge$ signifies a normalization to $\omega_c$, as was done in equation (2.65).

$$\varepsilon' = \frac{\varepsilon}{\gamma_v^2 (1-\beta_z\beta_v)^2} \qquad (2.75)$$

and $b'$ is related to b (equation 2.65)

$$b' = \frac{b}{\gamma_v (1-\beta_z\beta_v)} \qquad (2.76)$$

When $sb' > 1$, approximate saddle-point coordinates can be obtained by solving

the uncoupled beam and waveguide dispersion relations, linearizing and keeping small

terms. This leads to

$$\hat{\omega}'_{s+} = \hat{\omega}'_+ + \frac{3}{4} \frac{(\hat{k}'^2_+ \mid \beta'_z \mid \varepsilon')^{\frac{1}{3}}}{(\hat{k}'_+ - \beta'_z \hat{\omega}'_+)} (1 + i\sqrt{3}) \qquad (2.77)$$

$$\hat{\omega}'_{s-} = \hat{\omega}'_- + \frac{3}{4} \frac{(\hat{k}'^2_- \mid \beta'_z \mid \varepsilon')^{\frac{1}{3}}}{(\beta'_z \hat{\omega}'_- - \hat{k}'_-)} (1 + i\sqrt{3}) \qquad (2.78)$$

Equation (2.77) is referred to the upshifted pulse (the upper frequency intersection as in

Figure 2.3) and is valid when $\beta'_z < 0$, and equation (2.78) is referred to as the

downshifted pulse (the lower frequency intersection as in Figure 2.3) and is valid when

$\beta'_z > 0$. Exact solutions of equations (2.72) and (2.73) are required when the conditions

of validity for equations (2.77) and (2.78) are not met, and when $sb' < 1$. Note that

equations (2.77) and (2.78) show the current dependence of the growth rate. More

current means a greater growth rate, as evidenced from $\varepsilon'$, and goes as $I_b$ to the one-third

power.

Equations (2.77), (2.78) and (2.69) provide the growth rates shown in Figures

2.9 - 2.12. Note that all the downshifted pulses represent an absolute instability because

the pulses encompass the origin ($\beta_v = 0$). The parameters used to obtain the growth rates

are listed in the figure captions. Figure 2.9 shows how the absolute instability growth

rate increases as a function of the current. As the current increases, the growth rate also

increases (as mentioned above). Figure 2.10 shows the growth rate comparison between the fundamental mode (s = 1), the second harmonic (s = 2) and the third harmonic (s = 3). Notice that the greatest growth rate is for the fundamental mode, thus the fundamental mode should dominate. This is observed experimentally, as discussed in Chapter IV. Figure 2.11 demonstrates the effect of increasing the magnetic field. As the magnetic field is increased, the growth rate of the absolute instability increases, even though the overall height of the pulse shape has decreased. Figure 2.12 shows the absolute instability growth rate for two different modes, the $TE_{11}$ and $TE_{21}$. Notice that the $TE_{21}$ mode is barely an absolute instability. This comes about due to the high current used (1500 amps), even though the actual dispersion relation (Figure 4.16) shows the intersection to lie on the right-hand side of the plot (a forward wave). This suggests that the fundamental $TE_{21}$ mode absolute instability might be a competing interaction to the $TE_{11}$ fundamental mode backward-wave. This may have been observed experimentally, as discussed in Chapter IV.
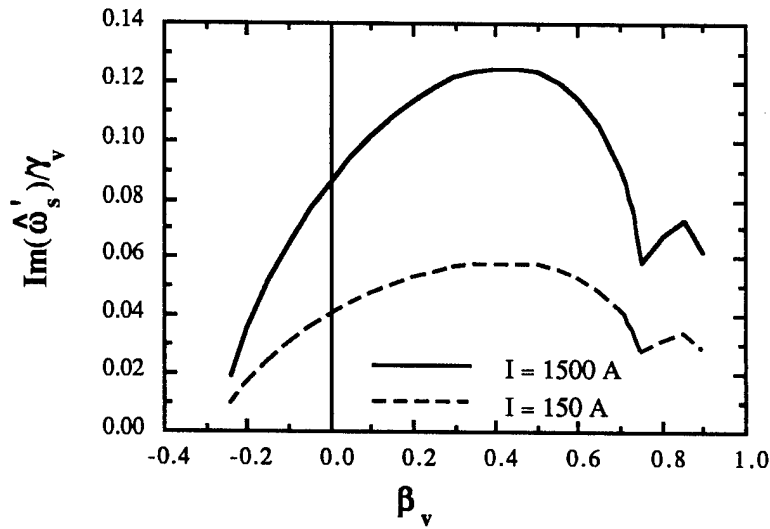
Figure 2.9. A comparison of the absolute instability growth rates for different currents. The 1500 amp result is the solid beam current, and the 150 amp result is the annular beam current. Parameters used are: $TE_{11}$, fundamental mode, B = 5.0 kG, beam radius of 1.2 cm, $\alpha$ = 0.65, V=750 kV.
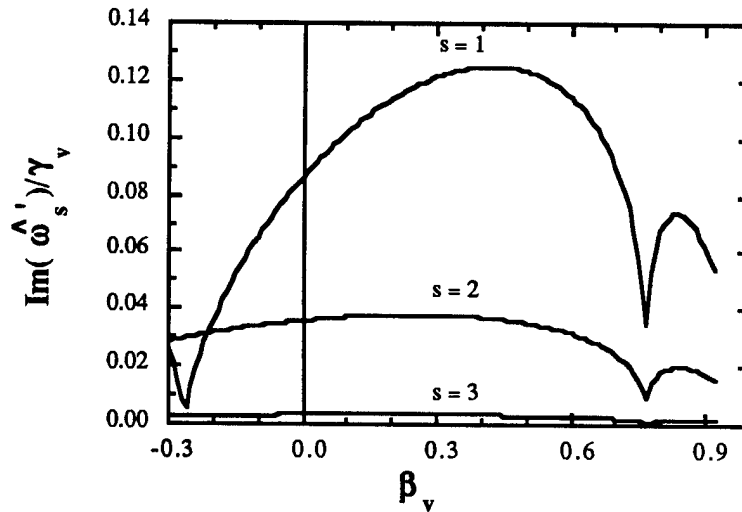


Figure 2.10. A comparison of the absolute instability growth rates for different harmonics: the fundamental mode (s = 1), the second harmonic (s = 2) and the third harmonic (s = 3). Parameters used are: $TE_{11}$, I = 1500 amps, B = 5.0 kG, beam radius of 1.2 cm, $\alpha$ = 0.65, V=750 kV.
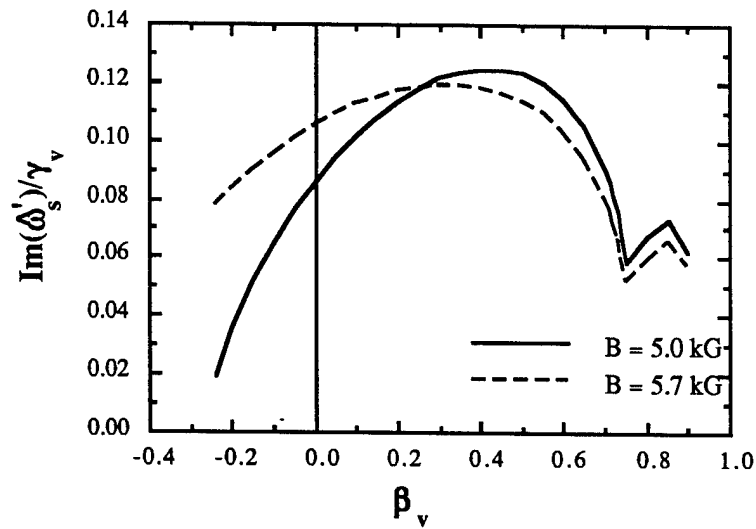
Figure 2.11. A comparison of the absolute instability growth rates for different magnetic fields. Parameters used are: $TE_{11}$, fundamental mode, I = 1500 amps, beam radius of 1.2 cm, $\alpha$ = 0.65, V=750 kV.
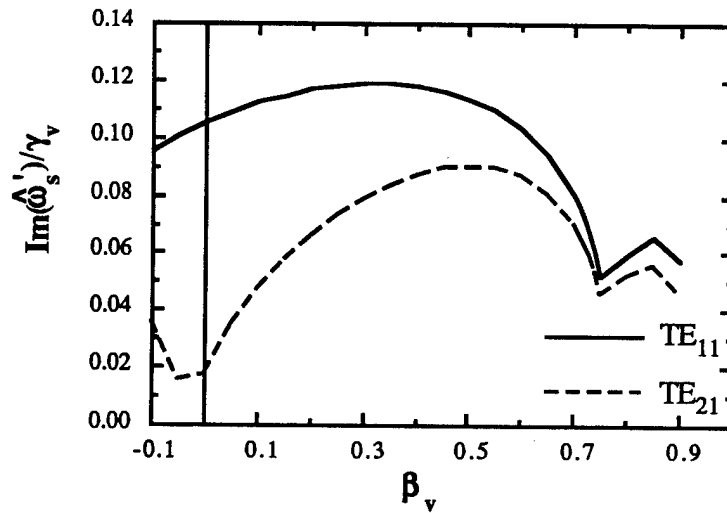
Figure 2.12. A comparison of the absolute instability growth rates for the $TE_{11}$ and $TE_{21}$ modes. Parameters used are: Fundamental mode, B = 6.8 kG, beam radius of 1.2 cm, $\alpha$ = 0.65, V=750 kV.

# CHAPTER III
# EXPERIMENTAL CONFIGURATION AND ELECTRON BEAM
# CHARACTERIZATION

The basic experimental configuration used in the gyro-BWO experiments is shown in Figure 3.1. The individual components are described in greater detail below.

## 3.1 Diode and Interaction Cavity Magnetic Fields

Two sets of magnetic field coils are used in the experiments, one in the diode region and the other in the interaction cavity region, each pulsed independently. The pulsed diode magnetic field of up to ~900 gauss (variable by changing the current through the magnet coils) is provided by five 'pancake' type magnets. The exact specifications of these magnets are described elsewhere [Cun89]. There are two reasons for charging and pulsing this field independently of the maser solenoidal magnetic field (the interaction cavity B-field). One reason is that the diode field tends to suppress radial 'edge' emission-induced arcing which degrades both the cathode surface and voltage pulse (discussed in more detail in section 3.3). The second reason is that when used in conjunction with the maser solenoidal field, the beam velocity ratio, $\alpha = v_\perp / v_\parallel$, can be varied by changing the magnetic field ratios between the two magnetic fields. This can be shown from a simple adiabatic invariant argument which shows the relationship of $\alpha$ to the magnetic fields by,

$$\alpha_m = \alpha_d \sqrt{\frac{R}{1 + \alpha_d^2(1-R)}} \qquad (3.1)$$

where $\alpha_m$ is the velocity ratio in the maser solenoidal magnetic field, $\alpha_d$ is the velocity

36
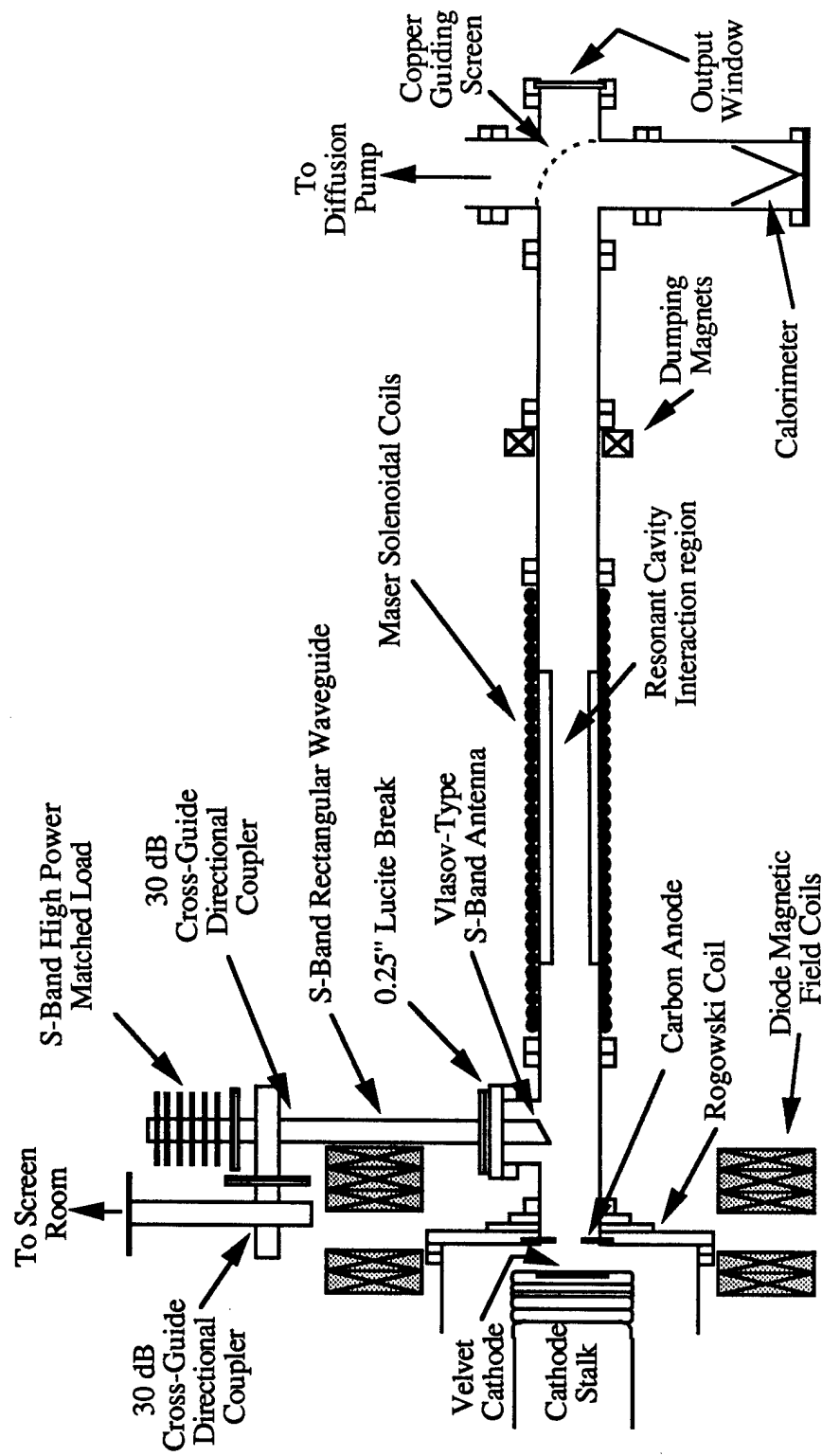
**Figure 3. 1 Gyro-BWO Experimental Configuration**

ratio in the diode region and R is the magnetic field ratio of the maser solenoidal magnetic field to the diode region magnetic field.

The on-axis pulsed diode magnetic field is measured using an Hall effect axial magnetic field probe (Bell Gaussmeter 610). Figure 3.2 plots the magnetic field in G/A (gauss/amp) as a function of position for the diode magnetic field configuration used for the experiments. The values shown in the plot are for a 104 ms delay, which is the time needed for the magnetic field to reach its maximum value when penetrating the aluminum chamber encompassing the diode field region and penetrating the magnet coils.
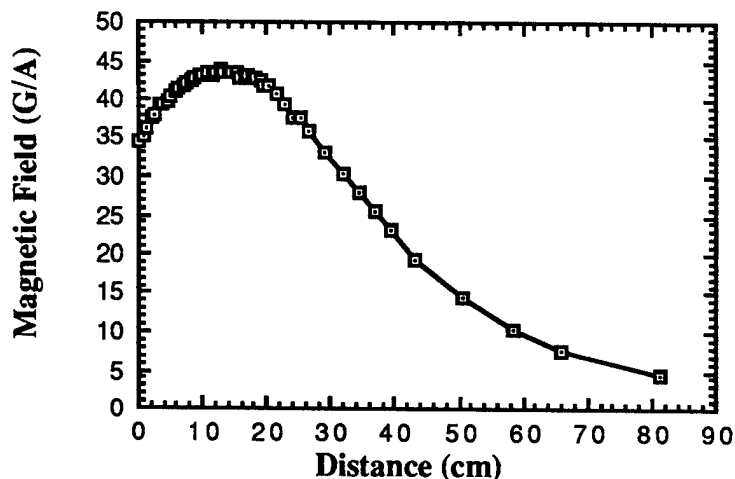


**Figure 3.2. Diode magnetic field (G/A) as a function of distance from the cathode (A-K gap = 6.9 cm, corresponding to two 2 cm and one 1.0 cm spacing rings). Zero cm corresponds to the velvet emitting surface. A distance of 4.75 cm corresponds to the front flange of the diode chamber. Values are for a 104 ms time delay.**

The maser solenoidal field is provided by an 80.5 cm long, four inch diameter stainless steel tube wrapped by two layers of 12 gauge copper wire. A Marx-like two-stage double-polarity (± 450 V) SCR switched capacitor bank provides a pulsed current that allows magnetic fields of 3.0 - 6.8 kG to be obtained. Numerical time integration (direct integration of a B-dot loop signal on a Tektronix DSA 602 digitizing scope ) is used to measure the magnetic field (calibrated with the gaussmeter used in the diode magnetic field measurements), with Figure 3.3 showing the G/A as a function of

position for the solenoid. Typically, this magnet current is measured by a Pearson

current transformer, Model 301X (0.01 V/A), on a 5335 Tektronix storage oscilloscope.

The magnetic field is essentially uniform beginning about 15 cm from either end of the

solenoid, thus the interaction cavity can be of ~ 50 cm in length.
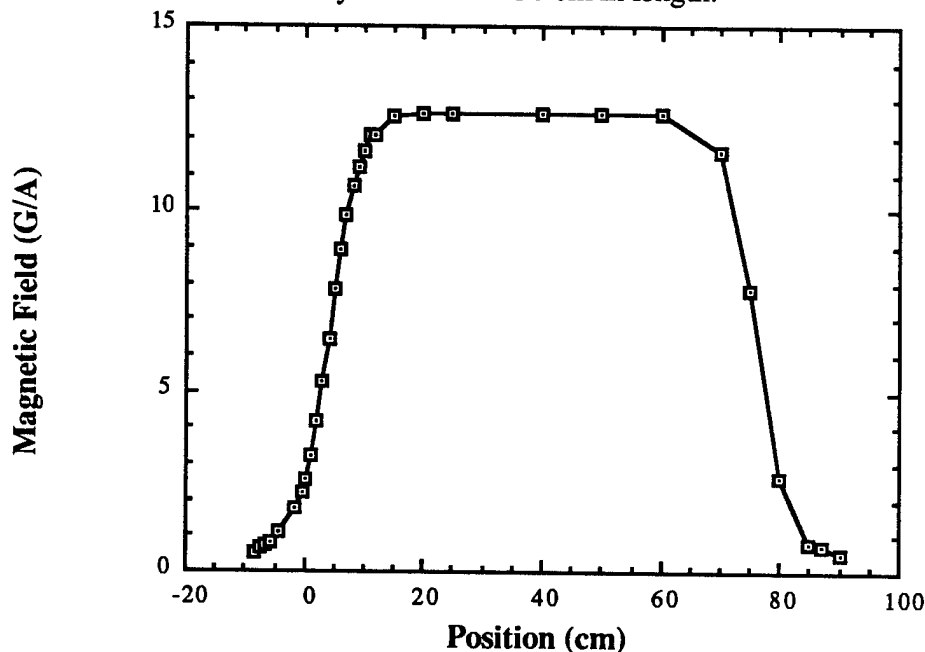


Figure 3.3. Maser solenoidal magnetic field (G/A) as a function of position. Zero cm corresponds to the start of the 4" drift tube. Values are for a 6 ms time delay.

## 3.2 MELBA

The long-pulse electron beam generator used in the experiments is MELBA

(Michigan Electron Long Beam Accelerator). MELBA is a Marx type generator in that it

charges capacitors in parallel and discharges them in series. MELBA consists of a seven

stage Marx generator and a single reverse-charged Abramyan [Abr77] stage which allows

a more uniform ('flatter') voltage pulse over a long time scale ( > 1 µs ). This occurs

because the reverse-charge stage 'rings' in the opposite direction of the other seven

stages, tending to dampen the initial LRC circuit overshoot, while boosting the voltage in

the latter stages of the pulse as in Figure 3.4. The use of an Abramyan stage allows for

an output voltage that varies by a few percent over long pulses ( 0.5 - 1.5 μs ). A side

view of the MELBA accelerator showing the Abramyan stage is shown in Figure 3.5.

Each stage of the Marx generator consists of two 1 μF, 100 kV capacitors. One

capacitor in an individual stage is charged positively, the other negatively (parallel

charging), and then discharged in series by applying a trigger signal to a series of $SF_6$

gas insulated spark gaps. The output voltage then travels to a vacuum diode load through

a current limiting resistance (~2.8 Ω), an RC filtering circuit, and across a graded

insulating stack ( used to uniformly distribute the diode voltage along the insulator ) to

prevent 'flashing' of the insulator [Mil82]. A triggered crowbar switch allows the output

voltage pulselength to be selected, usually in the 0.5 - 1.5 μs range. Figure 3.4 shows a

typical voltage pulse generated by MELBA. Using MELBA with a matched load (100 Ω)

gives the following peak output parameters: voltage ~ 1 MV; current ~ 10 kA; pulselength

~ 0.5 - 4.0 μs; and ± 10 % voltage fluctuation along the 'flat-top' (1.5 μs pulselength).

When the capacitors are charged to ± 57 kV, MELBA generates a flat-top voltage of

~700- 750 kV. A more in-depth description of MELBA appears elsewhere [PSI83].
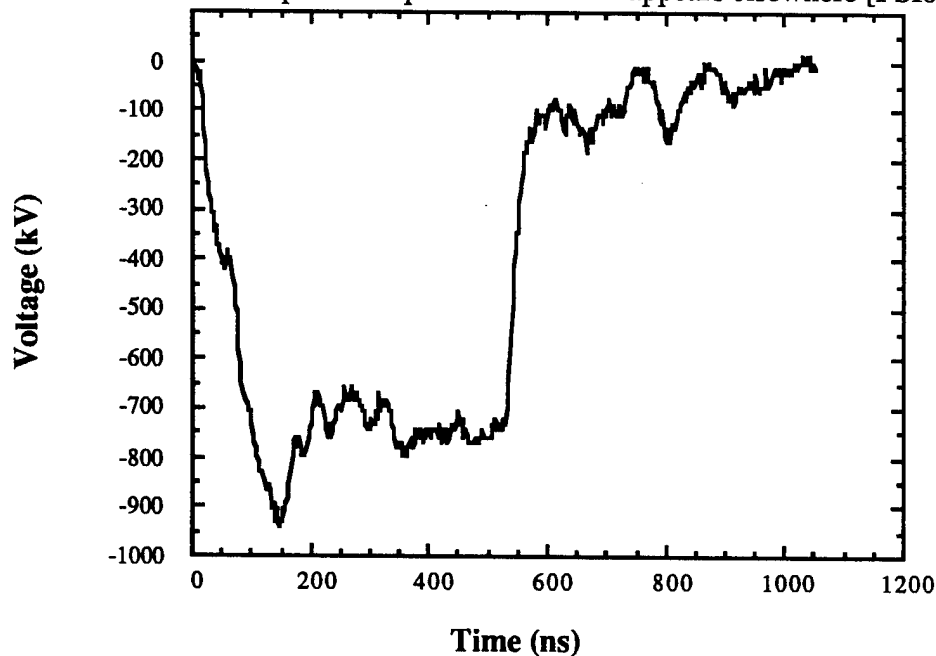


Figure 3.4. Typical MELBA Voltage Pulse used in the Gyro-BWO
Experiments.

41
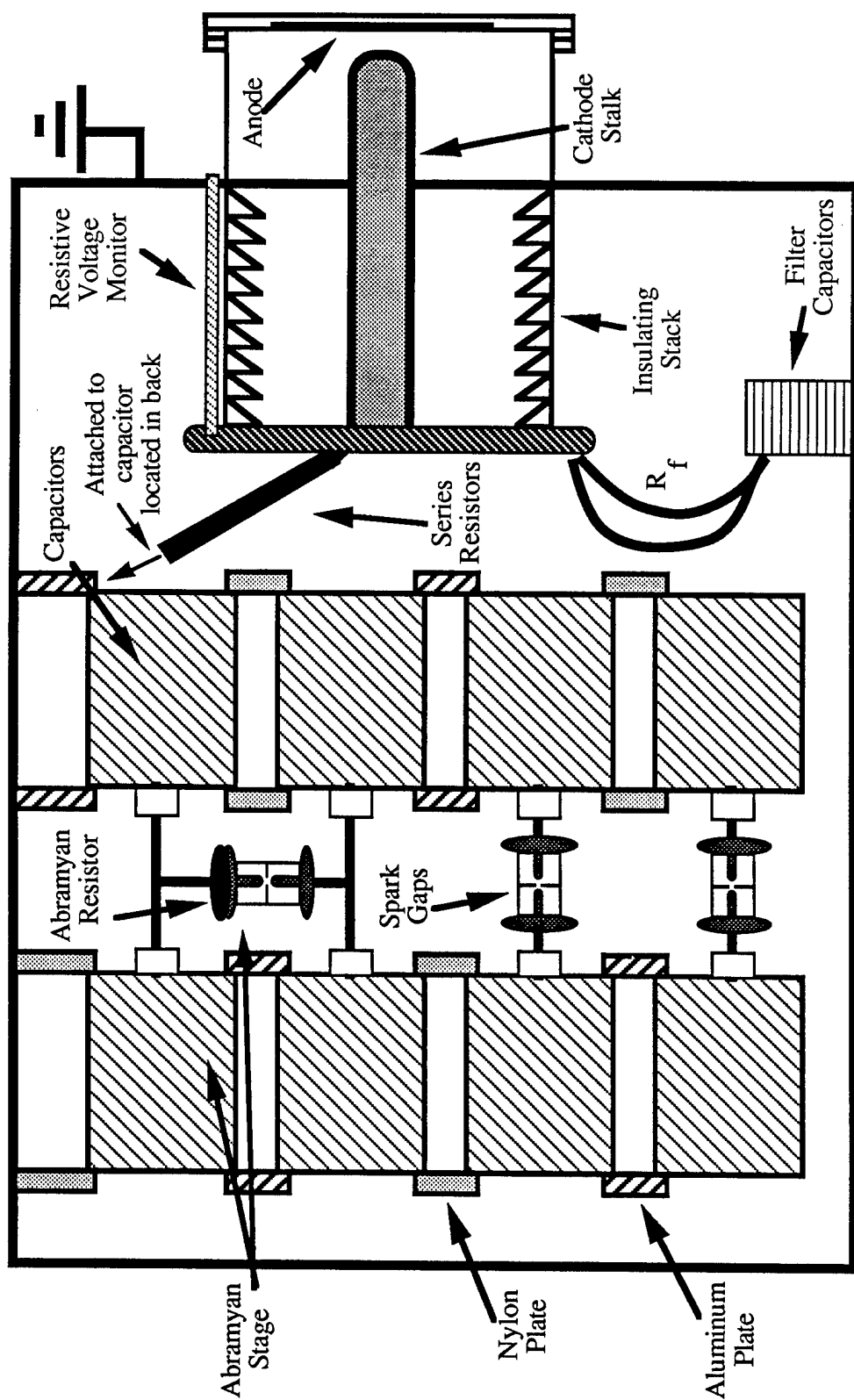


**Figure 3.5.** MELBA side view, showing the Abramyan stage.

## 3.3 Diode and Electron Beam Characterizations

Once the high voltage pulse traverses the insulating stack, the energy is converted to an electron beam (e-beam) by explosive emission from a cotton velvet-covered aluminum cathode ( also known as a 'cold-cathode' [Nat83] ). Plasma forms at the cathode surface, which then expands across the Anode-Cathode (A-K) gap region. To produce long e-beam pulses, the A-K gap must be kept relatively large (in comparison with the cathode radius) in order to avoid the plasma shorting out the diode by filling the diode A-K gap (known as gap closure). Typical cathode plasma closure velocities of 2 - 6 cm/$\mu$s have been observed in long-pulse diodes [Gil85].

To obtain long-pulse, high power microwaves, it is important to be able to generate long, 'flat-top' voltage pulses, without a substantial amount of fluctuation. Because of the relatively large A-K gaps of the MELBA experiments, radial 'edge' emissions from the cathode are important and tend to degrade the overall voltage pulse, hindering the generation of long, flat voltage pulses. In order to suppress radial 'edge' emissions, the cathode stalk has a corona ring (designed to reduce electric field enhancement [Luc88]) placed around the velvet emitting surface (See Figure 3.6). Electron emission from the cathode is substantial when a MV potential is applied to the cathode. To reduce the emission of electrons from the aluminum surfaces of the cathode, the exposed aluminum surfaces are coated with glyptal (glyptal 1201-A red insulating enamel, available from General Electric Supply, Inc.). This is done in order to ensure emission from only the velvet emitting surface; after several shots the glyptal begins to degrade and field emission spots become apparent on the corona ring and cathode stalk leading to a degradation of the overall voltage pulse. Diode closure experiments are also performed to test other means of suppressing radial 'edge' emissions, and are described in more detail below.

Glyptal Painted
Aluminum Shield
(Corona Ring)

Brass Threaded
Rod

7 cm
radius

3.8 cm radius

Velvet Cotton
or
Carbon Graphite
Felt

2 cm
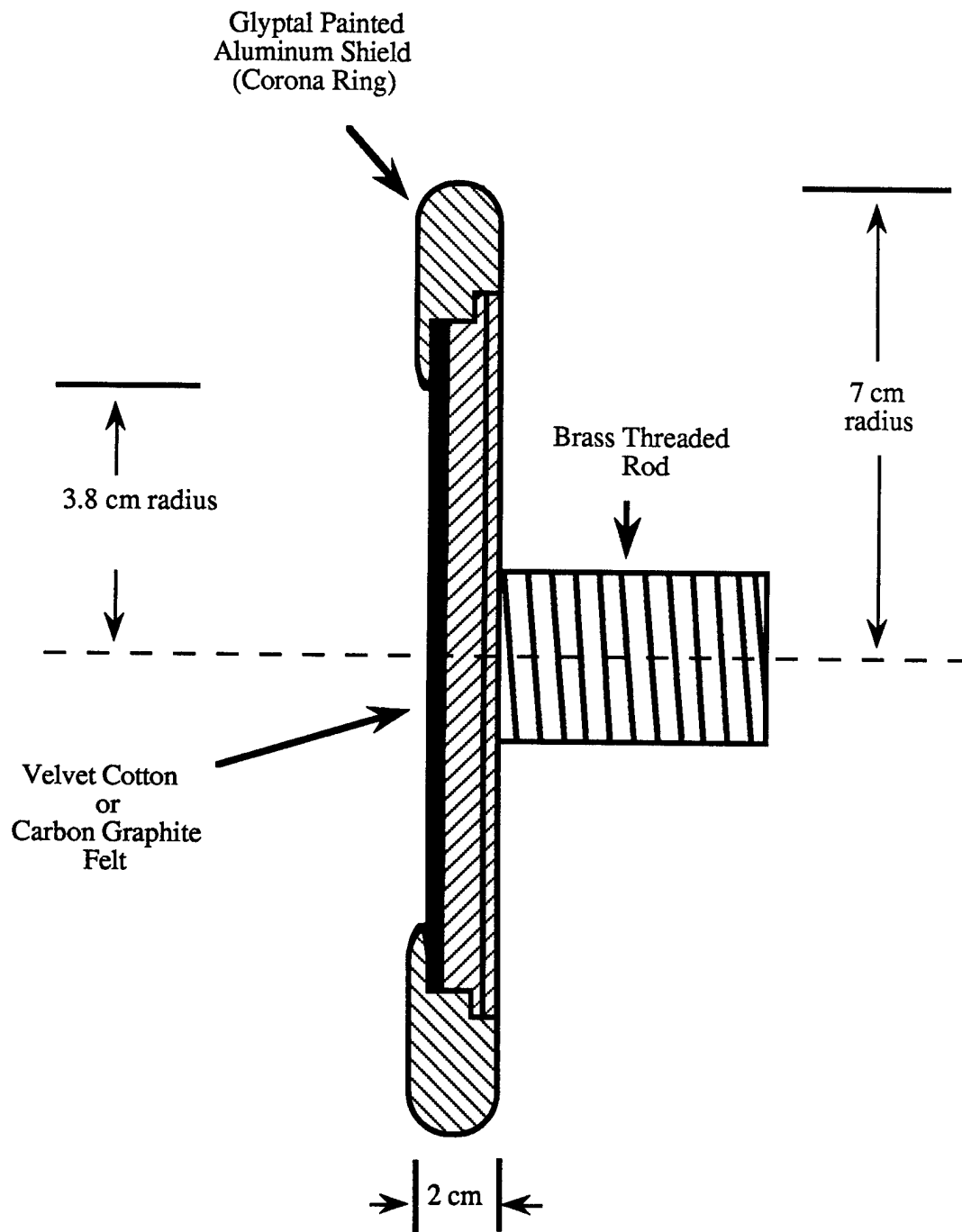
Figure 3.6. Corona Ring design (after Lucey [Luc88]).

Three different anodes of 1/8" thick POCO graphite plates are used to control the
quality and the amount of electron beam current admitted to the interaction region. The
first is an 80 hole, ~1 mm diameter, apertured-mask anode with a major radius of 2.52
cm. This anode plate was used to provide a high quality beam with estimated axial
velocity spread of $\Delta\beta_{\parallel}/\beta_{\parallel} \leq 4$ % and axial energy spread of $\Delta\gamma_{\parallel}/\gamma_{\parallel} \leq 7$ %, and a beam
velocity ratio $\alpha = v_{\perp}/v_{\parallel}$ of ~ 0.6. These values were obtained by using a Cerenkov plate
diagnostic [Cho91]. This anode plate admits ~40 - 80 amps of electron beam. The
second anode plate used is a 24 hole, ~4.8 mm diameter, apertured-mask anode with a
major radius of 2.52 cm. This anode plate provides ~ 100 - 450 amps of electron beam,
and an $\alpha$ ~ 0.4 - 0.7. The third anode plate is a 2.54 cm radius open hole to provide a
solid beam. This beam is of relatively poor quality with an $\alpha$ ~ 0.05 - 0.7, but provides
1-2 kA of electron beam current.
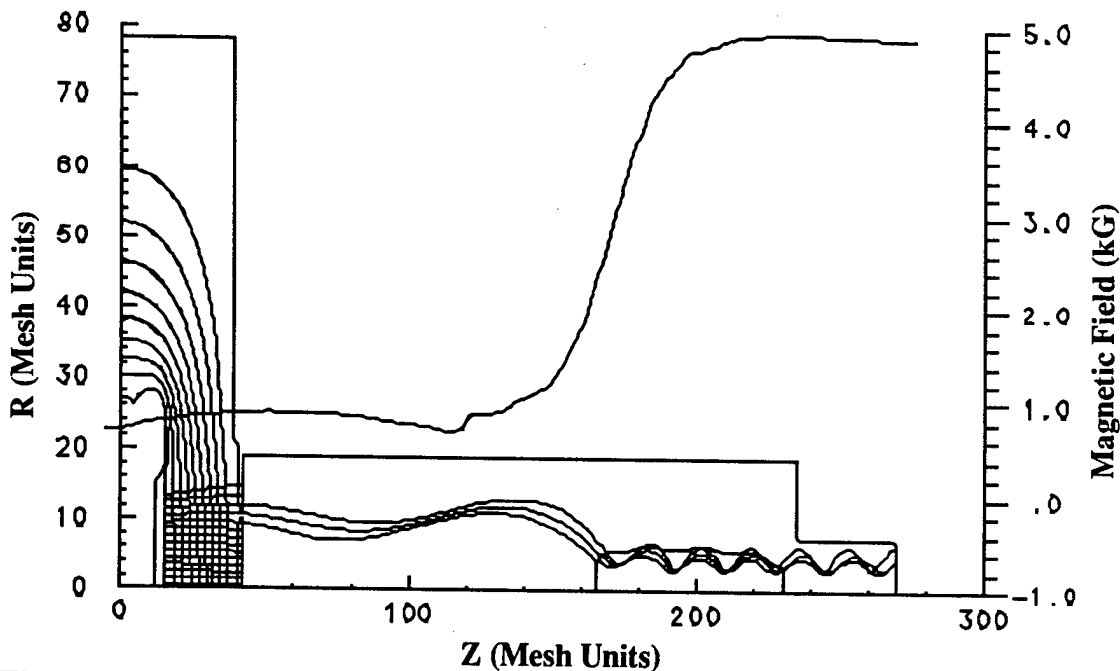


**Figure 3.7.** EGUN result showing the electron beam trajectory for the 24
hole apertured-mask anode, with voltage of 750 keV, A-K Gap of 6.9
cm, and interaction cavity radius of 1.93 cm. The beam current that
reaches the entrance of the tube is approximately 150 amps, with $\alpha$
varying from 0.4 - 0.7 (average of 0.5) from the center to the outer
edge of the propagated beam.

An electron trajectory code (EGUN code [Her79]) is used to simulate the electron

beam dynamics and obtain the $\alpha$ spread for the different anode plates. Figures 3.7 and

3.8 show the electron beam trajectories for the masked apertures and solid beam anode

plates. The Cerenkov plate diagnostic agrees well with the EGUN results for the eight

hole, 1 mm diameter, apertured-mask anode, thus the EGUN results are used as a basis

for finding $\alpha$ for the 24 hole apertured-mask anode and the solid beam. The EGUN

results are used since a Cerenkov plate would be 'washed-out' and would probably not

be a useful diagnostic for obtaining $\alpha$ information for the 24 hole apertured-mask anode

or from a solid beam (especially one of 1 - 2 kA, which would likely shatter the thin glass

plates).
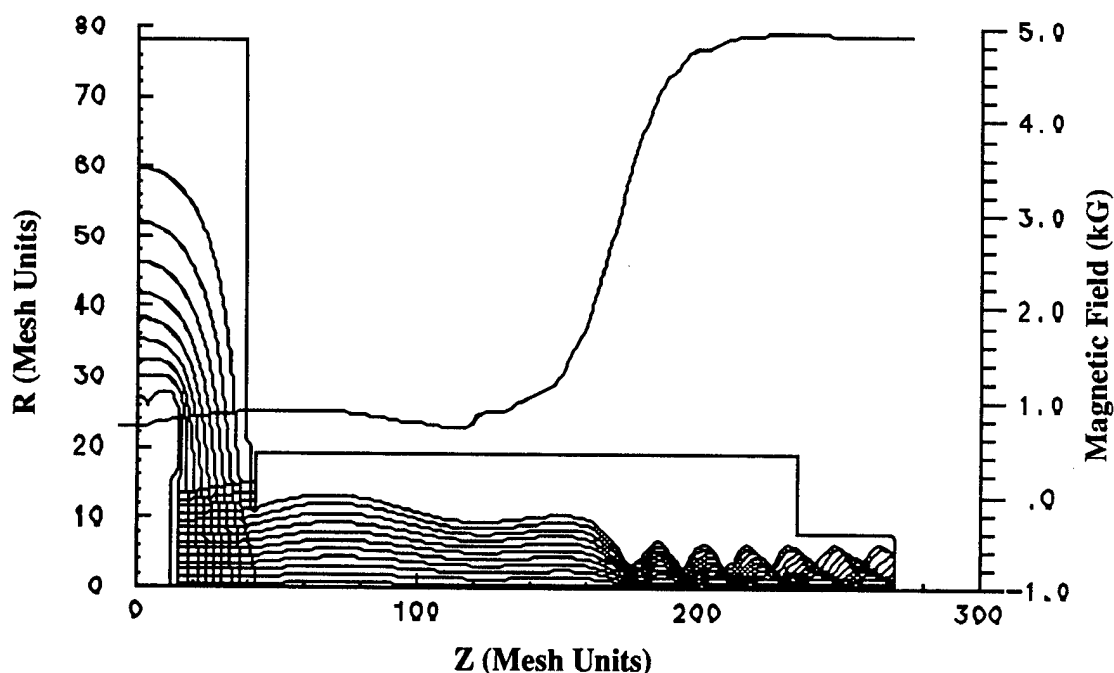


**Figure 3.8.** EGUN result showing the electron beam trajectory for the
5.1 cm diameter hole anode, with voltage of 750 keV, A-K Gap of 6.9
cm, and interaction cavity radius of 1.93 cm. The beam current that
reaches the entrance of the tube is approximately 850 amps, with $\alpha$
varying from 0.04 - 0.7 (average of 0.5) from the center to the outer
edge of the propagated beam.

## 3.3.1 Diode Closure Experiments

Diode closure experiments were performed in order to demonstrate the effects of two cathode shapes and three differing magnetic field conditions on the radial 'edge' emission problem. An example of the diode closure experimental setup is shown in Figure 3.9. The voltage and diode current diagnostics are described in section 3.5.1. The anode current is measured by means of four return current paths, each passing through a Pearson current transformer (Model 100, 0.1 V/A). A calibrated summing
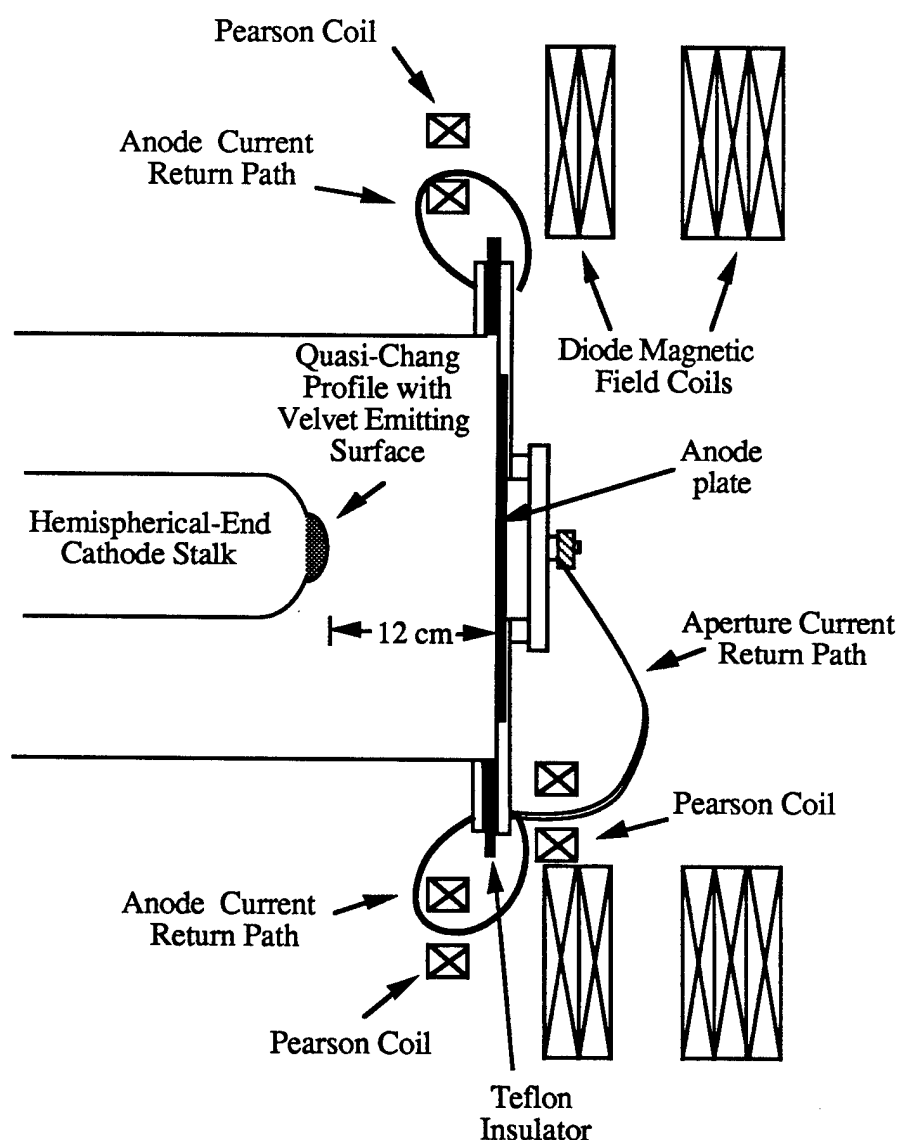


**Figure 3.9. An example of the diode closure experimental setup.**

Hemispherical-End Cathode

Quasi-Chang Profile
Covered with
Cotton Velvet

6.985 cm

3.925 cm

3.1 cm

55°

5.35 cm

16°

0.375 cm

1 cm

2.2 cm
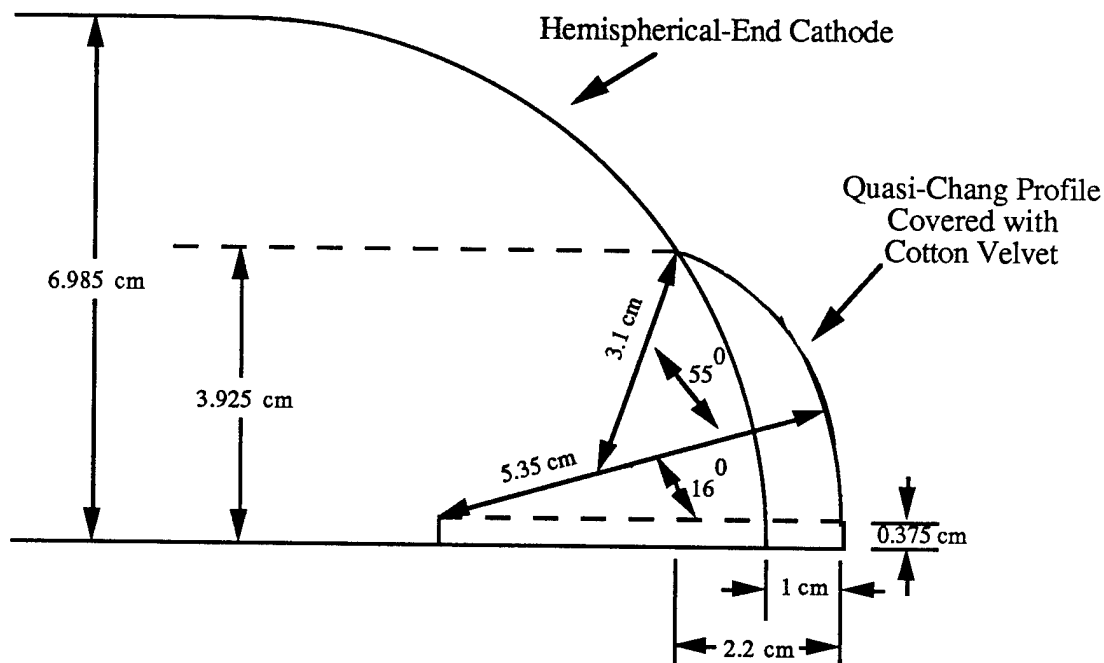
**Figure 3.10. Dimensions of the quasi-Chang profile attached to the hemispherical-end cathode stalk.**

circuit is used to sum the four signals from the Pearson transformers in order to obtain the total anode current. A teflon insulator is used to isolate the diode chamber from the anode to measure the amount of diode current that reaches the anode (referred to as anode current).

The diode closure experiments consisted of two different cathode shapes, the first being a planar cathode stalk with a Corona Ring (Figure 3.6) using a carbon graphite felt emitting surface (at an A-K gap of 8.1 cm), and the second a hemispherical-end (HE) cathode stalk with a quasi-Chang [Cha72,Gil90] profile using a velvet emitting surface (Figure 3.10) attached to the end of the cathode stalk (using an A-K gap of ~12 cm). The three different magnetic field conditions are: 1) no magnetic field; 2) a gradient magnetic field (with a gradient of ~25 - 30 %); and 3) a uniform magnetic field. The gradient and uniform magnetic fields are obtained by positioning the diode magnetic field coils at different distances from the cathode. In order to analyze the diode closure results, the following background of electron beam current behavior is necessary.

The space-charge limited emission can be described by the Child-Langmuir (C-L) law for a particular diode geometry. If the aspect ratio of the cathode radius ($r_c$) to the A-K gap (d) is large ($r_c/d \gg 1$) then the following non-relativistic C-L relation (known as the planar C-L law) can be used:

$$J = (2.34 \times 10^{-6}) \frac{V^{\frac{3}{2}}}{d^2} \qquad (3.2)$$

where J is the current density (amps/cm$^2$), and V is the voltage (volts). The A-K gap starts at d (cm) and is assumed to be a time varying quantity, given by

$$d = d_0 - vt \qquad (3.3)$$

where $d_0$ is the initial A-K gap (cm), v is the diode closure velocity (cm/$\mu$s), and t is the time ($\mu$s).

The current (in amps) can then be written as,

$$I = (2.34 \times 10^{-6}) \frac{A_{eff} V^{\frac{3}{2}}}{d^2} \qquad (3.4)$$

with $A_{eff}$ (cm$^2$) being the 'effective' area of the cathode plasma, which is assumed to be uniform and given by $\pi r_0^2$ ($r_0$ being the cathode plasma radius in cm). The planar perveance is then given by

$$P_p = (2.34 \times 10^{-6}) \frac{\pi r_0^2}{d^2} \qquad (3.5)$$

where perveance is defined as

$$P = \frac{I}{V^{\frac{3}{2}}} \qquad (3.6)$$

Solving for d from equation (3.5),

$$d = \sqrt{\frac{(2.34 \times 10^{-6}) A_{eff}}{P_p}} \qquad (3.7)$$

Using measured current and voltage results from the diode closure experiments, the A-K gap distance is calculated from equation (3.7), and compared with the expected result

from equation (3.3) to determine the closure velocity. Equations (3.2) - (3.5) and (3.7) are referred to as the planar model.

Since the diode configuration of MELBA typically has a large A-K gap, the aspect ratio is generally less than one, and the above equation can only be used as an approximation. This is due to the fact that radial 'edge' emission now becomes important and a different C-L relationship combining both planar and radial emissions should be used. Such a relationship has been approximated (Par74) by combining both the planar C-L and radial C-L relationships, where the radial C-L relationship is given by

$$I = (1.83 \times 10^{-6}) \frac{2\pi r_0}{d_0 \beta^2} V^{\frac{3}{2}} \tag{3.8}$$

which gives the radial perveance

$$P_r = (11.5 \times 10^{-6}) \frac{r_0}{d_0 \beta^2} \tag{3.9}$$

where $r_0$ is the cathode plasma radius, $d_0$ is the initial A-K gap spacing (the shortest distance to the anode), and $\beta$ is the 'geometric edge factor' defined by

$$\beta = \ln\left(\frac{d_0}{vt}\right) - \frac{2}{5}\left(\ln\left(\frac{d_0}{vt}\right)\right)^2 + \frac{11}{120}\left(\ln\left(\frac{d_0}{vt}\right)\right)^3 - \frac{47}{3300}\left(\ln\left(\frac{d_0}{vt}\right)\right)^4 \tag{3.10}$$

where $v$ is the closure velocity, and $t$ is the time as defined above in the planar model. Equations (3.8) - (3.10) are referred to as the radial model. These two models are combined by addition of the individual perveances to obtain a total perveance,

$$P_{total} = P_p + P_r \tag{3.11}$$

which is then used to describe the cathode plasma closure velocities. Equation (3.11) is referred to as the total model. The analysis was performed using Microsoft Excel 2.2 [Mic89], and a short explanation of the speadsheet setup is given in Appendix D.

Three currents are measured and compared: 1) diode current (a measure of the total current in the diode region); 2) anode current (a measure of the current that reaches the anode); and 3) 'wall' current (the radial 'arcing' beam emissions that do not reach the anode, taken as the anode current subtracted from the diode current). The above models

magnetic field shows the slowest closure velocity at 4.2 cm/μs, the unmagnetized

condition shows 4.4 cm/μs, and the uniform magnetic field condition has the fastest

closure velocity of 5.0 cm/μs. Figure 3.11 has a summary of the closure velocities for

the planar cathode for shots M1844-M1858. The probable reason for the gradient field

showing the slowest closure velocity is the magnetic field lines (see Figure 3.12)

**Table 3.1**
Current/Model results for the three magnetic field conditions for the planar cathode.

| Magnetic Field Condition (Shot) | Closure Velocity (cm/μs) | Effective Radius (cm) |
|---|---|---|
| Diode Current and Total Model Comparison | | |
| Gradient (M1850) | 4.2 | 5.75 |
| Zero Field (M1851) | 4.4 | 7.0 |
| Uniform (M1852) | 5.0 | 4.7 |
| Anode Current and Planar Model Comparison | | |
| Gradient (M1850) | 4.2 | 6.2 |
| Zero Field (M1851) | 4.4 | 7.0 |
| Uniform (M1852) | 5.0 | 6.9 |
| Wall Current and Radial Model Comparison | | |
| Gradient (M1850) | 4.2 | 5.0 |
| Zero Field (M1851) | 4.4 | 7.0 |
| Uniform (M1852) | 5.0 | 2.75 |

impede (slow down) the radial 'edge' emissions and keep them from 'arcing' across to

the anode (or to the walls of the diode chamber) which would effectively short out the

diode. The probable reason for the uniform magnetic field showing the fastest closure is

that all the electrons emitted from the cathode surface are tied to magnetic field lines, and

the uniform field tends to have a pinching action on the electron beam. Thus the plasma

electrons tend to stream only towards the anode, resulting in a faster closure velocity.

Note that the closure velocity does not depend on the comparison of the current (diode,

anode, wall) to the model (total, planar, radial). Only the effective (cathode plasma)
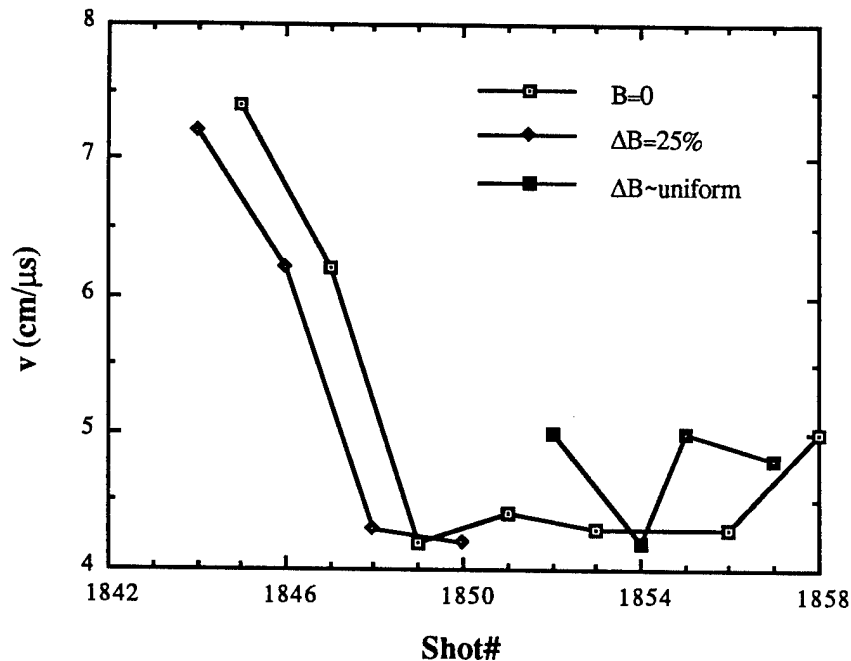
Figure 3.11. Summary of closure velocities for the planar cathode for shots M1844-M1858. The first four shots have fast closure velocities due to the conditioning of the freshly installed carbon graphite felt. Average closure velocities (not including first four shots): Gradient, 4.25 cm/μs; Uniform, 4.75 cm/μs; Unmagnetized, 4.4 cm/μs.

radius (and thus the effective cathode plasma area) depends on the model and current used. The effective radius is used to show the effects of the magnetic field conditions on the radial 'edge' effects.

The anode/planar comparison shows large values of the effective radius suggesting radial 'edge' effects are present in the planar cathode (recall that the carbon graphite felt emitting surface has only a 3.8 cm radius). Also the wall/radial comparison suggests how large an effect the radial 'edge' emission is, in that a smaller effective radius implies more delivered current from the diode to the anode (as observed experimentally). But to get a better understanding of the total effects, the diode/total model gives the best analysis. Figures 3.13, 3.14, and 3.15 show examples of the current/model comparisons for the magnetized and unmagnetized conditions for the planar cathode.

In using the diode/total model, the effects of the unmagnetized versus the magnetized conditions on the radial 'edge' effects are obvious. As expected, the zero

magnetic field condition gives the largest effective radius at 7.0 cm, matching the total radius of the cathode stalk itself. This shows that radial 'edge' effects are still a major problem when just employing the corona ring and glyptal. The uniform magnetic field condition gives the smallest effective radius of 4.7 cm, and the gradient magnetic field has a value of 5.75 cm. Both of these values are greater than the radius of the carbon graphite felt, still suggesting the existence of radial 'edge' effects, but the overall effect on the voltage pulses becomes obvious when looking at the voltage traces for the three different conditions. As Figures 3.16, 3.17, and 3.18 show, the magnetized conditions produce the longest and least degraded voltage pulses. For this reason, and for adiabatic compression, a magnetic field is applied in the diode region in the gyro-BWO experiments.
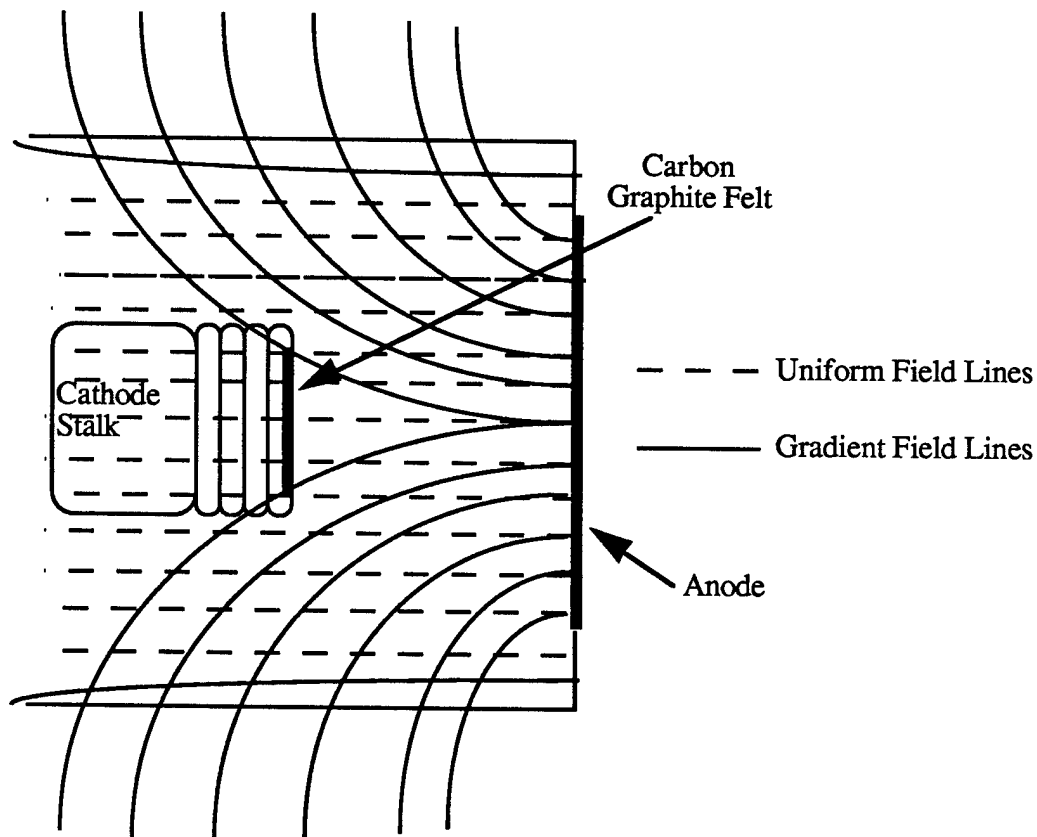


**Figure 3.12.** **Example of the magnetic field lines in the diode region for the gradient and uniform conditions.**
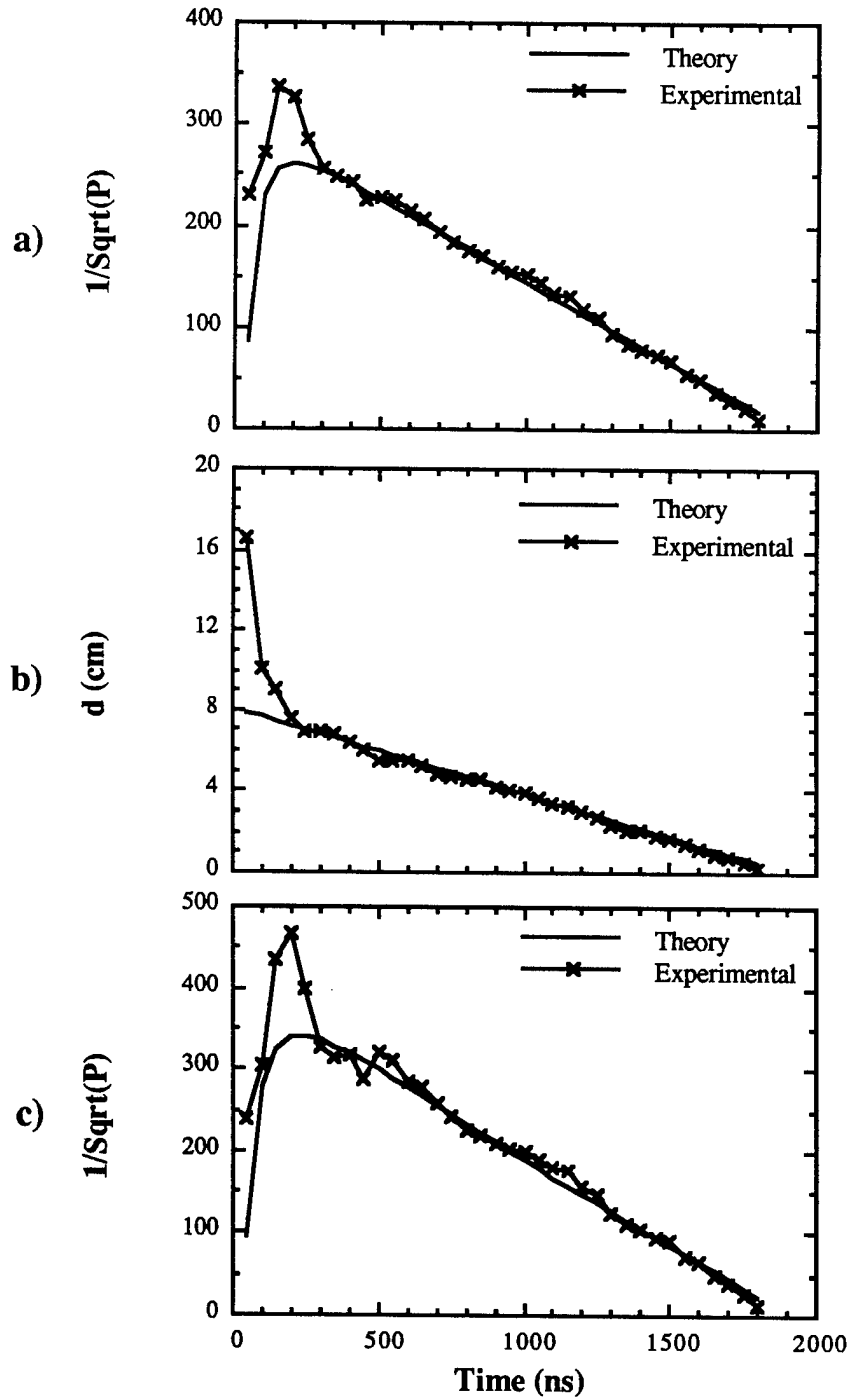
**Figure 3.13. Comparisons of the Current/Model for the gradient magnetic field condition for the planar cathode (shot M1850). a) Diode/Total model, with a closure velocity of 4.2 cm/μs and an effective radius of 5.75 cm. b) Anode/Planar model with a closure velocity of 4.2 cm/μs and an effective radius of 6.2 cm. c) Wall/Radial model with a closure velocity of 4.2 cm/μs and an effective radius of 5.0 cm.**
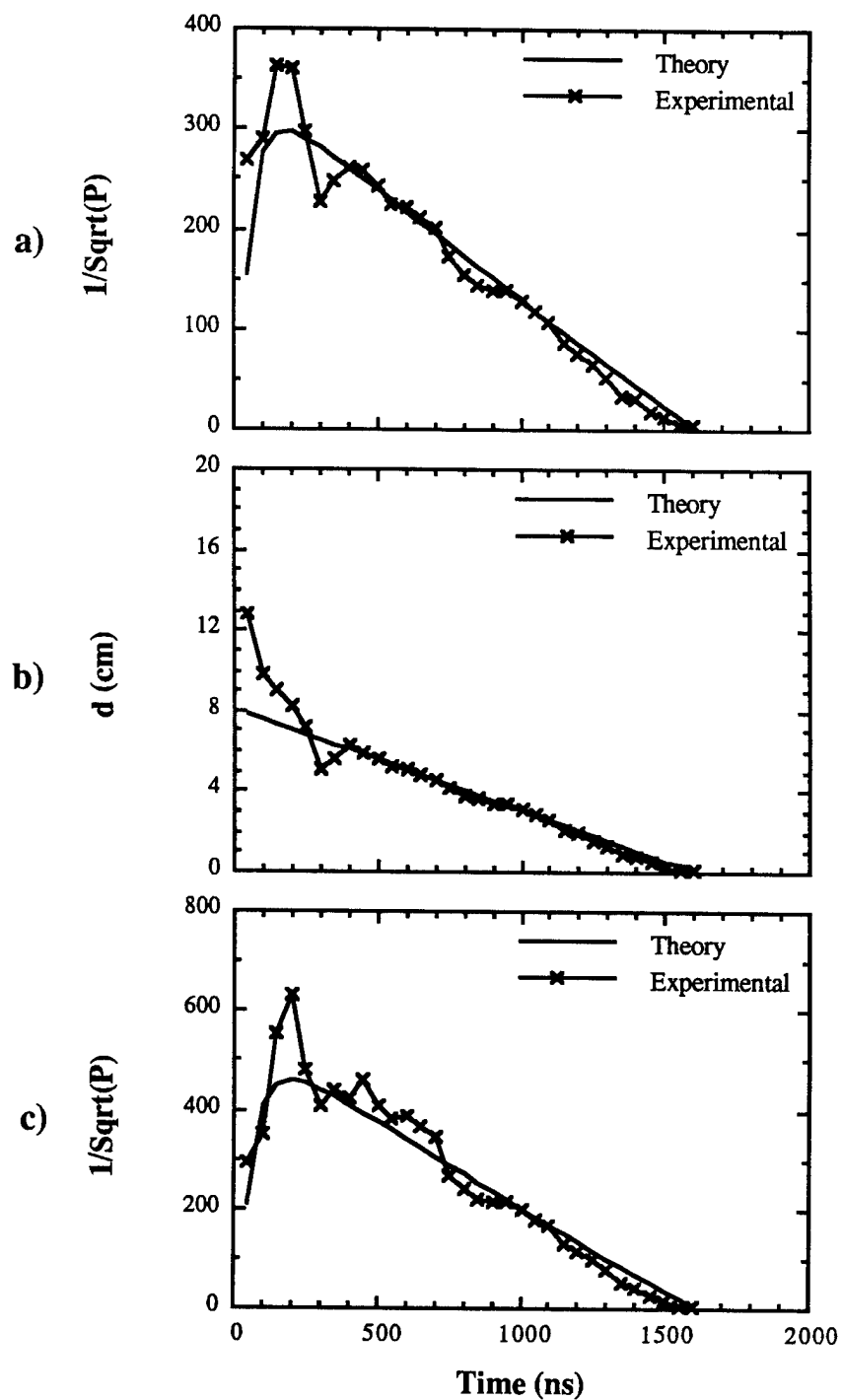
Figure 3.14. Comparisons of the Current/Model for the uniform magnetic field condition for the planar cathode (shot M1852). a) Diode/Total model, with a closure velocity of 5.0 cm/μs and an effective radius of 4.7 cm. b) Anode/Planar model with a closure velocity of 5.0 cm/μs and an effective radius of 6.9 cm. c) Wall/Radial model with a closure velocity of 5.0 cm/μs and an effective radius of 2.75 cm.
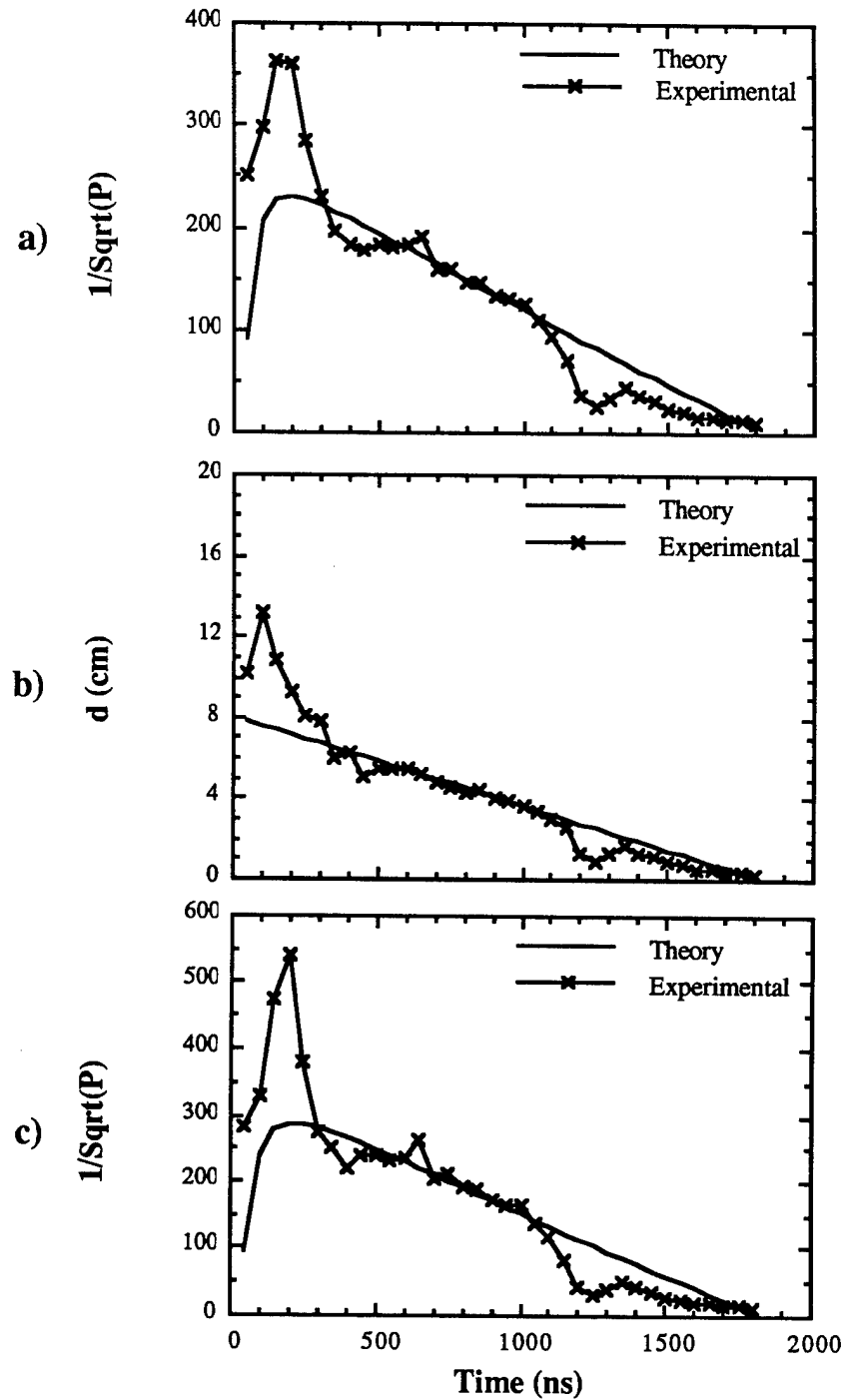
Figure 3.15. Comparisons of the Current/Model for the zero magnetic field condition for the planar cathode (shot M1851). a) Diode/Total model, with a closure velocity of 4.4 cm/$\mu$s and an effective radius of 7.0 cm. b) Anode/Planar model with a closure velocity of 4.24 cm/$\mu$s and an effective radius of 7.0 cm. c) Wall/Radial model with a closure velocity of 4.4 cm/$\mu$s and an effective radius of 7.0 cm.
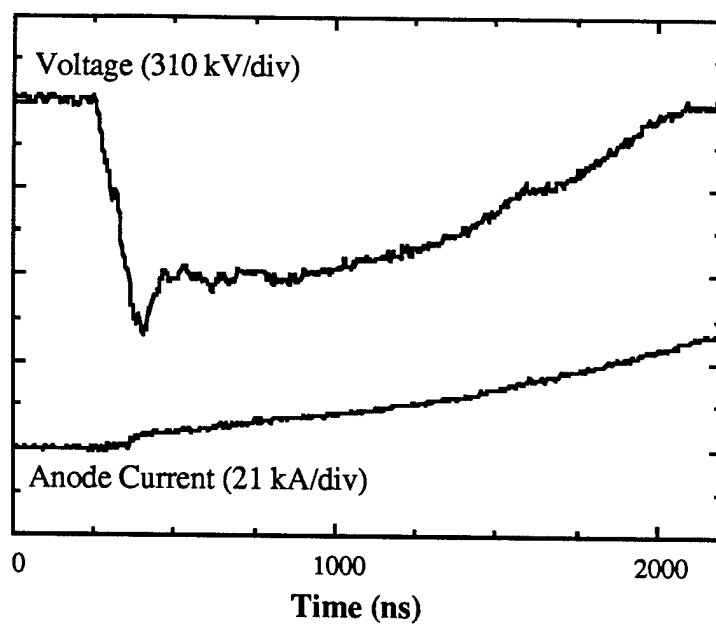
**Figure 3.16. Voltage and anode current for the gradient magnetic field condition for the planar cathode (shot M1850).**
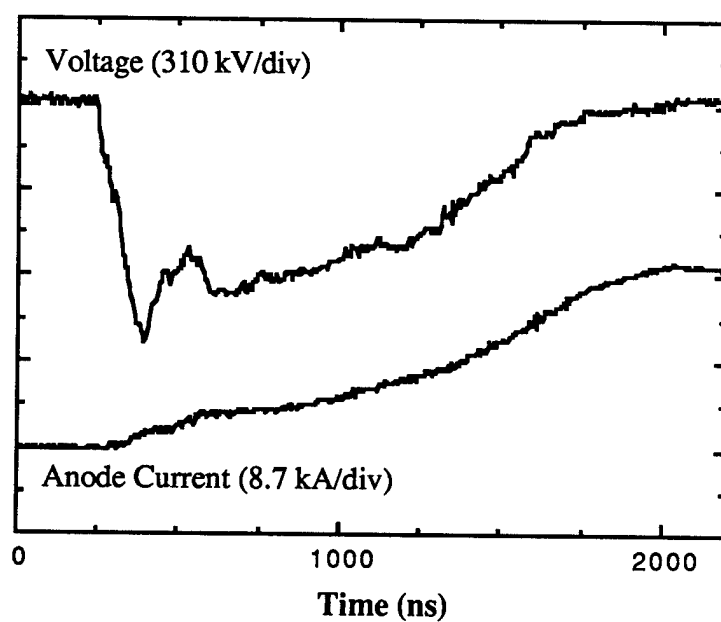


**Figure 3.17. Voltage and anode current for the uniform magnetic field condition for the planar cathode (shot M1852).**
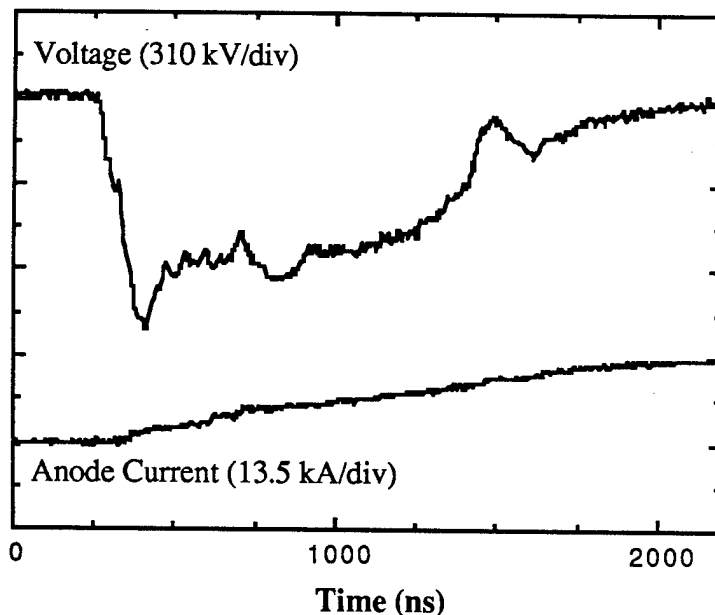
**Figure 3.18. Voltage and anode current for the zero magnetic field condition for the planar cathode (shot M1851).**

Another way to measure the effect of the radial 'edge' emissions is to show the ratio of anode to diode current. If the radial 'edge' effect is to be neglected then one expects the diode (total) current to follow the planar model as does the anode current. This would require that the ratio of anode current ($I_A$) to diode current ($I_D$) be essentially 100%. This is definitely not the case for the planar cathode as evidenced by Table 3.2, in which only the gradient field shows a ratio greater than 50%. Thus, it can also be concluded that radial 'edge' emissions are still a major factor for the planar cathode, but the magnetized conditions tend to suppress the 'arcing' tendencies in the radial direction.

**Table 3.2**
Ratio of Peak Anode to Diode currents ($I_A/I_D$) for the planar cathode for the three magnetic field conditions.

| Magnetic Field Condition (Shot) | Peak $I_A/I_D$ |
|---|---|
| Gradient (M1850) | 58 % |
| Uniform (M1852) | 44 % |
| Unmagnetized (M1851) | 30 % |

In the hopes of completely removing radial 'edge' emissions, a hemispherical-end cathode with a quasi-Chang profile attached to the end of the cathode was employed (referred to as cathode B). Using the same modeling techniques as for the planar cathode to analyze the data, the experimental results show the radial 'edge' emissions can be essentially eliminated, especially for the two magnetized conditions. Closure velocities obtained are: 2.3 cm/μs for the magnetic field gradient, 2.4 cm/μs for the uniform magnetic field (which actually has a slight magnetic field gradient of ~5 - 10 % due to the large A-K gap of 12 cm employed in the experiments), and 3 - 3.8 cm/μs for the zero magnetic field condition. Due to the large A-K gap used (~12 cm), the cathode electric field is lower than the planar cathode discussed above. This will show closure velocities slower than those of the planar cathode. Figure 3.19 shows a summary of the closure velocities for the three magnetic field conditions for cathode B. Figures 3.20, 3.21, and 3.22 show the comparison of the diode current to the total model used in obtaining the closure velocities for the three magnetic field conditions.
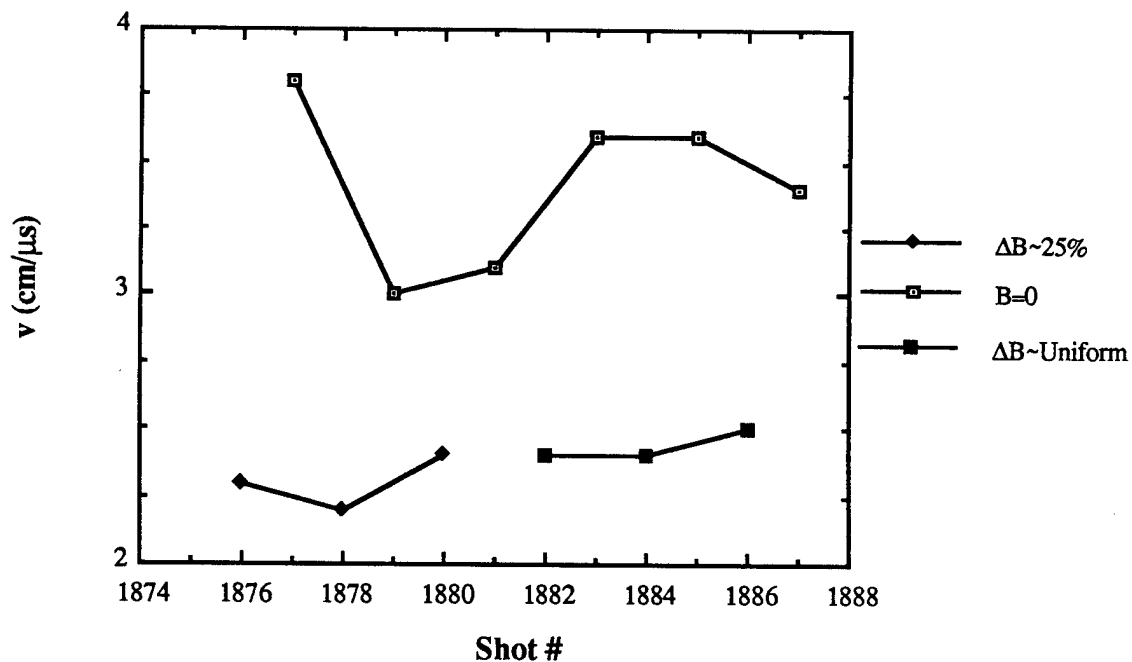


**Figure 3.19.** Summary of closure velocities for cathode B for shots M1876-M1887. Average closure velocities: Gradient, 2.3 cm/μs; Uniform, 2.4 cm/μs; Unmagnetized, 3.4 cm/μs.
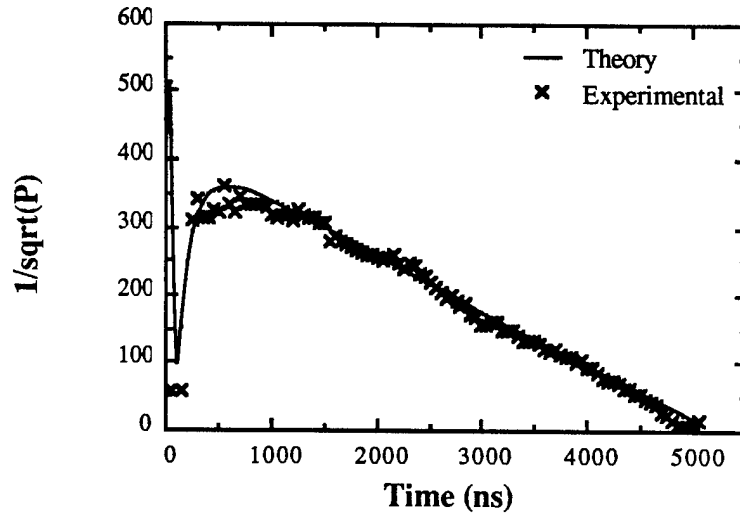
**Figure 3.20.** 1/sqrt(P) comparison of the diode current (experimentally measured) and the total model (theory) for the gradient magnetic field condition for cathode B (M1876). The closure velocity is 2.3 cm/μs, and the effective cathode plasma radius is 5.2 cm.
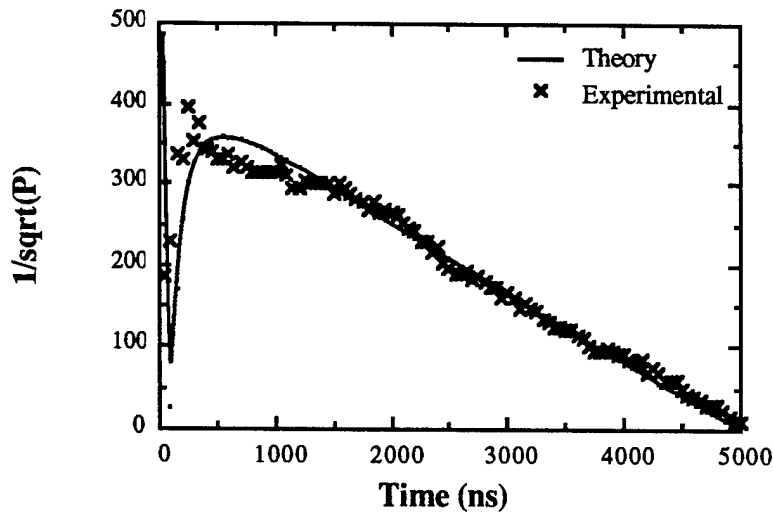


**Figure 3.21.** 1/sqrt(P) comparison of the diode current (experimentally measured) and the total model (theory) for the uniform magnetic field condition for cathode B (M1884). The closure velocity is 2.4 cm/μs, and the effective cathode plasma radius is 5.2 cm.
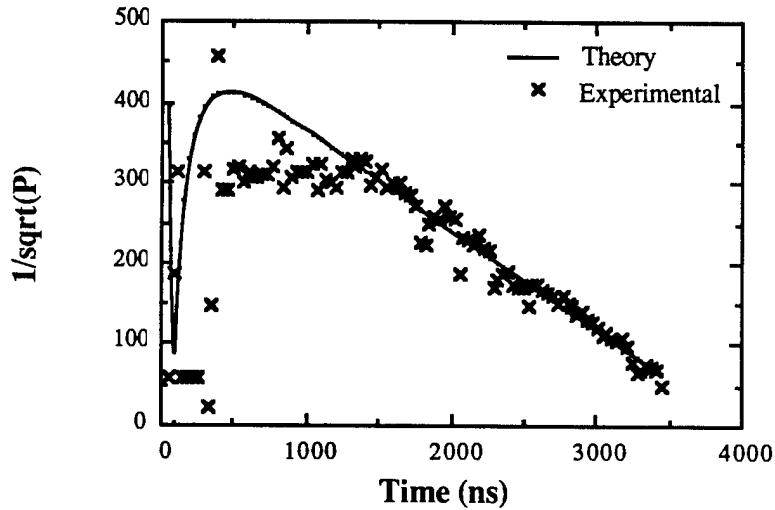
**Figure 3.22.** 1/sqrt(P) comparison of the diode current (experimentally measured) and the total model (theory) for the zero magnetic field condition for cathode B (M1875). The closure velocity is 3.0 cm/μs, and the effective cathode plasma radius is 5.3 cm.

Using the anode current to diode current ratios also shows radial 'edge' emission effects are essentially non-existent for the magnetized conditions on cathode B. Table 3.3 lists the peak as well as average ratio of $I_A/I_D$ for the data taken on the modified cathode. Note the peak 99-100% ratio for the magnetized conditions, which satisfies the criteria noted above for neglecting radial 'edge' effects. Also note that the current ratio of the unmagnetized condition for cathode B is much larger than for the planar cathode (a peak of 68% for cathode B compared to a peak of only 30 % for the planar cathode) suggesting that radial 'edge' effects are generally not as much a concern for cathode B as for the planar cathode.

**Table 3.3**

Maximum ratio of the peak anode to diode currents ($I_A/I_D$), and the average of the peak anode to diode currents obtained from shots M1876-M1887 for cathode B for the three magnetic field conditions.

| Magnetic Field Condition | Maximum Peak $I_A/I_D$ | Average $I_A/I_D$ |
|---|---|---|
| Gradient | 99 % | 85 % |
| Uniform | 100 % | 70 % |
| Unmagnetized | 68 % | 56 % |

Because of the lack of radial emission on cathode B, the voltage pulse traces also show the dramatic effect of the magnetic field on pulselengths. Smooth pulselengths of 4.5 - 5 μs are obtained for the gradient magnetic field (Figure 3.23) and for the uniform (slight gradient) magnetic field condition (Figure 3.24), as compared to the 'arcy' zero magnetic field condition whose pulselengths are only ~3-3.8 μs (Figure 3.25). Both magnetized conditions have 'flat-top' voltages of greater than 1 μs, plus well-behaved (i.e. essentially constant over 1 μs) currents of 4.5 kiloamps (and more).These smooth voltage and current pulses could be useful for generating extremely long-pulse, high power microwaves, with the possibility of large amounts of delivered energy (hypothetically a 100 MW average power, 1 μs pulse equals 100 joules). Another example of the improved electron beam results is the diode power being almost flat at 4 gigawatts for ~3 μs (Figure 3.26). This means at least ~12 kilojoules of energy are delivered to a small spot on the anode. This amount of delivered energy is evidenced by the resulting damage to the 1/8" thick graphite anode plate which was cracked and split enough as to render it unusable for future experiments. Future experiments could be conducted using the modified cathode and a thicker anode plate, for purposes of showing the effects of longer pulses and higher currents than those used in the gyro-BWO experiments presented in chapter 4.

63
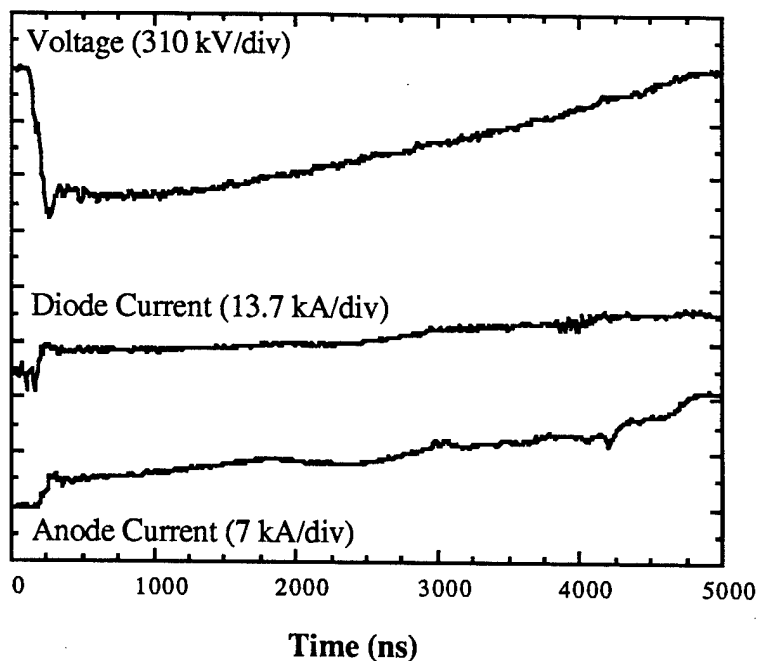


Figure 3.23. Voltage, diode current, and anode current for cathode B for the gradient magnetic field condition (shot M1876).
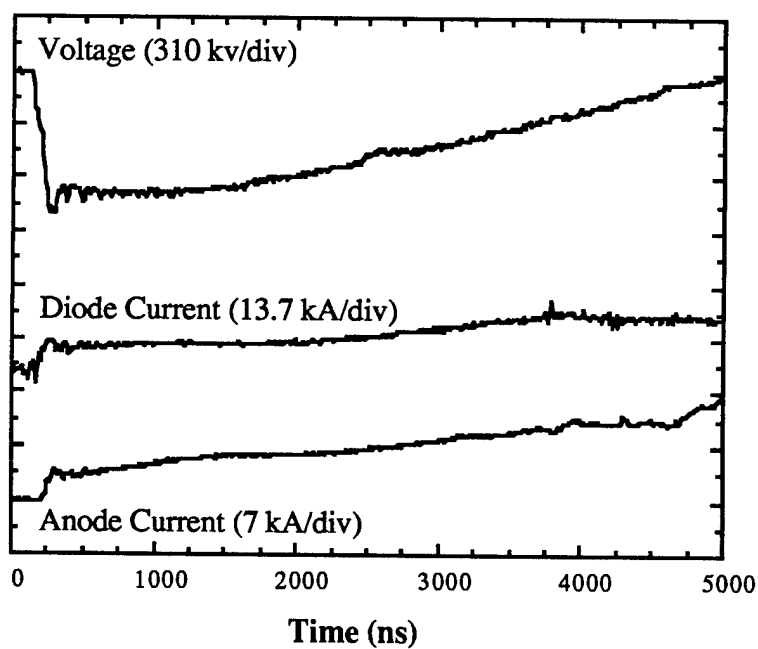


Figure 3.24. Voltage, diode current, and anode current for cathode B for the uniform (slight gradient) magnetic field condition (shot M1884).
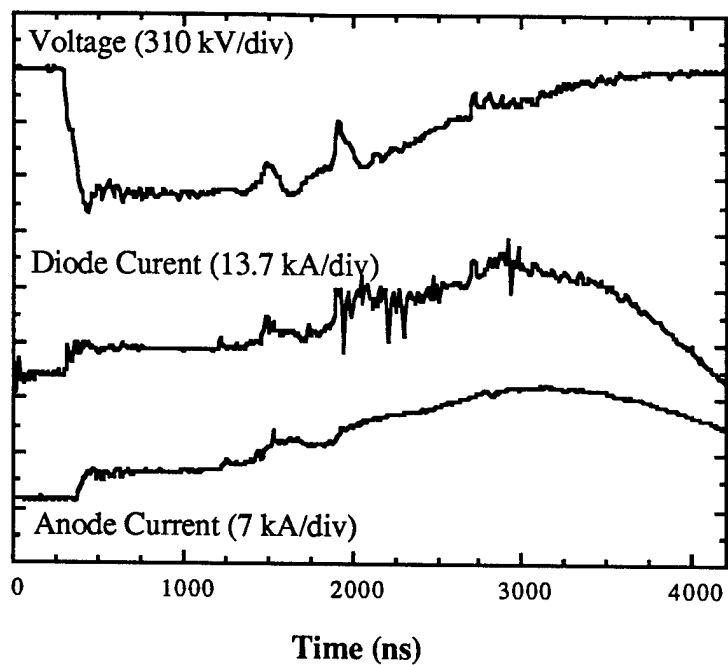
**Figure 3.25.** Voltage, diode current, and anode current for cathode B for the zero magnetic field condition (shot M1877).
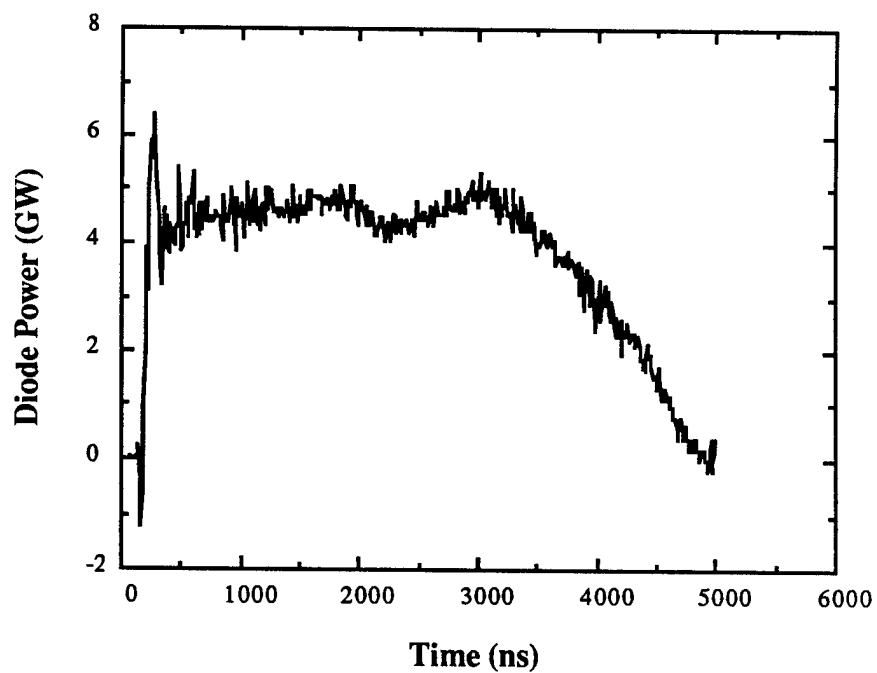


**Figure 3.26.** Diode power as a function of time (shot M1876).

## 3.4 Interaction Cavities

The interaction cavities are designed to take full advantage of the uniform axial magnetic field provided by the maser solenoid. The uniform magnetic field region is about 50.5 cm long, thus the cavity is chosen to be of this length. The theoretical optimum cavity length can be calculated by combining single particle theory and the guide wavelengths of the cavity to first obtain the optimum number of cyclotron orbits [Bra81],

$$N_{opt} \approx \frac{2}{\beta_{\perp 0}^2} \left( \frac{\left(1 - \frac{\beta_{z0}}{\beta_{ph}}\right)^2}{\left(1 - \beta_{ph}^{-2}\right)} \right) \tag{3.12}$$

where $\beta_{\perp 0}$ is the initial perpendicular $\beta$, $\beta_{z0}$ is the initial axial $\beta$, and $\beta_{ph}$ is the phase $\beta$ of the wave in the cavity. Using a beam energy of 700 kV, an $\alpha$ of 0.6 and a frequency of 4.57 GHz (slightly above the vacuum cutoff frequency of 4.55 GHz) gives an $N_{opt}$ of about 8. For the gyrotron, the optimum length is given by [Bra81],

$$L_{opt} \approx \frac{c\beta_{z0}N_{opt}}{f} \tag{3.13}$$

where c is the speed of light and f is the frequency of operation. Using the above numbers gives an optimum length of ~ 41 cm. Again this is valid for single particle theory, thus one would expect the actual length of optimization to be longer and the choice of 50.5 cm is considered a reasonable length.

The cavity radius is ~ 1.93 cm, which gives a $TE_{11}$ (lowest mode) vacuum frequency cutoff of 4.55 GHz (using equation A.41). Table 3.4 lists the cutoff frequencies for the most important cavity modes.

Other smooth cavities used were: 1) radius of 1.93 cm and length of ~ 58.5 cm, and 2) radius of 1.64 cm and length of ~ 58.5 cm (both in a different maser solenoidal field which was uniform over a longer distance).

Other experiments were conducted using a Bragg resonator on both the input and output ends of a smooth tube cavity (of length ~28 cm) [Cho91]. The Bragg resonators are used to increase the reflectivity of a given frequency (in this case the $TE_{31}$ mode at

**Table 3.4**

Vacuum cutoff frequencies of different modes for a cavity radius of 1.93 cm.

| Mode | Cutoff Freq. | Mode | Cutoff Freq. | Mode | Cutoff Freq. |
|------|-------------|------|-------------|------|-------------|
| $TE_{11}$ | 4.55 GHz | $TE_{12}$ | 13.2 GHz | $TM_{01}$ | 5.95 GHz |
| $TE_{21}$ | 7.55 GHz | $TE_{51}$ | 15.9 GHz | $TM_{11}$ | 9.47 GHz |
| $TE_{01}$ | 9.47 GHz | $TE_{22}$ | 16.6 GHz | $TM_{21}$ | 12.7 GHz |
| $TE_{31}$ | 10.4 GHz | $TE_{02}$ | 17.3 GHz | $TM_{02}$ | 13.6 GHz |
| $TE_{41}$ | 13.1 GHz | $TE_{61}$ | 18.5 GHz | | |

18.9 GHz), but the reflectivity of the whole frequency spectrum is also increased, if the ripples protrude into the tube. The parameters of the Bragg resonators are: input end: period = 0.95 cm, length = 14.25 cm, corrugation amplitude = ± 0.16 cm, average radius = 1.93 cm, Q (for $TE_{31}$) = 4700. A more detailed description of the Bragg resonators appears elsewhere [Cho91].

## 3.5 Diagnostics

To perform detailed analysis of the microwaves generated in the gyro-BWO experiments, many diagnostics must be employed. The voltages, currents, beam velocity ratio ($\alpha$), and magnetic fields at which the interactions occur as well as the microwave signals themselves must be measured and recorded. This section details the diagnostics used in the gyro-BWO experiments.

### 3.5.1 Electron Beam Diagnostics

A copper sulphate solution resistive divider is used to monitor the MELBA cathode voltage, and a B-dot loop detects the azimuthal magnetic field induced by the e-beam current flow on-axis in the diode region [Mil89]. A Rogowski coil is used to measure the injected current into the initial drift tube leading to the interaction cavity.

A Cerenkov plate diagnostic [Cho91] mentioned above is used for the measurement of the axial velocity and axial energy spreads.

## 3.5.2 Microwave Measurements

Two microwave detection configurations were used in the experiments. For the Bragg resonator cases and the longer smooth cavity interaction tubes, an open ended, rectangular S-band horn antenna placed in the forward direction is used to detect the low frequency emission from the cyclotron resonance maser experiments. The open ended S-band antenna is set inside a large chamber filled with microwave absorber (Eccosorb type AN-74) to reduce reflections of the microwaves inside the chamber (see Figure 3.27). The antenna is also positioned in the far-field region (72 cm from the output window), and is placed on-axis since this is where the peak power of the $TE_{11}$ mode exists (see Figure 3.28). Of course, there exists the question as to the polarization and orientation of the electric field exiting the output window, but a conservative estimate of the power can be arrived at if the rf measured is considered to be at its maximum field orientation. The S-band open-ended antenna was found to detect approximately -11.5 dB of the microwave power exiting the output window. Once the rf is picked up by the S-band antenna, the signal travels through an S-band waveguide system to a Faraday cage,



S-Band Open-Ended Horn

Microwave Absorber (Eccosorb Type AN-74)
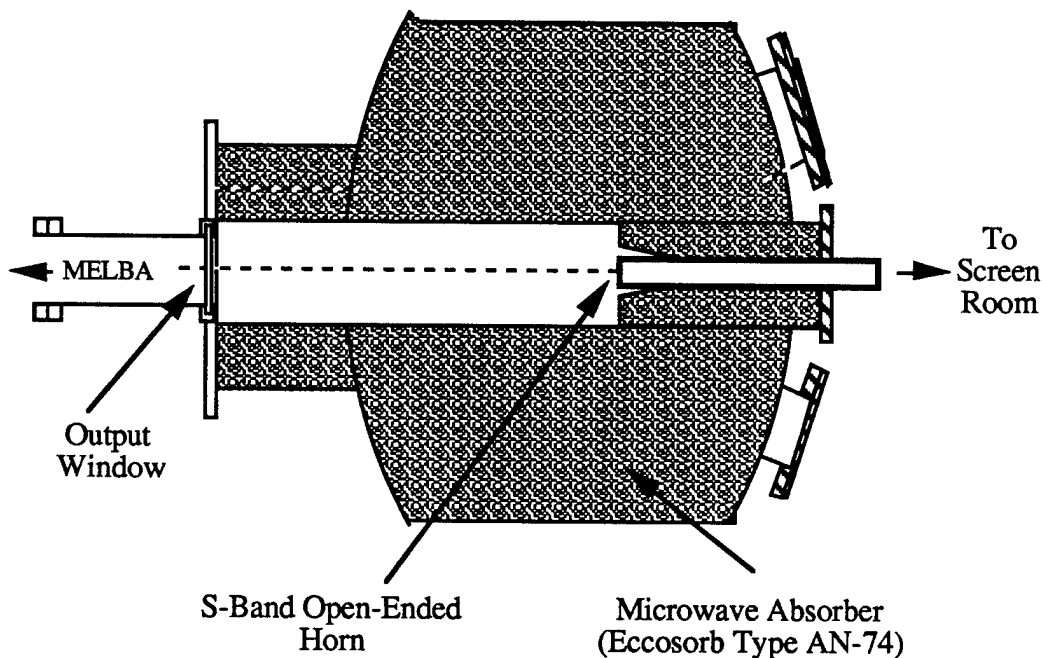
**Figure 3.27.** S-Band Open-Ended horn antenna position in relation to the output window (positioned ~72 cm from the output window).
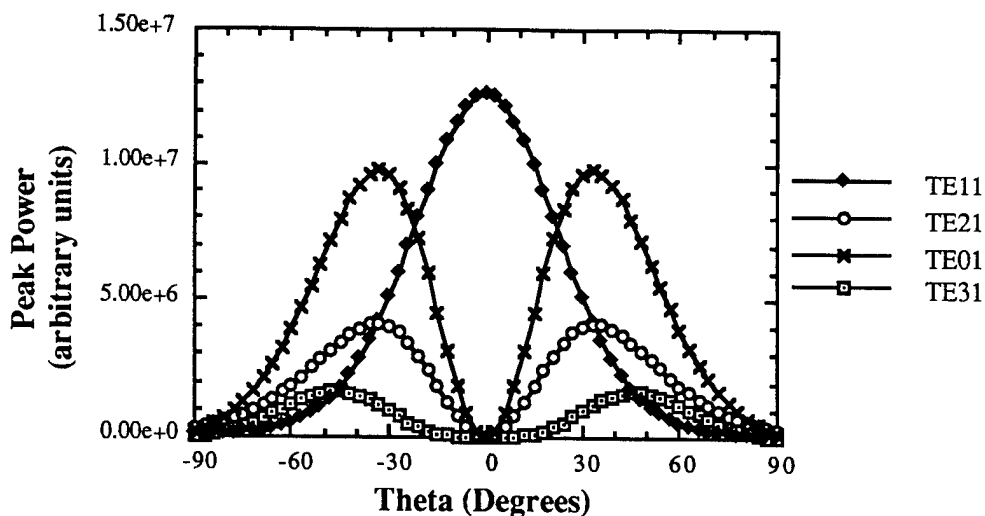
**Figure 3.28.** A two-dimensional (phi = 0°) peak power plot for different modes as a function of theta. Zero degrees corresponds to the on-axis position.

where it is further attenuated by directional couplers and coaxial attenuators, detected by calibrated crystal diode detectors, and then displayed on an oscilloscope. An example of the Hewlett Packard (model 8472B) diode detector calibration curve is shown in Figure 3.29.

The second microwave detection configuration is one in which a Vlasov-type, rectangular S-band antenna is employed to detect rf at the backward (diode) end of the beam tube. The Vlasov-type antenna is designed to detect the low frequency skip angles
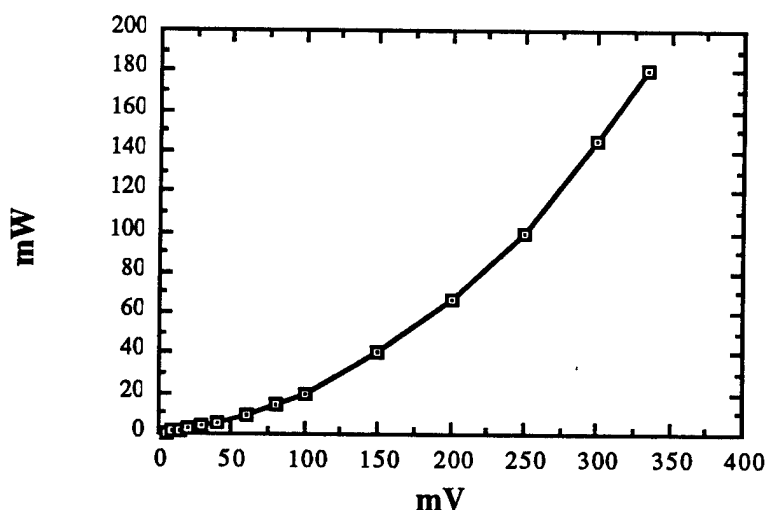


**Figure 3.29.** Calibration curve for an HP8472B diode detector at 7.5 GHz (labeled as #71 among the diode detectors used in the experiments).

present for the $TE_{11}$ backward wave mode. The skip angle for a given frequency is determined by [Ram65],

$$\theta = \cos^{-1}\left(\frac{f_c}{f}\right) \tag{3.14}$$

Table 3.5 gives skip angles as a function of frequency for the $TE_{11}$ mode. Figure 3.30 shows the skip angle relative to the narrow cavity walls. Note that for the experiments the waveguide was cut at an angle of 30 degrees relative to the broad wall. This is the opposite of a conventional Vlasov antenna which is cut at the skip angle relative to the narrow wall. The tip of the antenna is placed ~ 1.5 cm into the drift tube, so as not to

**Table 3.5**
Skip angles as a function of frequency for the $TE_{11}$ cavity mode.

| Frequency (GHz) | Skip Angle (degrees) | Frequency (GHz) | Skip Angle (degrees) | Frequency (GHz) | Skip Angle (degrees) |
|---|---|---|---|---|---|
| 4.57 | 5.14 | 4.75 | 16.6 | 5.05 | 25.7 |
| 4.60 | 8.33 | 4.85 | 20.2 | 5.15 | 27.9 |
| 4.65 | 11.8 | 4.95 | 23.1 | 5.25 | 29.9 |

interfere with the propagation of the electron beam to the interaction cavity. A Hall effect magnetic axial probe (the same as the one used for the diode field measurement) is used to measure the diode magnetic field perturbation of the antenna and accompaning S-band waveguide, and the perturbation is found to be negligible.
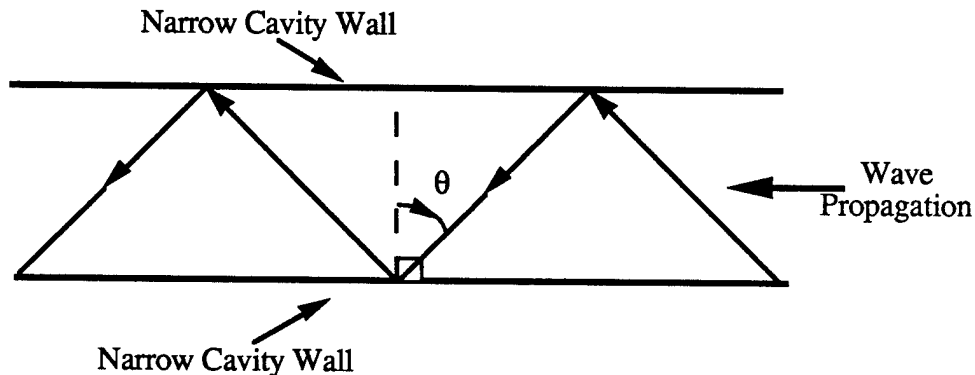


**Figure 3.30. Skip angle ($\theta$) of a wave propagating between cavity walls.**

The experimental setup depicted in Figure 3.31 is used to measure the efficiency of the Vlasov antenna. A Polarad microwave signal generator is employed to generate a cw microwave signal at 5.0 GHz. The generated signal is then split by a 6 dB power divider, one part of the signal traveling to a calibrated diode detector (Hewlett Packard 8472B) which is displayed on an oscilloscope (Tek 465B). The other part of the signal
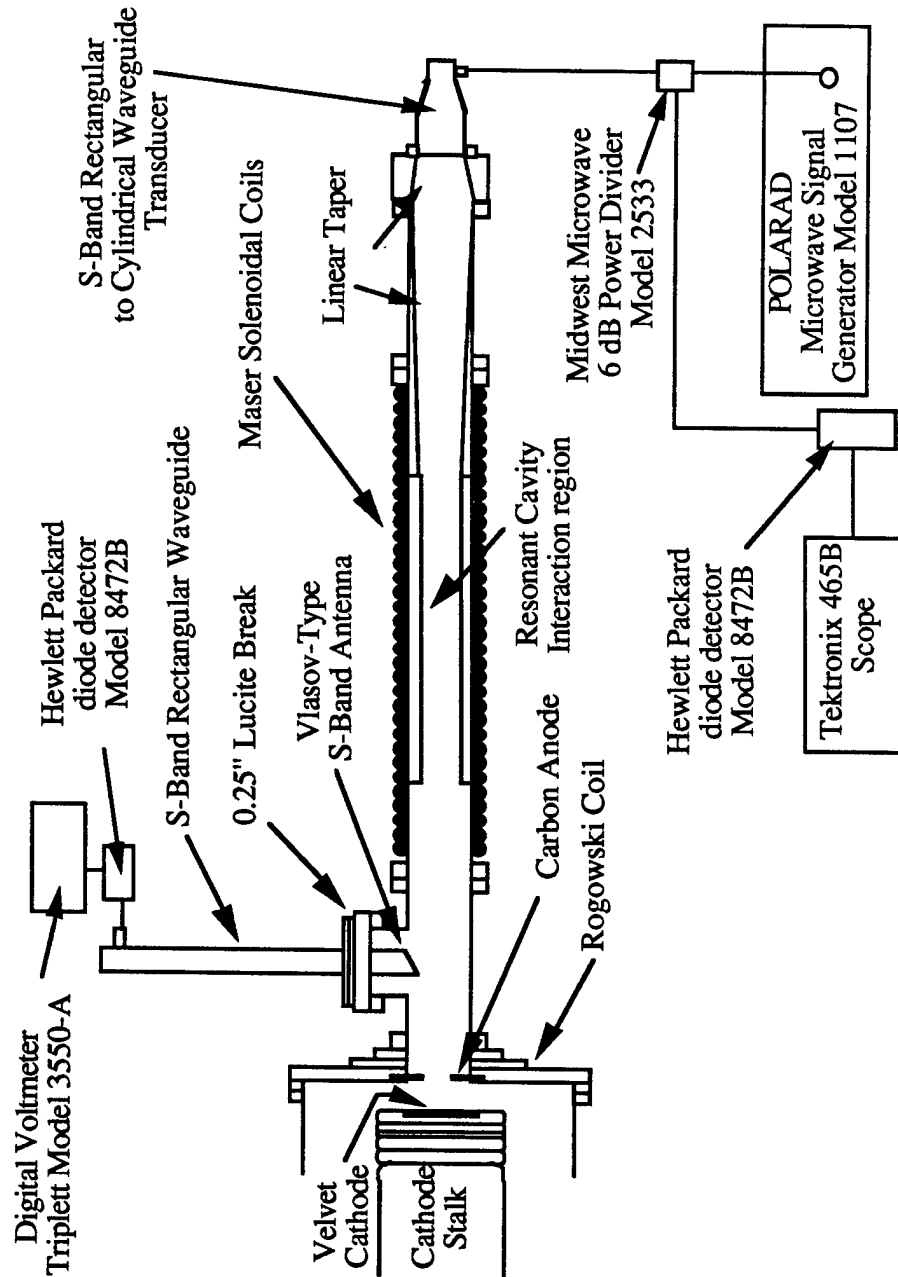


**Figure 3.31.  S-Band Vlasov-type antenna calibration configuration.**

travels to an S-Band rectangular to cylindrical (radius = 3.81 cm) waveguide transducer, followed by a linear taper down to the resonant cavity, and the signal is then received by the Vlasov antenna. The Vlasov-received signal passes through a short section of S-Band waveguide, and is detected by a calibrated diode detector (Hewlett Packard 8472B), and displayed on a digital voltmeter (Triplett Model 3550-A). After calibrating the coaxial cables, the Vlasov antenna was found to detect approximately -14 dB of the generated signal at 5.0 GHz.

After being detected by the antenna, the signal propagates through a 1/4 inch thick lucite window (attached with nylon bolts) to provide ground isolation of the waveguide that reaches the Faraday cage from that of MELBA ground. This is done in case the e-beam strikes the antenna, which, without the isolation, could cause large currents on the waveguide. After the lucite window, the signal continues through two 30 dB S-band waveguide directional couplers ( one of which is terminated with a matched high power dummy load) before entering the Faraday cage. After entering the cage, the microwave signal undergoes further attenuation by both waveguide directional couplers and coaxial attenuators. The signal is split between three channels, one that measures the full S-band signal, one that has a 6.0 GHz low-pass filter, and one that has a cylindrical cavity frequency filter with a resonance at 5.16 GHz. Each of these signals is detected by a calibrated diode detector and measured on an oscilloscope.

The calibration of the S-band waveguide is shown in Appendix F. Notice that since frequencies greater than 4.55 GHz have a large uncertainty as to the attenuation (with a minimum of 20 dB for the two 30 dB (60 dB total) S-Band waveguide directional couplers connected in series, a minimum of 6 dB for the 20 dB S-Band waveguide directional coupler, and a minimum of 12 dB for the 30 dB S-Band waveguide directional coupler; see Figures F.1 - F.5), only conservative estimates of power using the lowest attenuation could be obtained for the results obtained from the 1.93 cm radius interaction cavity.

72
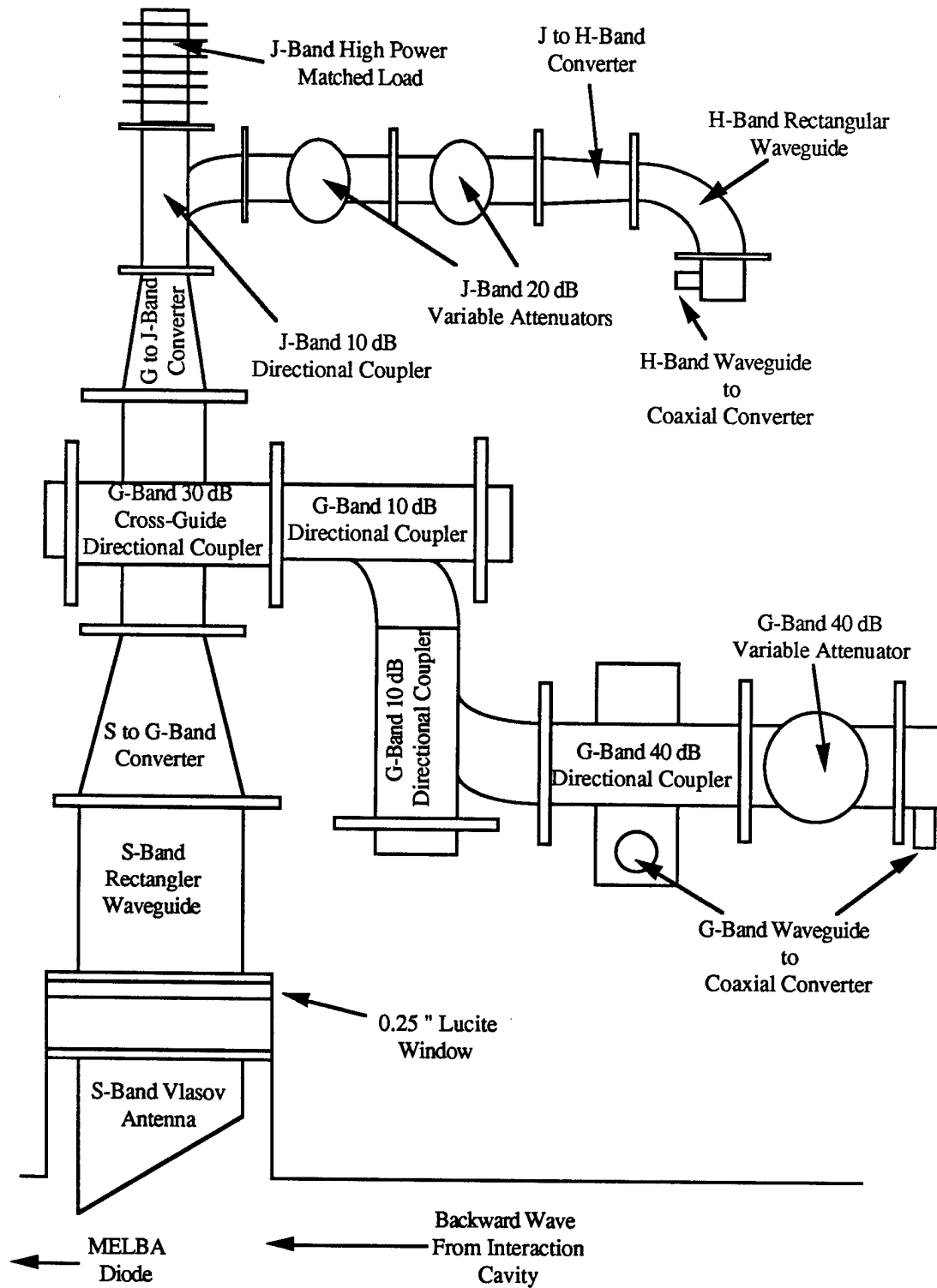


**Figure 3.32.  The waveguide detection system configuration.**

In order to obtain better power calibration and frequency measurements, another waveguide system is employed for which the generated signals are in the fundamental $TE_{10}$ mode band. This waveguide system is depicted in Figure 3.32. Table 3.6 lists the cutoff frequency and recommended $TE_{10}$ frequency range of operation for the various types of waveguide. The signal is again detected by the Vlasov-type S-Band antenna, and travels through a short section of S-Band rectangular waveguide (with a cutoff frequency of $f_{co}$ = 2.08 GHz). Next it passes through an S- to G-Band ($f_{co}$ = 3.15 GHz) waveguide convertor where the signal is then divided between two waveguide channels. One waveguide channel consists of a 30 dB G-Band ($f_{co}$ = 3.15 GHz) directional coupler, and two 10 dB G-Band ($f_{co}$ = 3.15 GHz) directional couplers. The microwave signal is then detected in two locations, the first through a 40 dB G-Band ($f_{co}$ = 3.15 GHz) directional coupler with a waveguide to coaxial convertor, coaxial attenuators, and a diode detector. This detector location acts as a high pass filter, measuring all frequencies greater than 3.15 GHz. The second detector signal (still in the first waveguide channel) consists of a 40 dB G-Band ($f_{co}$ = 3.15 GHz) variable attenuator, a waveguide to coaxial convertor, coaxial attenuators, a 6 GHz low pass filter, and a diode detector to give a detectable frequency range of 3.15 - 6 GHz.

The second waveguide channel consists of a G- to J-Band ($f_{co}$ = 4.30 GHz) waveguide convertor, and a 10 dB J-Band directional coupler. The original microwave signal detected by the Vlasov-type antenna is dissipated in a high power matched J-Band ($f_{co}$ = 4.30 GHz) load. The microwave signal directed through the 10 dB J-Band directional coupler continues through two 20 dB J-Band ($f_{co}$ = 4.30 GHz) variable attenuators. Initially, the second waveguide channel had a J-Band waveguide to coaxial convertor, coaxial attenuators, an 8 (or 10) GHz low pass filter and a diode detector to give a measurable frequency range of 4.3 - 8 (or 10 ) GHz. This J-Band detection system was used to compare with the G-Band (3.15 - 6 GHz) signal (discussed in Chapter 4). After using the J-Band waveguide to coaxial convertor for the comparison, it

was replaced by a J- to H-Band ($f_{co}$ = 5.27 GHz) waveguide convertor, a short section

of H-Band rectangular waveguide, a waveguide to coaxial convertor, coaxial attenuators,

an 8 GHz low pass filter, and a diode detector to give a detectable frequency range of

5.27 - 8 GHz.

**Table 3.6**

Some characteristics of the waveguide bands used in the detection system of the
experiment [Saa73].

| Band | $TE_{10}$ Freq. Cutoff (GHz) | $TE_{10}$ Recommended Freq. Range (GHz) | Pulsed Microwave Air Breakdown (MW) |
|------|------|------|------|
| S | 2.08 | 2.60 - 3.95 | 10 -12 |
| G | 3.15 | 3.94 - 5.99 | 4 - 6 |
| J | 4.30 | 5.38 - 8.17 | 2 - 3 |
| H | 5.27 | 6.57 - 9.99 | 0.8 - 1 |

### 3.5.3 Frequency Filters

A series of cylindrical cavity filters are used in order to get a better measurement

of the frequency. The cavity filter is designed to have a dominant resonant frequency in

the $TM_{010}$ mode, by using a loop antenna at both the input and output ends of the filter

and keeping the ratio of the height to the radius greater than 2 [Har61].The cavity filters

used have an approximate radius of 2.2 cm, and a height of approximately 1 cm. The

cavity resonant frequency (in GHz) for the TM modes is given by (see, for example,

[Har61])

$$f_{mnp} = 4.775 \sqrt{\frac{x_{mn}^2}{r^2} + \frac{\pi^2 p^2}{h^2}}$$
(3.14)

where m = 0,1,2... is the azimuthal variation number, n = 1,2,3... is the radial varition

number, p = 0,1,2... is the axial variation number, $x_{mn}$ are the zeros of the Bessel

functions $J(x_{mn})$ = 0, r is the radius of the cavity, and h is the height of the cavity. In

order to tune the filter to the desired frequency, a tuning screw is employed. The tuning

screw enables the frequency to be adjusted by changing the effective capacitance and inductance of the cavity filter. Epoxy holds the tuning screw in place after the resonant frequency has been adjusted. An HP8510 network analyzer is used to calibrate the cavity frequency filters. Figure 3.33 shows the cylindrical cavity frequency filter. An example of the frequency spectrum of the cavity filters is shown in Figure 3.34. Table 3.7 lists the characteristics of the frequency filters employed in the experiment. One must note that other higher order resonant frequency modes also exist in the cavity filters as evidenced in Figure 3.35. Low pass filters are employed to avoid the detection of these higher resonant frequencies.



**Side View**      **Top View**
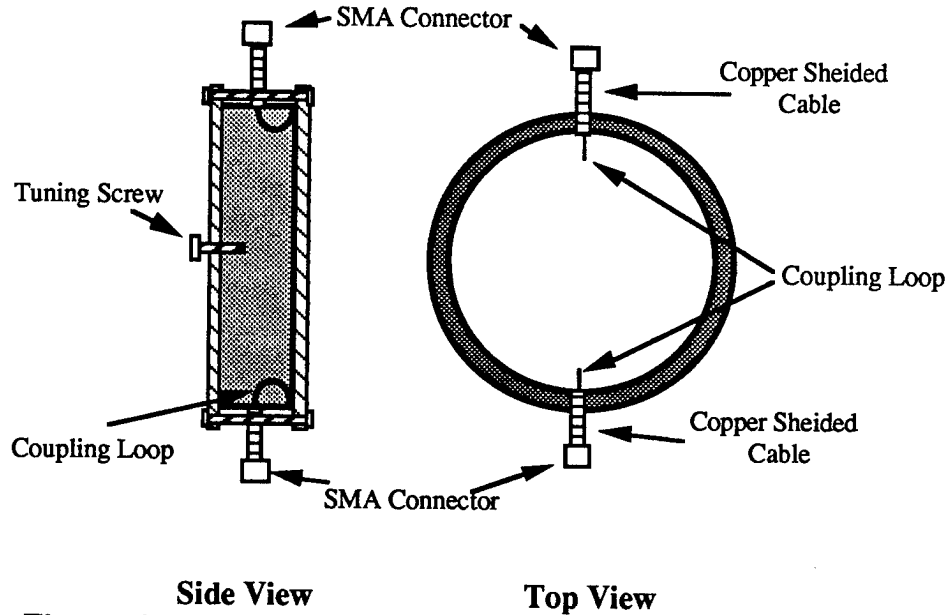
**Figure 3.33. The cylindrical cavity frequency filter design.**

**Table 3.7**
Characteristics of the cylindrical cavity filters used in the experiment.

| Filter # | $TM_{011}$ Resonant Frequency (GHz) | 10 dB Freq. Width (GHz) | Insertion Loss (dB) |
|---|---|---|---|
| G1 | 4.67 ± 0.05 | 4.64 - 4.71 | ~ 3.3 |
| G2 | 4.72 ± 0.05 | 4.64 - 4.82 | ~ 7.8 |
| G3 | 5.12 ± 0.05 | 4.92 - 5.26 | ~ 15.5 |
| H1 | 5.38 ± 0.05 | 5.24 - 5.60 | ~ 13.0 |
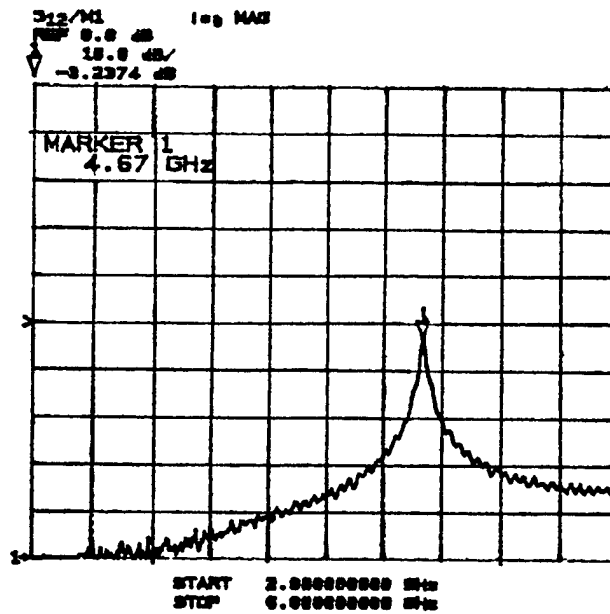
Figure 3.34.  The resonant frequency spectrum for the G1 cylindrical
cavity frequency filter.
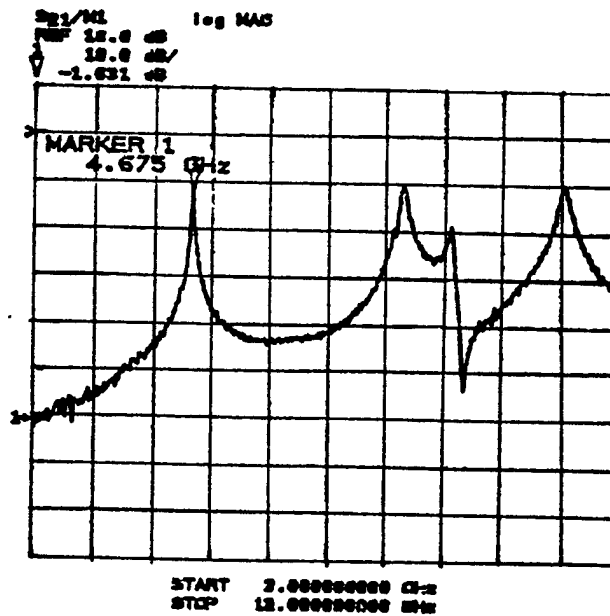


Figure 3.35.  The resonant frequency spectrum for the G1 cylindrical
cavity frequency filter showing the higher order mode resonant peaks.

### 3.5.4 Energy Diagnostic

A calorimeter in the form of a pyramid shaped thin graphite horn (see Figure 3.1) is employed for energy measurements. The calorimeter and its circuitry were designed by Jin Choi are described elsewhere [Cho91]. The calorimeter is placed 90 degrees off-axis (again, see Figure 3.1) in order to remove the possibility of the calorimeter detecting diode light or being struck by the electron beam (which was suspected when the calorimeter was initially placed in the position occupied by the output window). A copper guiding screen is used to direct the microwaves onto the calorimeter. The calorimeter signal travels to the Faraday cage, shielded by copper pipe, to a balanced circuitry system that has been calibrated at ~70 mV/Joule. The signal is displayed on a slow digitizing scope (TEK 5335), due to the fact that it takes several seconds for the calorimeter to reach thermal equilibrium. An advantage to this long time scale is that the noise generated by the accelerator and electron beam (on the order of microseconds) is gone long before the calorimeter reaches thermal equilibrium and does not affect the final calorimeter signal displayed on the scope.

# CHAPTER IV

# EXPERIMENTAL RESULTS

### 4.1. Solid Beam Results

Figure 4.1 shows the peak cyclotron maser power detected in the waveguide system as a function of the magnetic field for the 5.1 cm diameter anode aperture. This gives the general scaling of the power versus the magnetic field. Figure 4.2 shows the same peak power, but as a function of $F_c/\gamma$ instead of the magnetic field. This is done since the voltage is not a constant, which causes a variation in the interactions from shot to shot, even though the magnetic field may be the same for different shots. The peak extracted power ranges from ~300 - 800 kW, with an average of ~ 450 kW, at a magnetic field of 4.7 - 6.6 kG. Since the antenna picks up approximately 10% of the microwave signal, this would imply a tube power estimate of 3 - 8 MW, which would be ~ 1 - 2% efficient. Similar power estimates were obtained from the calorimeter, but the calorimeter measures all the power (including the power of any forward waves) since the calorimeter was located at the downstream (away from the diode end) end of the experiment (see Figure 3.1). There was some correspondence between the diode detector results and calorimeter results in that typically both increased or decreased for the same particular data shot enabling one to use the calorimeter as a rough comparison to the diode detector results for the gyro-BWO output power. The maximum extracted power was obtained at $F_c/\gamma$ ~ 6.2 GHz. Notice that the power is greatly reduced at the vacuum frequency cavity cutoff of 4.55 GHz. Three possible explanations exist, which are: 1) the power is 'trapped' inside the interaction cavity, that is, the skip angle approaches zero degrees near cutoff causing an inability for the wave to escape the interaction cavity; 2) due to the large

78

spread in $\alpha$, the interaction could exist on the right hand side of the dispersion curve implying a forward wave; or 3) due to the large amount of current in the interaction cavity (~1 - 2 kA), the cutoff frequency undergoes a frequency upshift. This can be shown by starting with the effective plasma frequency of the beam,

$$\omega_{pe}^2 = \left( \frac{N_0 e^2 \mu_0 c^2 A_b}{m_0 \pi r_c^2} \right)$$ (4.1)

where $N_0$ is the number density of the beam, e is the electron charge, $\mu_0$ is the magnetic permeability, $A_b$ is the cross-sectional area of the beam, $m_0$ is the mass of the electron, and $r_c$ is the cavity radius. Knowing the number density,

$$N_0 = \frac{I_b \pi r_c^2}{A_b \pi r_c^2 e v_{z0}}$$ (4.2)

where $v_{z0}$ is the electron velocity in the z-direction, one can substitute equation (4.2) into equation (4.1),and after some algebraic manipulation, obtain,

$$\omega_{pe}^2 = I_b \left( \frac{e}{c \varepsilon_0 m_0 \pi r_c^2} \right) \sqrt{\frac{1 + \alpha^2}{\gamma_0^2 - 1}}$$ (4.3)

where $\varepsilon_0$ is the vacuum permitivity, $\alpha$ is the ratio of $v_\perp/v_\parallel$, and $\gamma_0$ is the initial relativistic Lorentz factor. Using the dispersion equation for a waveguide uniformly filled with plasma,

$$\omega^2 = \frac{(k_{mn}^2 + k_z^2)}{\mu \varepsilon}$$ (4.4)

along with the dielectric constant of a cold, homogeneous, isotropic plasma,

$$\varepsilon = \varepsilon_0 \left( 1 - \frac{\omega_{pe}^2}{\omega^2} \right)$$ (4.5)

leads to the e-beam filled cavity cutoff frequency,

$$f_{eco} = f_{co} \sqrt{1 + \frac{f_{pe}^2}{f_{co}^2}}$$ (4.6)
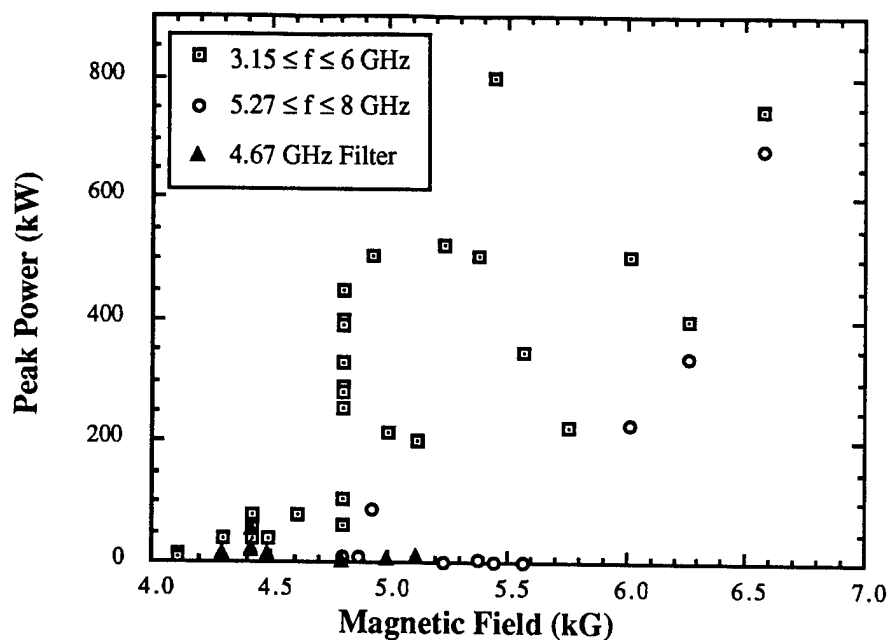
**Figure 4.1.** **Peak power measured in the waveguide detection system as a function of the magnetic field for the solid beam.**
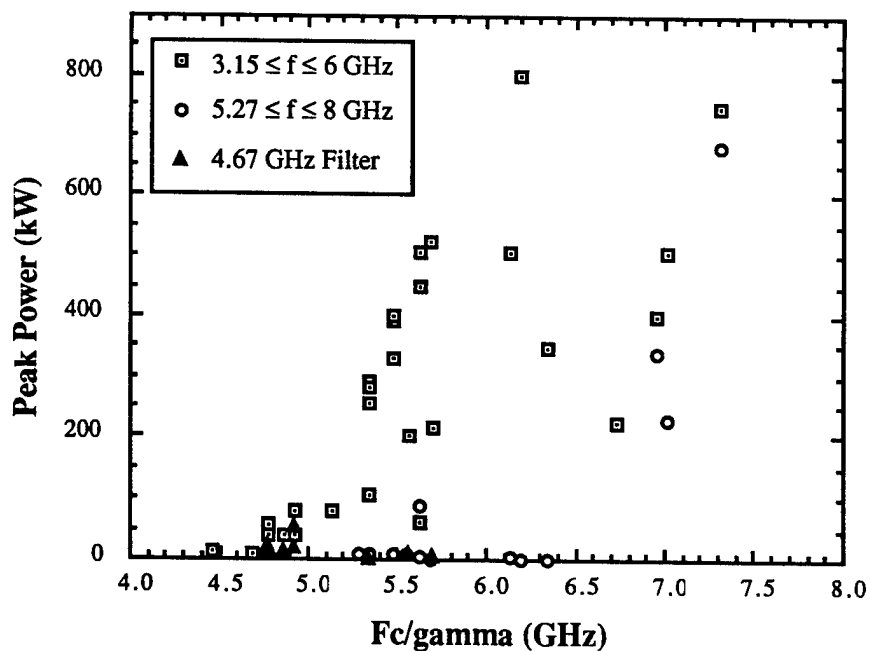


**Figure 4.2.** **Peak power measured in the waveguide detection system as a function of $F_c/\gamma$ for the solid beam.**

where $f_{co}$ is the vacuum cavity cutoff frequency (see Appendix A), and $f_{pe}$ is the effective

plasma frequency.

Using a beam current of 1 kA, a beam energy of 750 kV, and an $\alpha$ of 0.65, the

cutoff frequency upshifts to ~4.75 GHz. Thus the power detected should begin to

increase around $F_c/\gamma = 4.75$ GHz (which is observed in Figure 4.2), suggesting that the

current-caused frequency upshift is the most likely explanation. With the upshift in

cutoff frequency, the possibility exists that the interactions at the lower $F_c/\gamma$ values(below

4.75 GHz) are forward wave interactions, which would not be detected as efficiently by

the Vlasov antenna located at the diode end of the interaction cavity. This could account

for the low power detected in the waveguide at $F_c/\gamma$ less than 4.75 GHz.

Figure 4.3 shows the measured frequency range normalized to $F_c/\gamma$, versus the

magnetic field. Figure 4.4 shows the measured frequency range normalized to $F_c/\gamma$,

versus $F_c/\gamma$. In order to be a gyro-backward-wave interaction, $F_c/\gamma$ must be greater than
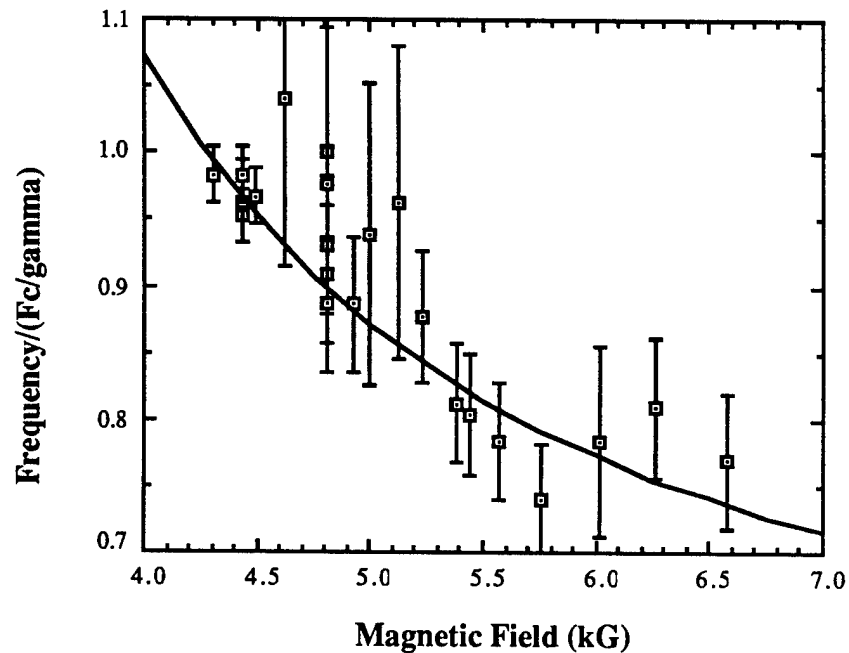


Figure 4.3. The normalized measured frequency range versus magnetic field for the solid beam. Solid line is theory for an e-beam-filled cavity ($\alpha$ = 0.65, E = 750 kV, I = 1.5 kA).

82
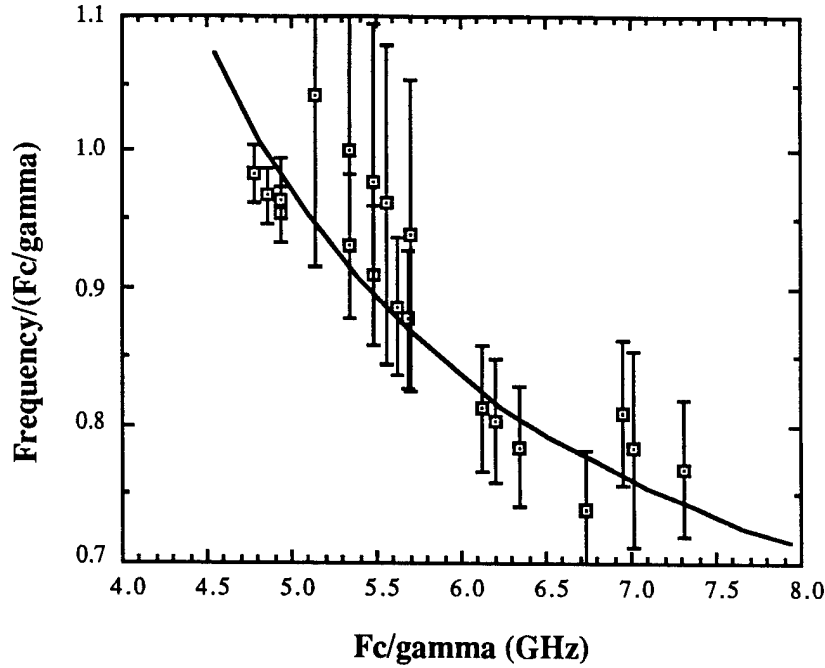


**Figure 4.4. The normalized measured frequency range versus $F_c/\gamma$ for the solid beam. Solid line is theory for an e-beam-filled cavity ($\alpha = 0.65$, $I = 1.5$ kA).**

the measured frequency. The frequency range is determined by the different filters and waveguide bands used. Figure 4.4 proves that the high power signals detected in the experiment are the backward wave interactions. Several of the data points at the lower $F_c/\gamma$ (around 4.6-5.1 GHz) that have a range that exceed 1.0 in the figure were determined without the aid of H-Band waveguide (cutoff frequency of ~5.27 GHz), and could only be said to have a frequency less than 6 GHz. Also evidenced in Figure 4.4 is the non-linear shape of the change in the normalized measured frequency range as $F_c/\gamma$ increases. This is due to the parabolic shape of the cavity dispersion curve. Using an estimated $\alpha$ of 0.65 (discussed below), a voltage of 750 kV, and a current of 1.5 kA, theoretical frequency intersections can be found for the e-beam filled cavity, and are plotted in Figures 4.3 and 4.4. The measured frequency ranges are in good agreement with the theoretical prediction. The inexactness between the measured values and the theory is due to the variations of $\alpha$, beam voltage, and the broadband measurement of the frequencies.

Figures 4.5 - 4.16 show typical data from single shots (and dispersion relation plots) as a function of cavity magnetic fields. Figure 4.5 shows both the G-Band signal ($3.15 \le f \le 6$ GHz, using a 6 GHz low pass filter) and the J-Band signal ($4.3 \le f \le 8$ GHz, using an 8 GHz low pass filter), both with approximately the same attenuation. The two signals are roughly the same, showing the measured frequency is below 6 GHz. In order to narrow the frequency range further, H-Band waveguide (frequency cutoff
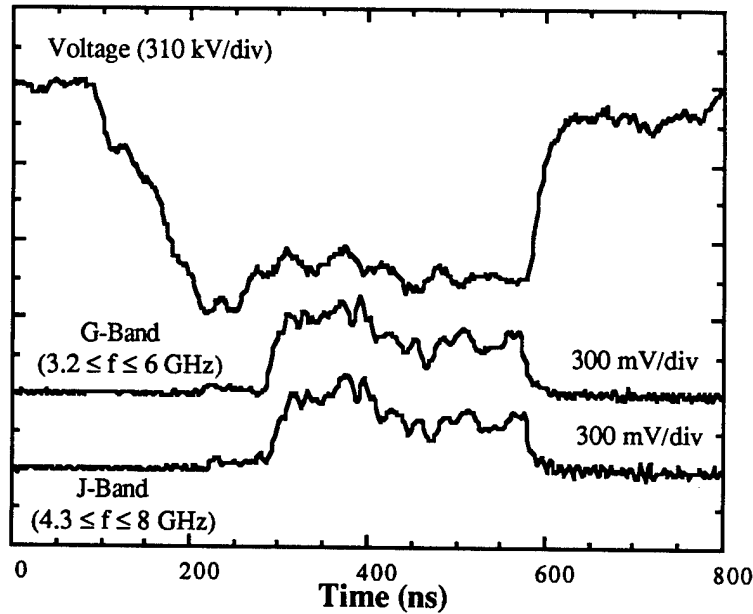


**Figure 4.5.** Data signal from G-Band ($3.15 \le f \le 6$ GHz) and J-Band ($4.3 \le f \le 8$ GHz), which show the frequency of the interaction is between 4.3 and 6 GHz (Shot M2501). The magnetic field is 4.8 kG. The extracted peak power for the two signals is ~ 330 kW

~5.27 GHz) was added to the waveguide detection system. Using the same parameters as in Figure 4.5 (magnetic field ~ 4.8 kG), very little of the signal passes through the H-Band (see Figure 4.6), showing the frequency to be less than 5.27 GHz. This low measured frequency range (4.5 - 5.3 GHz), in conjunction with the $F_c/\gamma$ information, indicates that the signals detected are the $TE_{11}$ fundamental mode backward wave interaction, since the next mode, $TE_{21}$, cutoff exists around 7.8 GHz (see the dispersion relation in Figure 4.7).
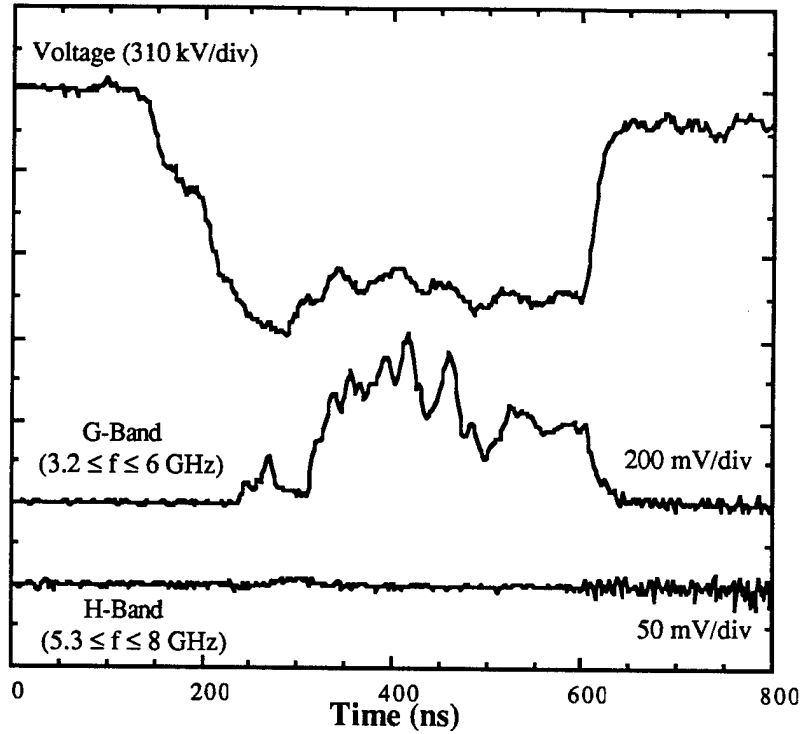
Figure 4.6. Data signals from G-Band (3.15 ≤ f ≤ 6 GHz) and H-Band (5.27 ≤ f ≤ 8 GHz) , which show the frequency of the interaction is less than 5.3 GHz (Shot M2518). The magnetic field is 4.8 kG. The peak extracted power in G-Band is ~ 450 kW.
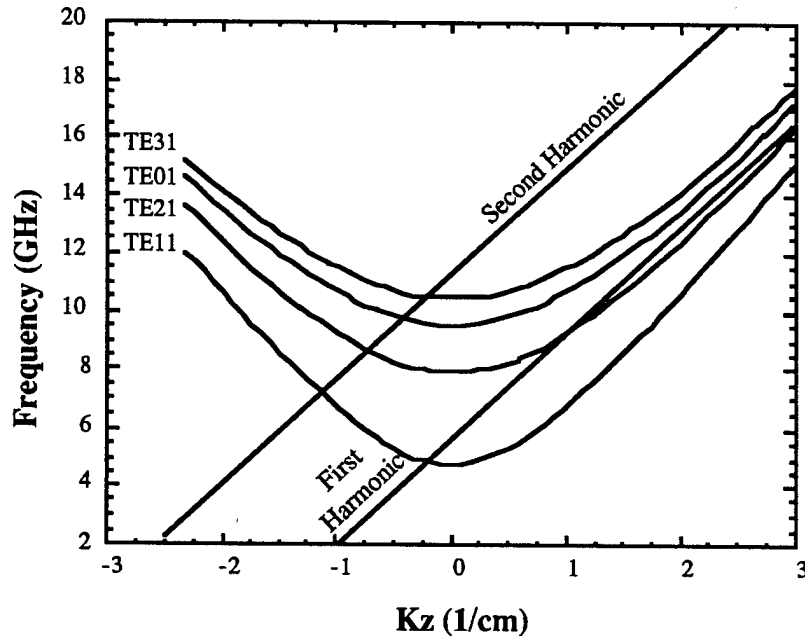


Figure 4.7. The e-beam-filled cavity dispersion relation for shots M2501 and M2518, showing the fundamental and second harmonic frequency intersections. The magnetic field is 4.8 kG, beam energy is 710 kV, and $\alpha$ is 0.65. Fundamental mode lower frequency intersections are: $TE_{11}$ (BW) = 4.94 GHz, $TE_{21}$ (FW) = 9.4 GHz. Second harmonic lower frequency intersections are: $TE_{11}$ (BW) = 7.2 GHz, $TE_{21}$ (BW) = 8.7 GHz.

Figure 4.8 shows an example of the microwave signals in the G-Band ($3.15 \leq f \leq$ 6 GHz) and the 4.67 GHz frequency filter. These signals are comparable in power for lower magnetic fields ($F_c/\gamma \sim$ 4.9 GHz), but are not very large ($\sim$ 40 - 80 kW). As the magnetic field increases, the frequency filter signal decreases whereas the G-band ($3.15 \leq f \leq$ 6 GHz) signal increases, suggesting that most of the microwave power exists at frequencies above 4.67 GHz. This is consistent with the cutoff frequency upshift discussed above. Figure 4.9 shows the e-beam-filled cavity (e-beam current $\sim$ 1.5 kA) dispersion relation for Figure 4.8.
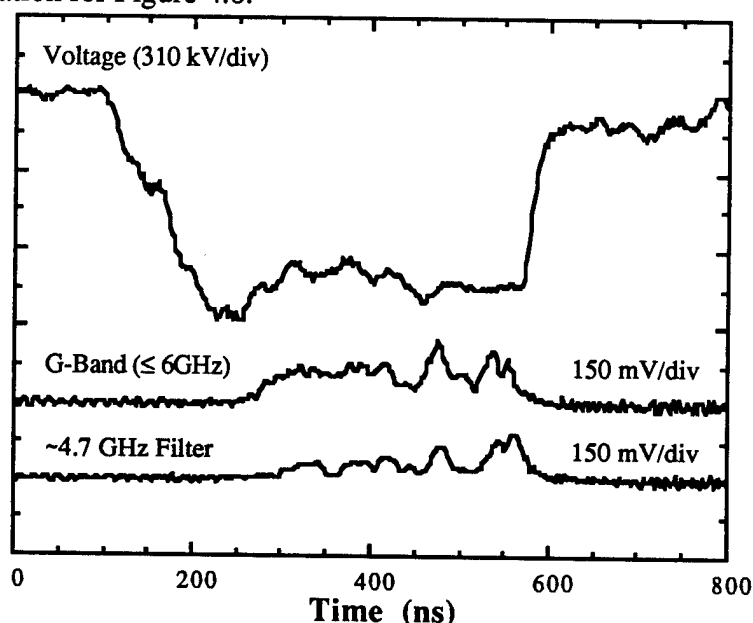


**Figure 4.8. Data signals from G-Band ($3.15 \leq f \leq 6$ GHz) and the 4.67 GHz frequency filter (10 dB width 4.65 - 4.75 GHz) (Shot M2512). The magnetic field is 4.4 kG. The peak extracted power for the two signals is approximately 80 kW.**

Figures 4.10 - 4.13 show the magnetic tunability of the signal and another way of proving the existence of the backward wave. As the magnetic field is increased from 5.2 - 6.7 kG, the signal detected in H-Band begins to increase in power and the pulse shape matches the signal detected in G-Band ($3.15 \leq f \leq 6$ GHz). Thus as the magnetic field increases (and $F_c/\gamma$ increases), the gyro-BWO frequency intersection increases, which is shown in the e-beam filled cavity dispersion relations depicted in Figures 4.14 - 4.16.

This is consistent for the backward wave interaction, since for the case of the forward

wave interaction near cutoff (a gyrotron interaction), the frequency should decrease as the

magnetic field is increased. From Figure 4.11, the H-Band (5.27 ≤ f ≤ 8 GHz) signal is

roughly half of the G-Band (3.15 ≤ f ≤ 6 GHz) signal, which can be used to estimate α.

Using the known voltage and magnetic field at which the interaction occurs, plus the

cutoff frequency of H-Band (~5.27 GHz), the dispersion relation (see figure 4.15) is

used to give an α estimate of ~ 0.65. This is consistent with the upper bound α results

of the EGUN code (discussed earlier) for the stated parameters.
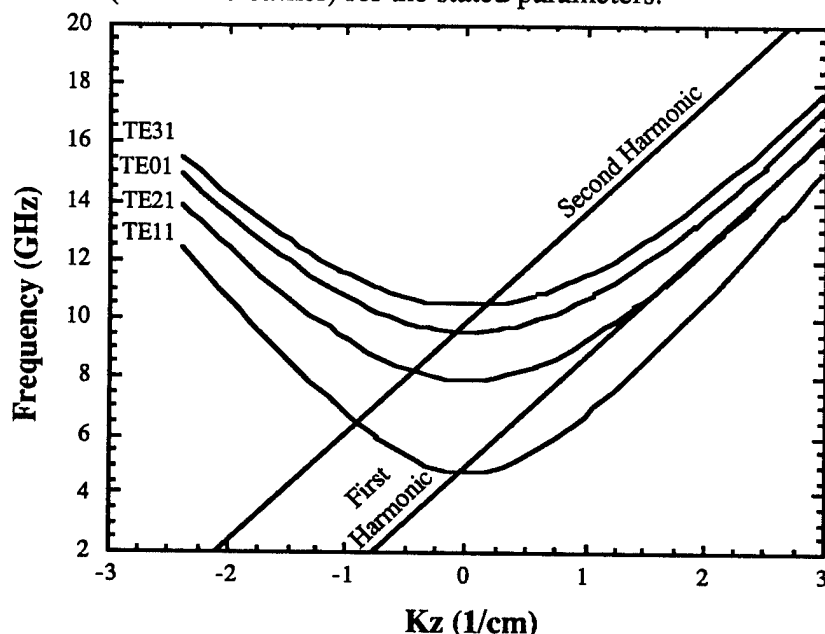


**Figure 4.9. The e-beam-filled cavity dispersion relation for shot M2512, showing the fundamental and second harmonic frequency intersections. The magnetic field is 4.4 kG, beam energy is 775 kV, and α is 0.6. Fundamental mode lower frequency intersections are: TE$_{11}$ (BW) = 4.75 GHz, TE$_{21}$ (FW) = 11.6 GHz. Second harmonic lower frequency intersections are: TE$_{11}$ (BW) = 6.4 GHz, TE$_{21}$ (BW) = 8.2 GHz.**

The initial peaks observed in Figures 4.12 - 4.13 are also the TE$_{11}$ fundamental

mode backward wave interaction, as shown by the dispersion relation in Figure 4.17.

This interaction occurs at a frequency of ~5.3 GHz, since it is detected in both G-Band

(3.2 ≤ f ≤ 6 GHz) and H-Band (5.26 ≤ f ≤ 8 GHz), at approximately half the amplitude

of the G-band signal. The peaks occur at a higher voltage (~850 - 900 kV) than the
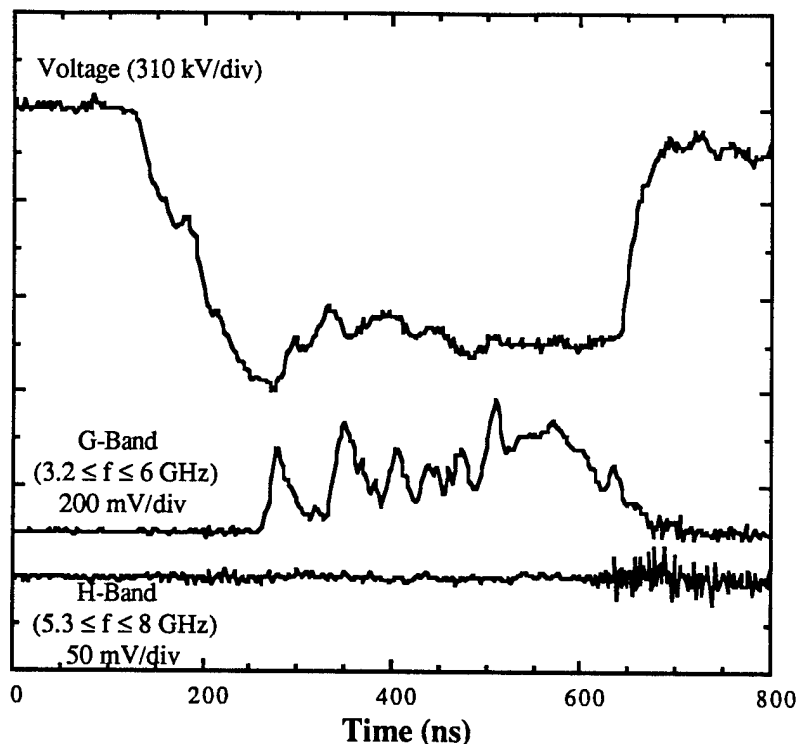
**Figure 4.10.** Data signals from G-Band (3.15 ≤ f ≤ 6 GHz) and H-Band (5.27 ≤ f ≤ 8 GHz), which show the frequency of the interaction is less than 5.3 GHz (Shot M2527). The magnetic field is 5.2 kG.
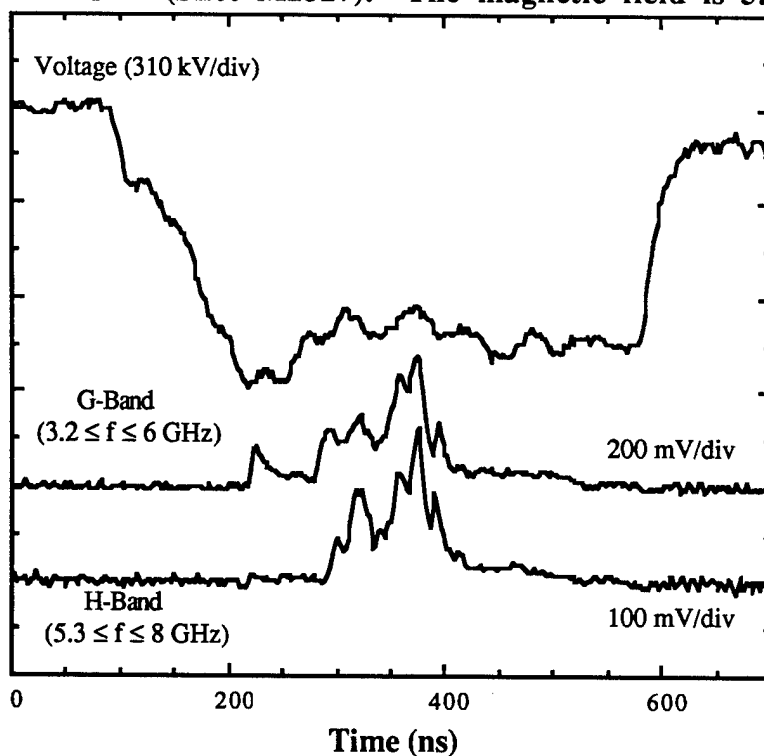


**Figure 4.11.** Data signals from G-Band (3.15 ≤ f ≤ 6 GHz) and H-Band (5.27 ≤ f ≤ 8 GHz), which show the frequency of the interaction is between 5.3 and 6 GHz (Shot M2521). The magnetic field is 6.0 kG.

88
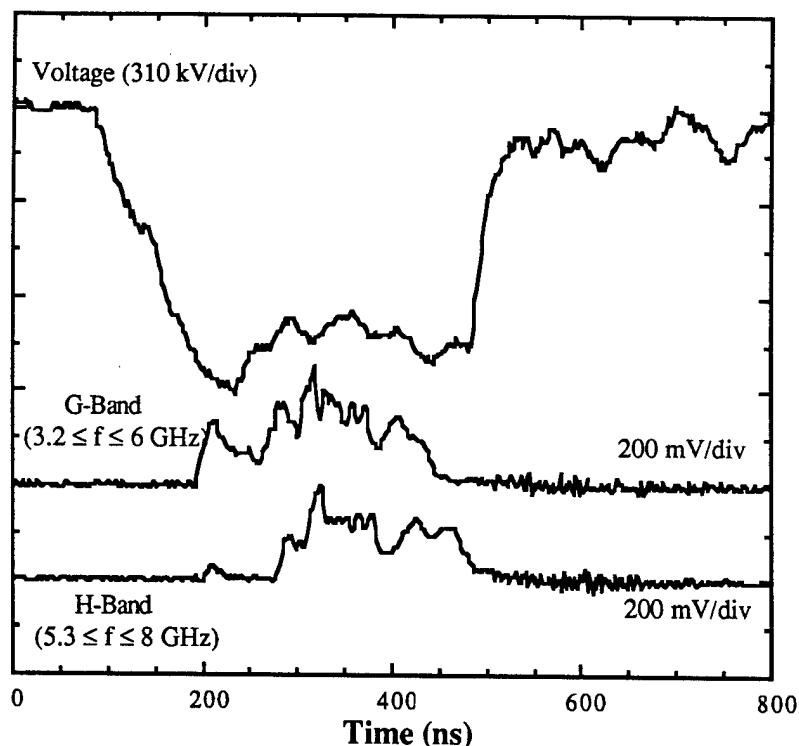


Figure 4.12. Data signals from G-Band (3.15 ≤ f ≤ 6 GHz) and H-Band (5.27 ≤ f ≤ 8 GHz), which show the frequency of the interaction is between 5.3 and 6 GHz (Shot M2525). The magnetic field is 6.3 kG.
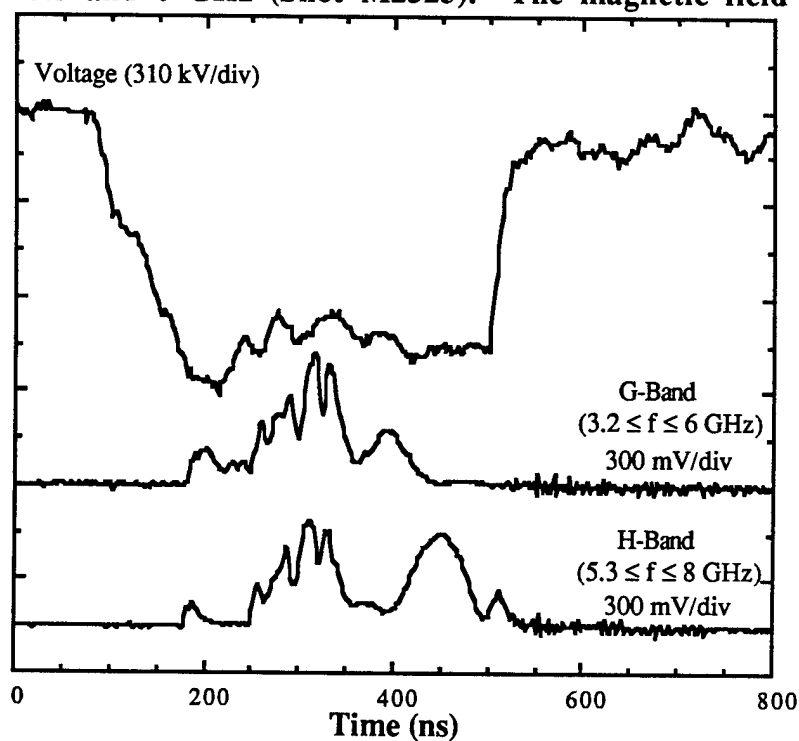


Figure 4.13. Data signals from G-Band (3.15 ≤ f ≤ 6 GHz) and H-Band (5.27 ≤ f ≤ 8 GHz), which show the frequency of the interaction is between 5.3 and 6 GHz. The last peak in H-Band has a frequency between 6 and 8 GHz (Shot M2524). The magnetic field is 6.6 kG.

89
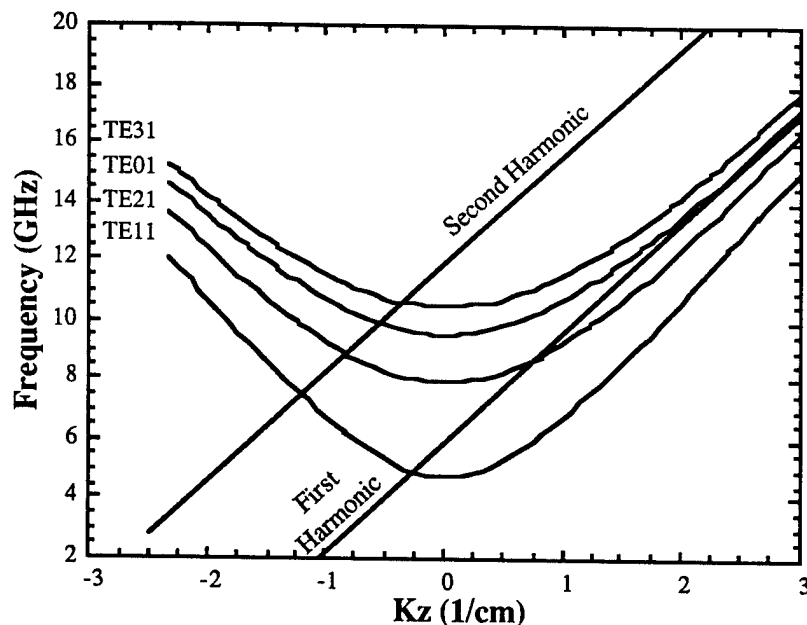


Figure 4.14.  The e-beam-filled cavity dispersion relation for shot M2527, showing the fundamental and second harmonic frequency intersections.  The magnetic field is 5.2 kG, beam energy is 750 kV, and $\alpha$ is 0.65.  Fundamental mode lower frequency intersections are: $TE_{11}$ (BW) = 5.0 GHz, $TE_{21}$ (FW) = 8.8 GHz. Second harmonic lower frequency intersections are: $TE_{11}$ (BW) = 7.5 GHz, $TE_{21}$ (BW) = 8.9 GHz.
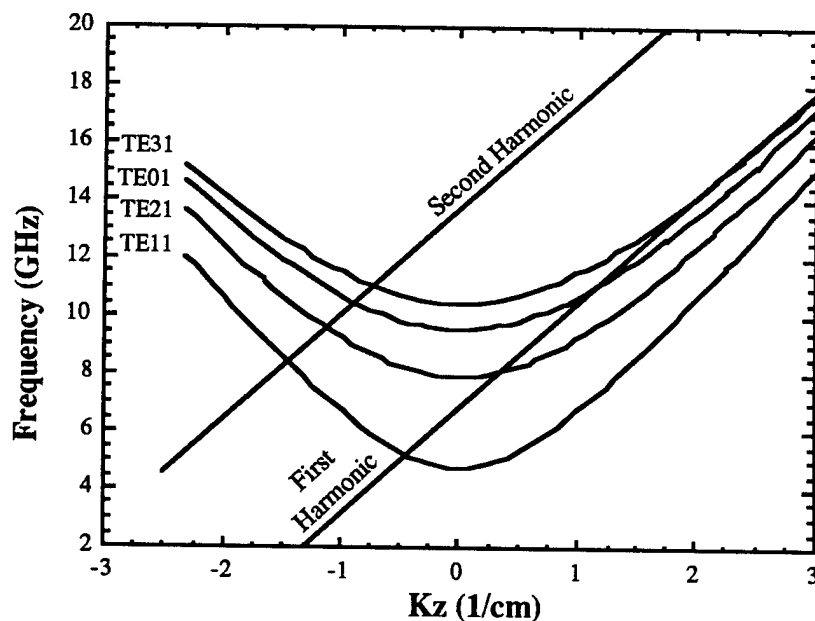


Figure 4.15.  The e-beam-filled cavity dispersion relation for shot M2521, showing the fundamental and second harmonic frequency intersections.  The magnetic field is 6.0 kG, beam energy is 750 kV, and $\alpha$ is 0.65.  Fundamental mode lower frequency intersections are: $TE_{11}$ (BW) = 5.26 GHz, $TE_{21}$ (FW) = 8.2 GHz. Second harmonic lower frequency intersections are: $TE_{11}$ (BW) = 8.4 GHz, $TE_{21}$ (BW) = 9.6 GHz.
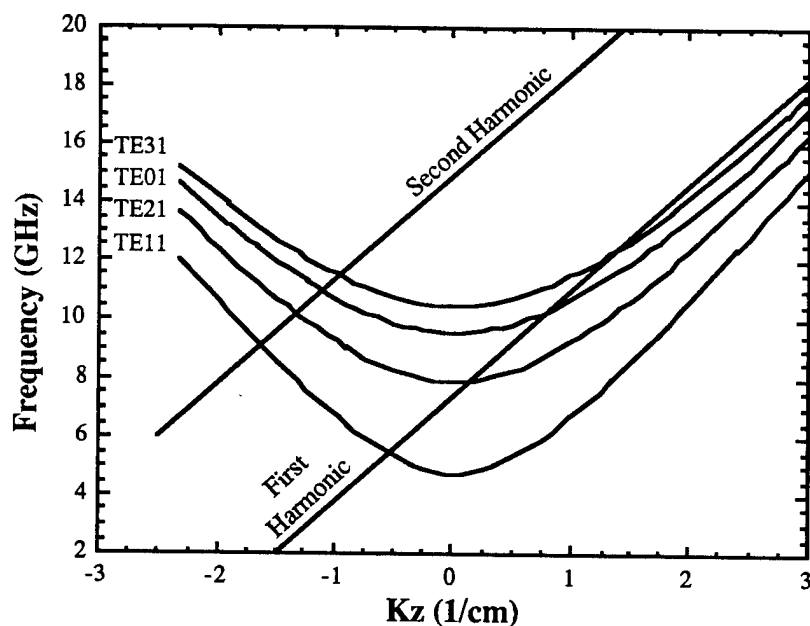
Figure 4.16. The e-beam-filled cavity dispersion relation for shot M2524, showing the fundamental and second harmonic frequency intersections. The magnetic field is 6.6 kG, beam energy is 775 kV, and $\alpha$ is 0.7. Fundamental mode lower frequency intersections are: $TE_{11}$ (BW) = 5.5 GHz, $TE_{21}$ (FW) = 7.9 GHz. Second harmonic lower frequency intersections are: $TE_{11}$ (BW) = 9.1 GHz, $TE_{21}$ (BW) = 10.1 GHz.
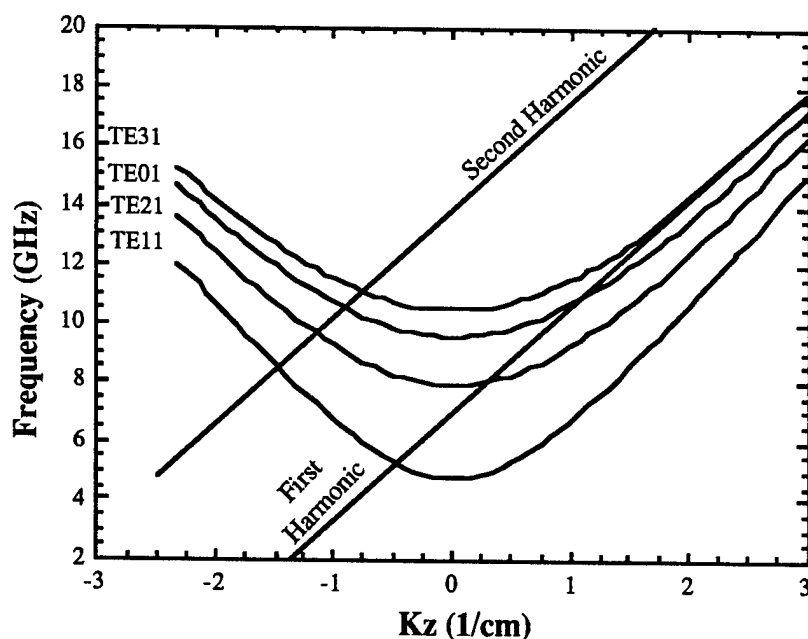


Figure 4.17. The e-beam-filled cavity dispersion relation for shot M2524, showing the fundamental and second harmonic frequency intersections. The magnetic field is 6.6 kG, beam energy is 850 kV, and $\alpha$ is 0.7. Fundamental mode lower frequency intersections are: $TE_{11}$ (BW) = 5.3 GHz, $TE_{21}$ (FW) = 8.1 GHz. Second harmonic lower frequency intersections are: $TE_{11}$ (BW) = 8.5 GHz, $TE_{21}$ (BW) = 9.1 GHz, $TE_{01}$ (BW) = 10.6 GHz, $TE_{31}$ (BW) = 11.1 GHz.

longer microwave signals, but do not remain in resonance since the voltage rapidly drops to ~700 - 775 kV for the rest of the voltage pulse.

Other peaks which occur toward the end of the voltage pulse for Figures 4.12 and 4.13 in H-Band ($5.27 \leq f \leq 8$ GHz) but not in G-Band ($3.15 \leq f \leq 6$ GHz) are concluded to lie in the frequency range of 6 - 8 GHz; these peaks could be the $TE_{21}$ fundamental absolute instability (see Figure 4.17) competing with the $TE_{11}$ fundamental cyclotron mode backward wave interaction. This is expected to occur, since the $TE_{21}$ intersection occurs near the $TE_{21}$ frequency cutoff, w. ereas the $TE_{11}$ intersection is well above the $TE_{11}$ cutoff frequency; note that modes closer to cutoff have a larger absolute instability growth rate, and a higher diffraction Q which gives a lower starting current for the gyro-BWO.

For lower magnetic fields (~4.1 kG, $F_c/\gamma$ ~ 4.4 -4.6 GHz), the possibility exists that other interactions were detected, most notably the second harmonic $TE_{11}$ or $TE_{21}$ backward wave interactions. The intersections are shown in Figure 4.18 ($TE_{11}$ ~ 6.1 GHz, $TE_{21}$ ~ 7.8 GHz). The measured frequency range for the above parameters was 4.3 - 10 GHz (a 10 GHz low pass filter was used on J-Band, with $4.3 \leq f \leq 10$ GHz). The power detected was 10 - 15 dB less (measured at about ~ 5 - 25 kW) than the higher magnetic field cases, suggesting the fundamental mode interaction is much stronger than the second and higher harmonic interactions. These harmonics probably exist for the higher magnetic fields as well, but were not detected on later experiments since the upper range of the measured frequency is 8 GHz (an 8 GHz lowpass filter is used on the H-Band signal), and the frequency of the second (and higher) harmonic intersections are greater than 8 GHz (see figure 4.17). Second harmonic operation and competition has been previously observed in gyrotron experiments [Bra90, Ide91]. Further investigation is needed to determine if these higher harmonics are present and if they produce a large amount of power which is subject to mode competition between the fundamental and higher harmonic modes.
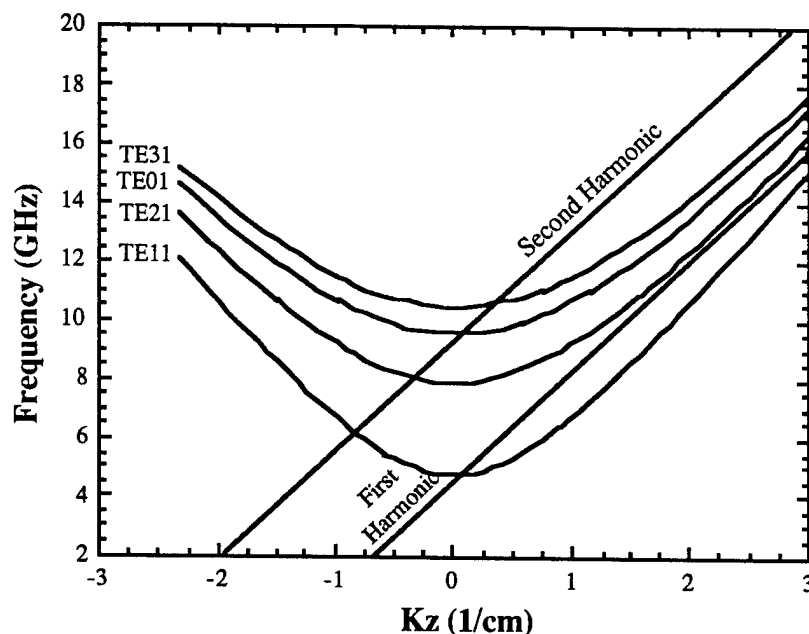
**Figure 4.18.** The e-beam-filled cavity dispersion relation for shot M2486, showing the first and second harmonic frequency intersections. The magnetic field is 4.1 kG, beam energy is 750 kV, and $\alpha$ is 0.6. Fundamental mode lower frequency intersections are: $TE_{11}$ (BW) = 4.75 GHz. Second harmonic lower frequency intersections are: $TE_{11}$ (BW) = 6.2 GHz, $TE_{21}$ (BW) = 8.1 GHz, $TE_{01}$ (BW) = 9.6 GHz, $TE_{31}$ (FW) = 10.6 GHz.

## 4.2. Annular Beam Results

Experiments were conducted with the 24 hole apertured-masked anode, which provided ~150 - 300 amps of electron beam current. These experiments employed the same waveguide detection system, including the H-Band waveguide ($5.27 \le f \le 8$ GHz), as in the solid beam results. Figure 4.19 and Figure 4.20 show the peak cyclotron maser power detected in the waveguide system as a function of magnetic field and $F_c/\gamma$, respectively. Peak extracted power ranges from ~ 10 - 300 kW, depending on where the resonance interaction occurs. The maximum power occurs over an $Fc/\gamma$ range of 6.2 - 6.5 GHz. The circles in both Figure 4.19 and 4.20 show the highest powers, but this occurs over a short pulselength (~ 40 - 100 ns) at the beginning of the voltage pulse where the voltage is highest, and in a magnetic field range of 5.7 - 6.6 kG. These powers (ranging from 100 - 300 kW) correspond to an efficiency of ~ 1 -2%
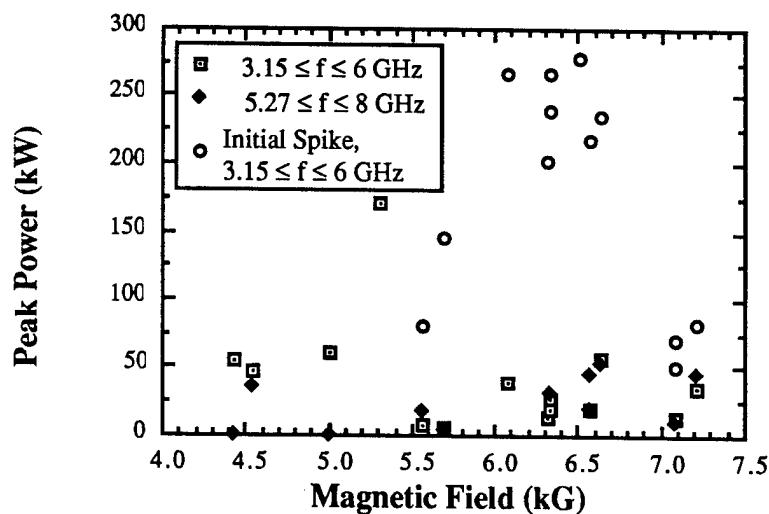
**Figure 4.19.** Peak power measured in the waveguide detection system as a function of the magnetic field for the annular beam.
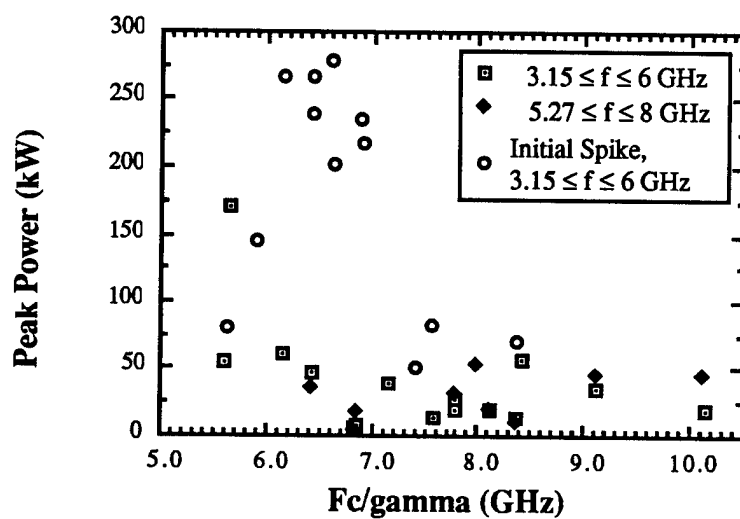


**Figure 4.20.** Peak power measured in the waveguide detection system as a function of $F_c/\gamma$ for the annular beam.

when taking into account the efficiency of the Vlasov-antenna. The other data points in Figure 4.21 and 4.22 are for the signals that occur during the flat part of the voltage pulse (10 - 80 kW in the antenna) which leads to an efficiency of only 0.1 - 1% after taking into account the detection efficiency of the Vlasov-antenna. Calorimetry results also gave an average power estimate of 100 - 800 kW (for the total tube microwave signals), in rough agreement with the diode detector measurements.

Figures 4.21 and 4.22 show the measured frequency range normalized to $Fc/\gamma$ versus the magnetic field and $Fc/\gamma$, respectively. Since the normalized frequency range is less than one, the interactions are the backward-wave. Using an estimated $\alpha$ of 0.65, beam voltage of 650 kV, and a current of 300 amps, the theoretical frequency intersections are plotted in Figures 4.21 and 4.22. The theoretical prediction and measured frequencies are in good agreement, with the inexactness between the two arising from variations in $\alpha$, beam voltage, and the broadband frequency measurements.
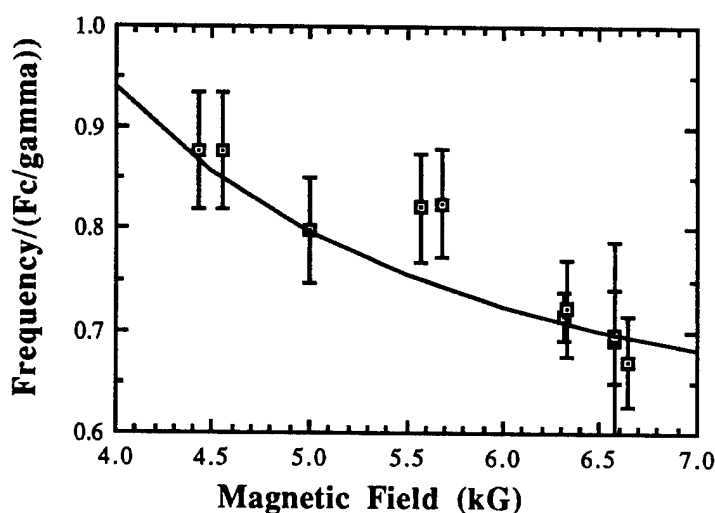


Figure 4.21. The normalized measured frequency range versus magnetic field for the annular beam. Solid line is theory for an e-beam-filled cavity ($\alpha$ = 0.65, E = 650 kV, I = 300 A).
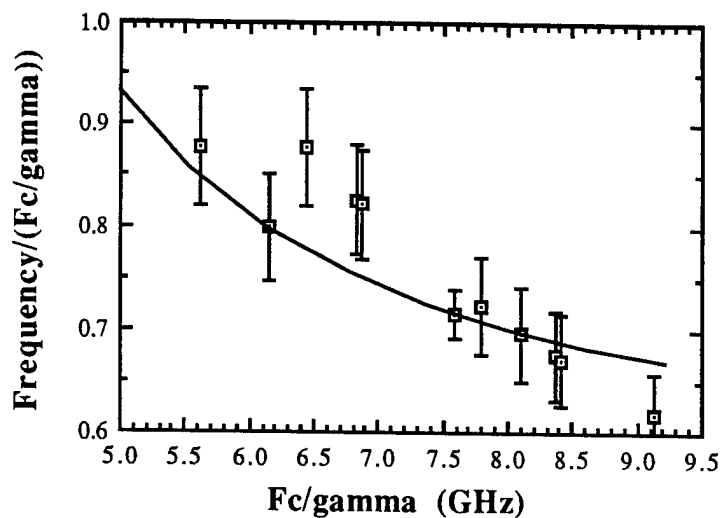
**Figure 4.22.** The normalized measured frequency range versus $F_c/\gamma$ for the annular beam. Solid line is theory for an e-beam-filled cavity ($\alpha$ = 0.65, I = 300 A).
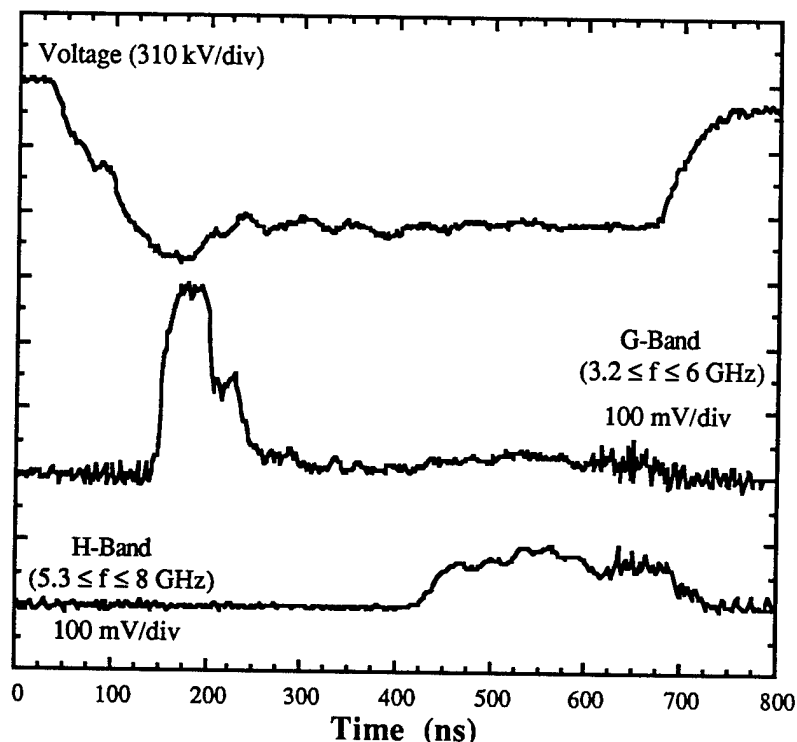


**Figure 4.23.** Data signal from G-Band (3.15 ≤ f ≤ 6 GHz) and H-Band (5.27 ≤ f ≤ 8 GHz), which show the initial high peak extracted power (~150 kW) frequency ( ≤ 5.3 GHz) interaction and the low extracted power (~10 kW) frequency (5.27 ≤ f ≤ 6 GHz) interaction (Shot M2566). The magnetic field is 5.7 kG.

Figure 4.23 shows a typical single data shot of the large initial pulse where the greatest extracted power occurs for the annular beam (see Figure 4.20). The magnetic field for Figure 4.23 is ~ 5.7 kG. The large initial peak in Figure 4.23 corresponds to approximately 150 kW and occurs in the G-Band signal ($3.15 \leq f \leq 6$ GHz) during the start of the voltage pulse. Again, as seen in the solid beam results, the interaction does not remain in resonance due to the large drop in voltage from ~ 850 kV to ~ 650 kV. Since this large initial microwave pulse does not occur in the H-Band signal, the signal is concluded to have a frequency of less than 5.3 GHz. This interaction is the $TE_{11}$ backward-wave intersection and occurs at ~ 4.8 GHz (close to the cavity cutoff of ~4.6 GHz), as shown by the dispersion relation given in Figure 4.24.
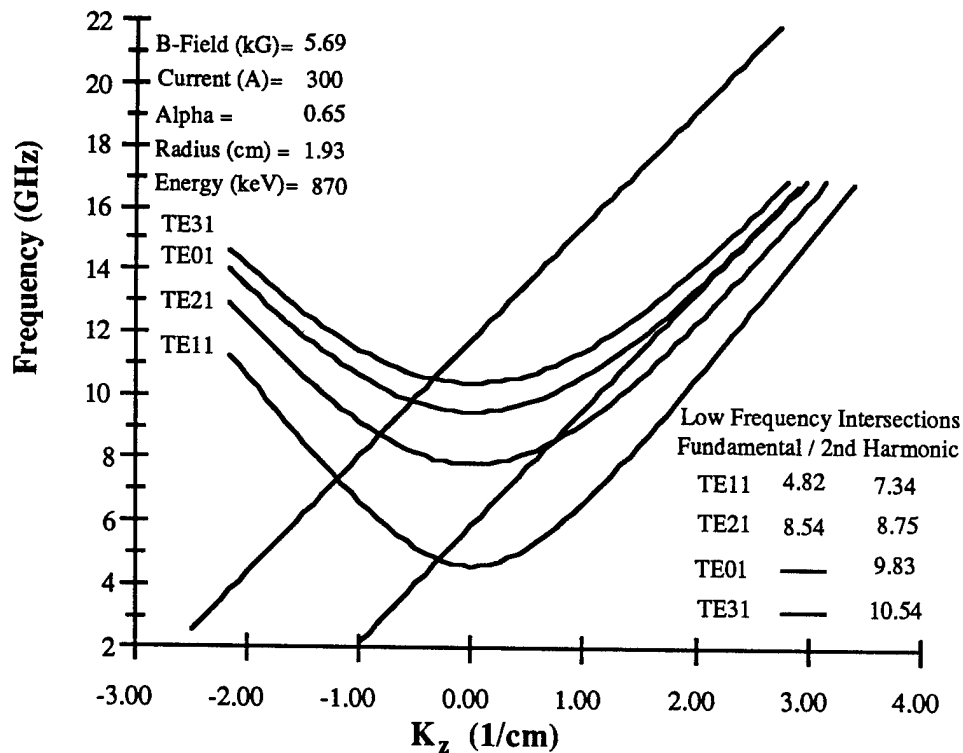
Figure 4.24. Dispersion Relation for the initial high power peak in the G-Band signal ($3.15 \leq f \leq 6$ GHz) on Shot M2566.

The H-Band signal (5.27 ≤ f ≤ 8 GHz) that appears towards the end of the voltage pulse in Figure 4.23 has a peak extracted power of about 10 kW. This H-Band signal is also in the G-Band (3.15 ≤ f ≤ 6 GHz) signal, although this is not immediately evident from Figure 4.23. Since the two traces were obtained at different attenuations, the G-Band (3.15 ≤ f ≤ 6 GHz) signal was expanded (and an 11 point smooth function was applied to the G-Band signal to remove the digitized noise of the expansion) to show that the latter part of the H-Band and G-Band signals were actually the same. Figure 4.25 shows the expanded view of the microwave signals from Figure 4.23, proving the low power interaction was in both bands and has a frequency range of 5.27 ≤ f ≤ 6 GHz. Figure 4.26 shows the dispersion relation for the low power interaction and shows that the frequency intersection occurs at approximately 5.2 GHz. Since this interaction occurs
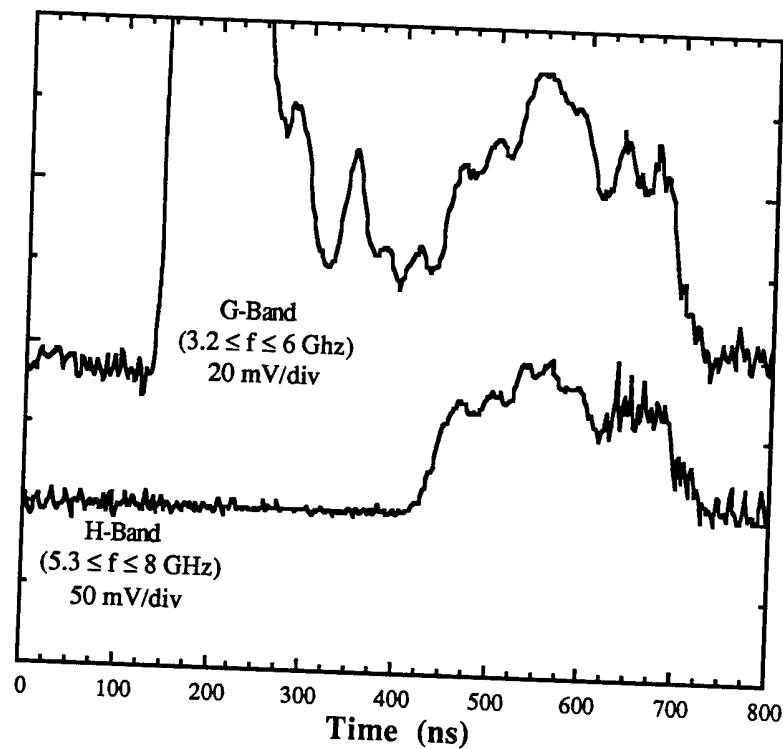


**Figure 4.25.** Expanded view of the G-Band (3.15 ≤ f ≤ 6 GHz) and H-Band (5.27 ≤ f ≤ 8 GHz) signals from Figure 4.23, showing the low power interaction occurs for 5.23 ≤ f ≤ 6 GHz.

B-Field (kG)= 5.7
Current (A)= 300
Alpha = 0.65
Radius (cm) = 1.93
Energy (keV)= 682

TE31
TE01
TE21
TE11

Frequency (GHz)

Low Frequency Intersections
Fundamental / 2nd Harmonic

|  | Fundamental | 2nd Harmonic |
|---|---|---|
| TE11 | 5.13 | 8.37 |
| TE21 | 7.98 | 9.54 |
| TE01 | 10.94 | 10.42 |
| TE31 | 14.79 | 10.99 |

$K_z$ (1/cm)
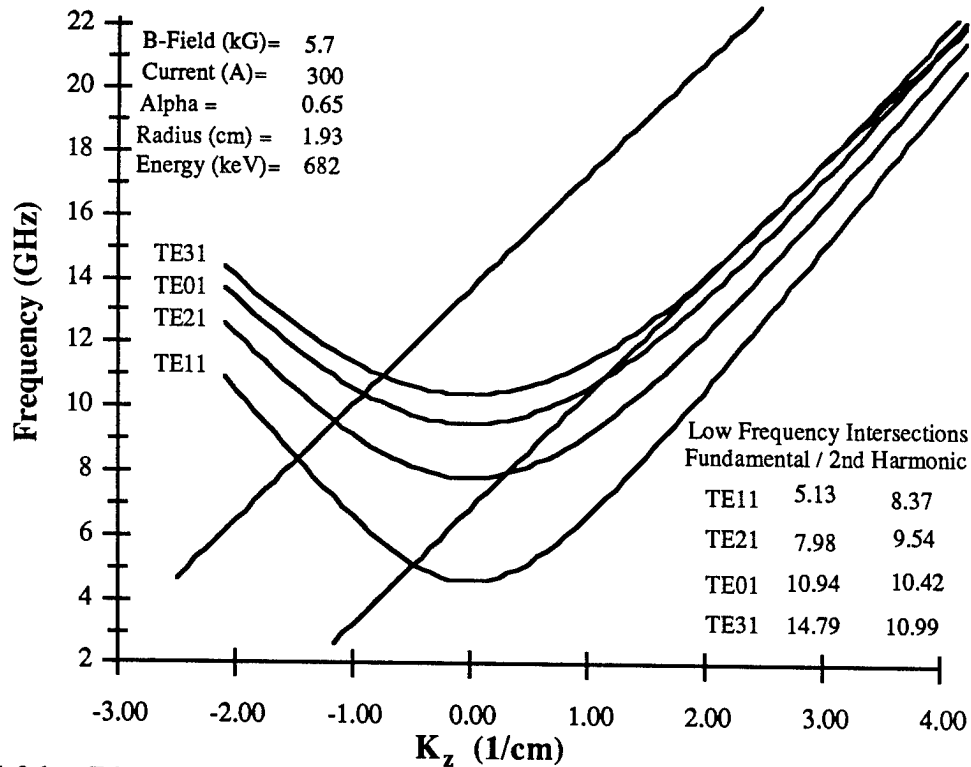
**Figure 4.26.** **Dispersion Relation for the low power signals in Figure 4.25 (Shot M2566).**

farther away from the cavity cutoff, the growth rate will be less than that of the initial high power interaction of ~ 4.8 GHz that is observed at the start of the voltage pulse. The differences in the growth rate may be a contributing factor in the differences in the powers at the two different intersections. The threshold current for the low power interaction can be found to be approximately 65 amps (using equations (2.59) and using a diffractive quality factor of ~1700, the maximum Q from equation (2.61)). This starting current will be greater than for the lower frequency (~ 4.8 GHz), higher power interaction which is approximately 15 amps. Thus, since both are much less than the beam current, the difference in the starting currents probably does not contribute to the differences in the powers of the two intersections.

In an effort to match the resonance condition seen in the initial peak, high power, signal of Figure 4.23 to the flat top voltage of ~ 650 kV, the magnetic field was lowered to ~ 5.0 kG, as shown in the data of Figure 4.27. Figure 4.28 shows the dispersion relation obtained as a result of this lowering of the magnetic field. From Figure 4.27, the

resonance interaction remains tuned for almost the entire flat-top voltage. The peak

extracted power obtained during the pulse is ~ 80 kW, which is less than that obtained

from the initial peak signals at the higher voltages, but lasts for ~ 630 ns which is much

greater than those with initial peak signals of ~ 40 - 100 ns. This means there would be

more delivered energy from the longer pulse microwave interaction. This also suggests

another reason as to why the extracted powers are larger for the high voltage (850 kV),

initial microwave signals . The reason may be that at higher voltages, the electrons have

more perpendicular energy (higher α) to give to the electromagnetic waves, resulting in

more extracted power, and thus a higher efficiency (as discussed in Chapter II, from

equation (2.47) and shown in Figure 2.7).

Figures 4.25 and 4.27 also demonstrate the magnetic tunability of the signal. As

the magnetic field was lowered from 5.7 to 5.0 kG, the flat-top voltage interaction
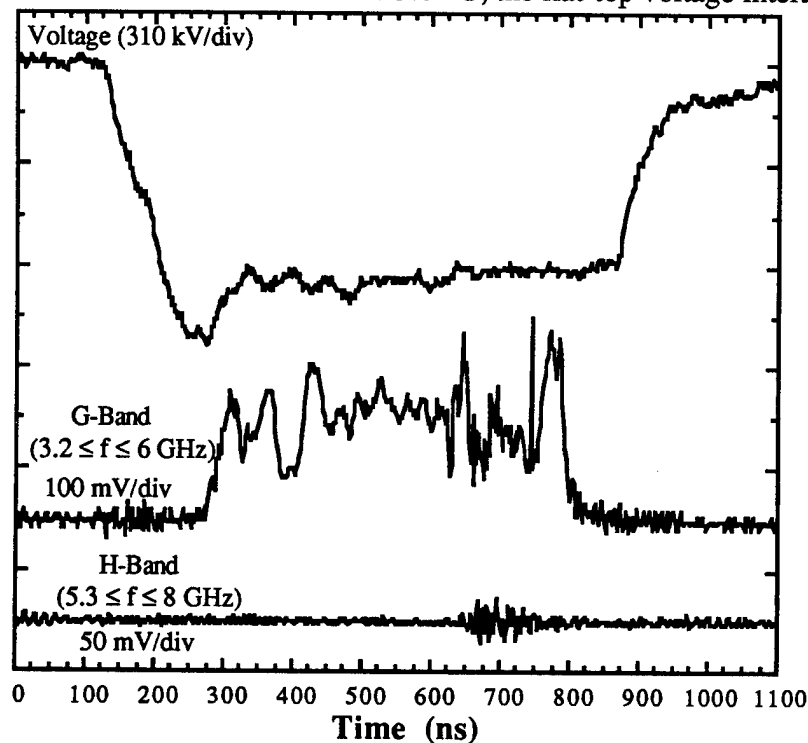


Figure 4.27. Data signal from G-Band (3.15 ≤ f ≤ 6 GHz) and H-Band (5.27 ≤ f ≤ 8 GHz), which show the frequency is less than 5.27 GHz (Shot M2567). Note that the pulselength of the microwaves is ~ 630 ns. The peak extracted power is ~ 80 kW. The magnetic field is 5.0 kG.
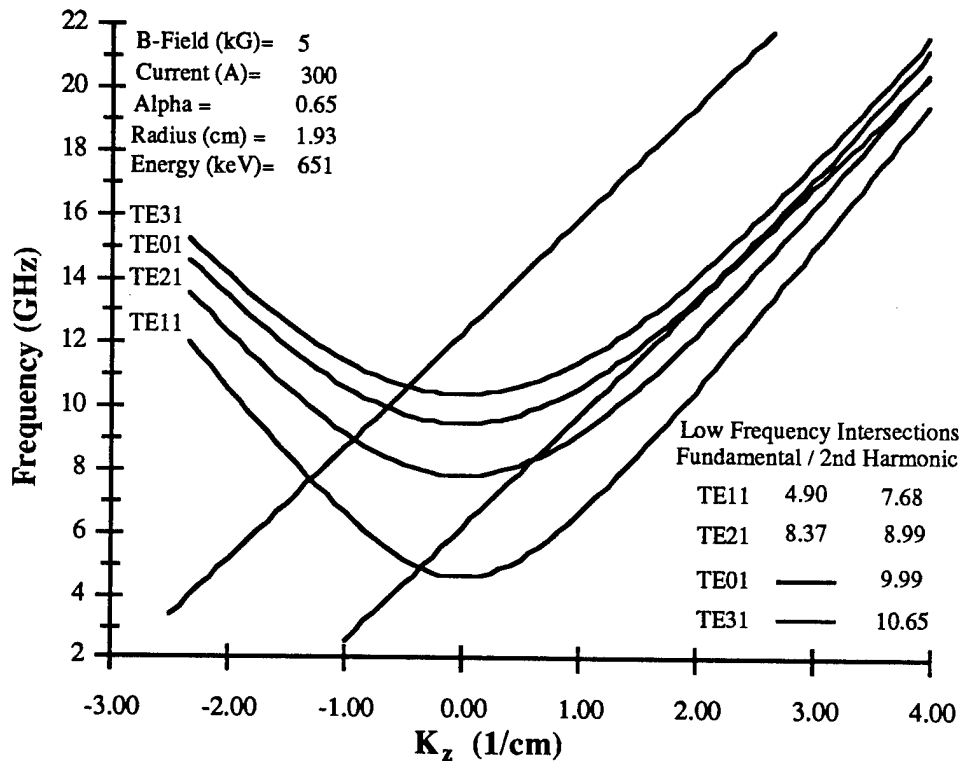
**Figure 4.28. Dispersion Relation showing the resonance condition at 5.0 kG at a flat-top voltage of 650 kV (Shot M2567).**

disappeared from the H-Band waveguide ( $5.27 \leq f \leq 8$ GHz) detector. This again, as

discussed above for the solid beam, proves the existence of the backward-wave, since the

frequency of the interaction decreases as the magnetic field decreases.

Other microwave signals were also observed when the voltage drooped

dramatically during a data shot. Figure 4.29 shows a typical data shot where the voltage

droops to ~ 420 kV. For this particular shot (M2572) the magnetic field was ~ 6.6 kG.

Noting that the late time signal appears in the H-Band waveguide ($5.27 \leq f \leq 8$ GHz)

detector and not the G-Band waveguide ($3.15 \leq f \leq 6$ GHz) detector shows the frequency

of the signal lies between 6 and 8 GHz. Note that the attenuation difference between the

two bands shown in Figure 4.29 is only 3 dB, so the conclusion of the frequency range

of $6 \leq f \leq 8$ GHz is valid without further expanding the frequency signals as discussed

above. Figure 4.30 gives the dispersion relation for the low voltage intersection (at about

6.71 GHz), again demonstrating a $TE_{11}$ backward-wave interaction. This low voltage

interaction also shows that the threshold current for the oscillation is below 200 amps (the
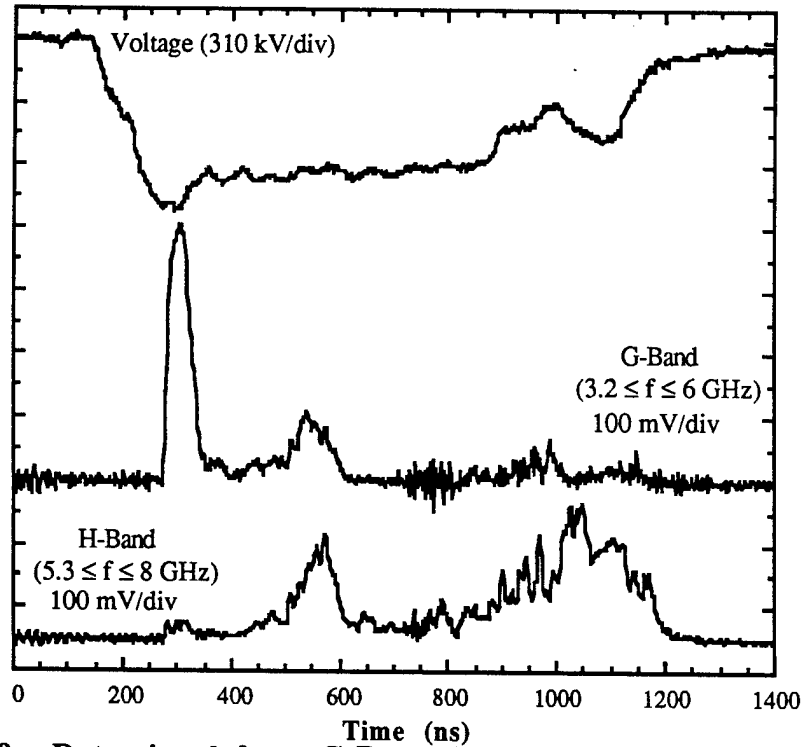
**Figure 4.29.** Data signal from G-Band (3.15 ≤ f ≤ 6 GHz) and H-Band (5.27 ≤ f ≤ 8 GHz), which show the low voltage frequency is 6 ≤ f ≤ 8 GHz (Shot M2572). The H-band signal peak power is ~ 45 kW. The G-Band initial pulse peak power is ~ 200 kW.
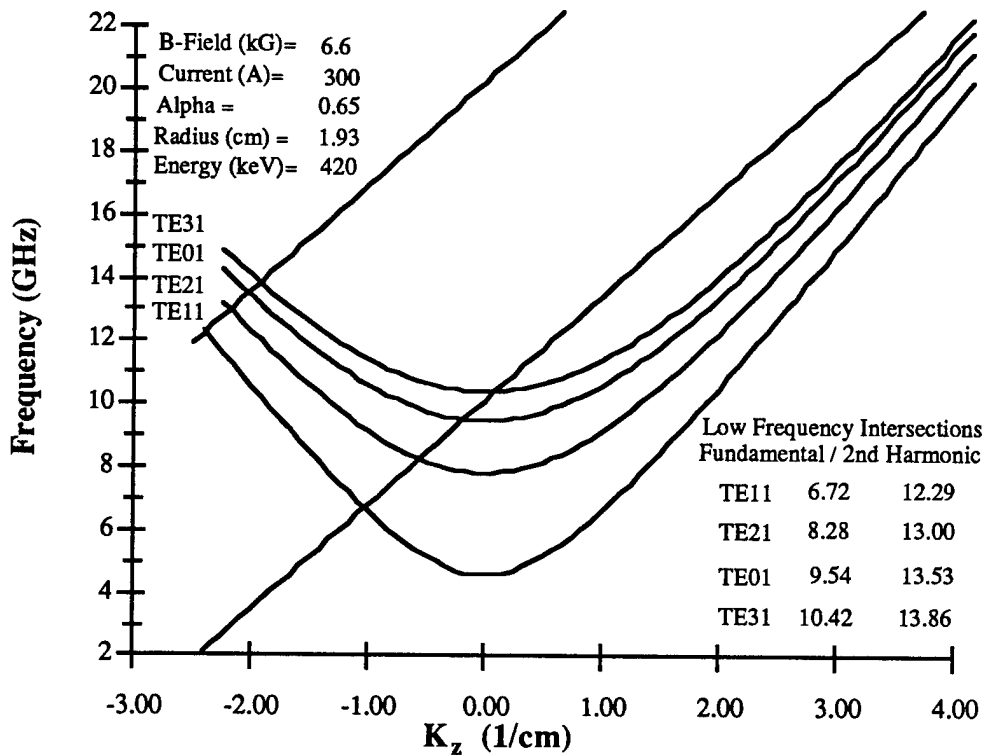


**Figure 4.30.** Dispersion relation for the peak H-Band (5.3 ≤ f ≤ 8 GHz) signal that occurs when the voltage is low in Figure 4.29 (shot M2572).

measured current was ~200 amps), which agrees with the theoretical threshold current given by equation (2.59) of ~ 100 amps .

## 4.3. Comparison of the Annular and Solid Beam Results

Figure 4.31 shows the peak extracted power as a function of the electron beam current. As discussed above in section 4.2, the circles show the microwave signals observed from the initial high voltage spike of the voltage pulse. The solid beam (with currents of 1 - 2 kA) provides the highest powers, typically 5 - 10 times higher than those obtained from the annular beam (currents ~ 200 - 300 amps) along the flat-top voltage, and 2 - 4 times higher than the annular beam high voltage peak signals. Note that Figure 4.31 includes all of the peak power data points, thus will include low powers for non-optimized conditions. For similar magnetic fields and voltages (see Figures 4.2 and 4.20), the power is greater for the higher current (solid beam) condition. The relative efficiency of the annular beam is approximately the same as that of the solid beam. This demonstrates that the gyro-BWO is insensitive to the e-beam energy spread which is
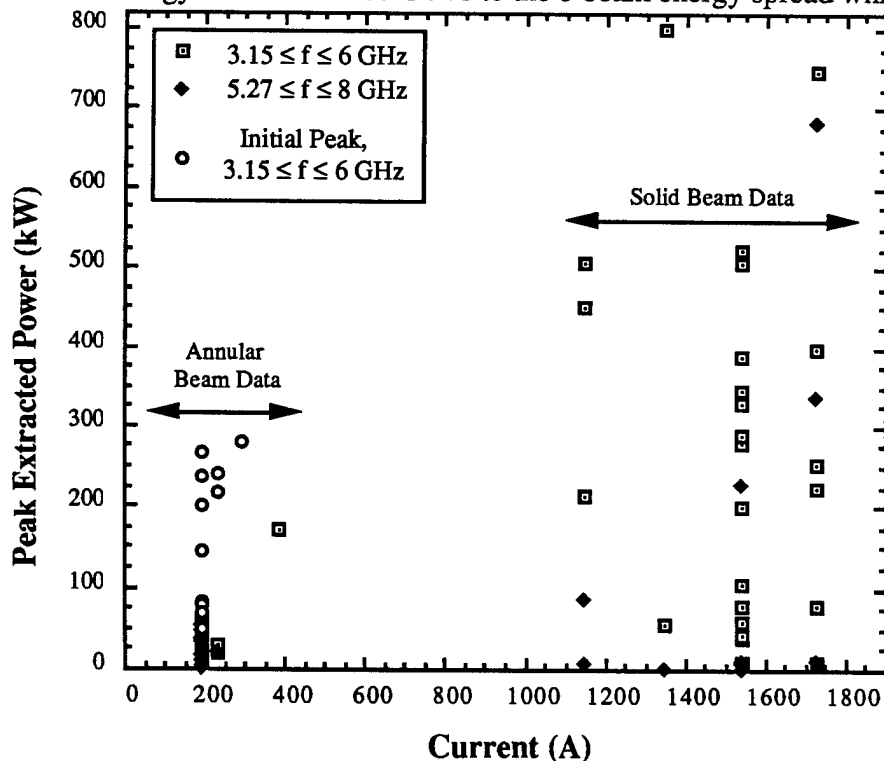
Figure 4.31. Microwave peak power as a function of the beam current for the annular and solid electron beams.

much greater for the solid beam. The implication is that more current is needed for more extracted power, but using a solid beam only increases the power and not the efficiency.

A reason for the relatively low efficiency of the annular beam may be the smaller growth rate of the lower currents (the growth rate is directly dependent on the current). Some possible explanations for the low efficiency of the solid beam are the space-charge limiting effect on the beam in the interaction cavity, reabsorbtion of the microwave power in the interaction cavity, or that only part of the solid electron beam with enough current at a given $\alpha$ actually interacts with the cavity modes to produce the microwave output. Lower efficiencies at higher currents have been seen previously in Russian gyrotron experiments [Gin79].

## 4.4 Bragg Resonator Results.

The Bragg Resonator results (Cho91) for the gyro-BWO with the 24 hole apertured-mask anode are similar to those obtained in the gyro-BWO experiments conducted above with the smooth tube. That is, the powers obtained were similar (hundreds of kilowatts to 1 MW), and the microwave signals were also the same. The major difference is that the Bragg Resonator results were not always reproducable in that the signal would appear on some shots, but not on others for similar parameters. Typically when the low frequency gyro-BWO signal was reduced, the upper frequency interactions signal would increase in relative power. This suggests that the Bragg Resonator could be used in suppressing the low frequency gyro-BWO interactions by tuning the parameters to the upper frequency interaction that is enhanced by the Bragg Resonator. A flourescent light experiment to identify the radiation pattern was performed by Jin Choi [Cho91] which verified the low frequency, low magnetic field interaction was the $TE_{11}$ mode.

# CHAPTER V

# CONCLUSIONS

The Gyro-BWO is a desirable mechanism for generating long-pulse, high-power microwaves when using intense electron beams with large energy spreads. The reason for this is that the gyro-BWO interaction is relatively insensitive to beam velocity spreads and beam voltage fluctuations (as opposed to CARM devices). Previous gyro-BWO experiments have been very few, and have been conducted with low current ( < 10 amps), low voltage ( < 100 kV) electron beams, and have provided ~10 kW at efficiencies of ~15 %. Exploration of many aspects of the gyro-BWO still remain, including the effects of high current and high voltage electron beams on the efficiency and microwave power output.

In this thesis, experimental investigations of high current gyro-BWOs have been conducted for a solid beam which provided 1 -2 kA of electron beam current, and for an annular beam which provided 150 - 300 amps of electron beam current. A Vlasov-type antenna was employed to extract the microwave signal at the diode (upstream) end of the experiment. A waveguide detection system along with low-pass filters provided limited frequency ranges used to measure the frequency of the generated microwave signal. A calorimeter was used at the opposite (downstream) end of the experiment to give a rough output power comparison to the diode detectors on the waveguide detection system.

The solid beam provided extracted powers of 300 - 800 kW. When accounting for the efficiency of the Vlasov-antenna, the gyro-BWO device generates ~ 3 - 8 MW of power and has an efficiency of ~ 1 - 2 %. The greatest extracted powers were detected at parameters of: beam voltage = 700 - 750 kV, beam current = 1000 - 1500 amps, and

104

magnetic fields of 5.0 - 5.5 kG. Pulselengths of the microwave signals were 300 - 600 ns, and remained in resonance for the length of the voltage pulse. The frequency range of the highest powers was 4.7 - 5.3 GHz. The frequency was shown to be less than $F_c/\gamma$, was magnetically tunable over the range of 4.6 - 6 ± 0.5 GHz, and the frequency increased as the magnetic field increased, proving the existence of the backward-wave. Based on the frequency range and magnetic tunability, the interaction was determined to be the $TE_{11}$ fundamental mode backward-wave interaction. Microwave power output from the solid beam is approximately 300 - 800 times more than for previous low current gyro-BWO experiments, but at about one-tenth the efficiency.

The annular electron beam provided extracted microwave powers of 10 - 300 kW, depending on the beam voltage. High voltages (~ 850 - 900 kV) gave extracted powers of ~ 100 - 300 kW (efficiencies of ~1 - 2 % for the device) but for relatively short pulselengths (40 - 100 ns), due to the high voltage resonance condition detuning as the voltage dropped. The maximum extracted power (300 kW) occured at parameters of: beam voltage = 850 kV, beam current = 200 amps, and magnetic field of 6.4 kG. Lower voltages (600 - 700 kV) provided extracted powers of 10 - 80 kW (device efficiencies of 0.1 - 1 %) with pulselengths of 200 - 630 ns depending on the operating parameters. The reason for lower power for the low voltage (650 kV) interactions is believed to be reduced electron perpendicular energy (that is, the electrons have a lower $\alpha$). The maximum extracted power (80 kW) and maximum pulselength (630 ns) of the low voltage interaction occurred at parameters of: beam voltage = 650 kV, beam current = 200 amps, and magnetic field = 5.0 kG. The frequency of the maximum extracted power for both the high voltage (850 kV) and low voltage (650 kV) interactions was experimentally observed in the range of 4.6 - 6 GHz. The microwave signal was shown to be magnetically tunable over the range of 4.6 - 6 GHz, and, as for the solid beam above, was determined to be the the $TE_{11}$ fundamental mode backward-wave interaction at a frequency less than $F_c/\gamma$. In general, the annular beam provided less power than the

solid beam, but at approximately the same efficiencies. Microwave power output from the gyro-BWO device for the annular beam is about 10 - 80 times that of previous experiments, but only about one-tenth the efficiency.

Future work based on the experimental results presented here would be to use a high current annular beam that provides about 1 - 2 kA of electron beam current as did the solid beam. The microwave power output from this type of annular beam may be greater than that of the 150 - 300 A annular beam used in the above experiments, and may also have a greater efficiency than that of both the solid and annular beams mentioned above. Other work might include investigation of the high harmonic and mode competition in the gyro-BWO in an effort to increase the frequency output of the device at relatively low magnetic fields, as well as work on coupling out the generated power from the gyro-BWO by using several optimized Vlasov-antennas located at the diode end of the experiment.

**APPENDICES**

## APPENDIX A

## CYLINDRICAL VACUUM WAVEGUIDE ELECTROMAGNETIC FIELDS DERIVATION

The following derivation follows that of Harrington [Har61].

Beginning with the Helmholtz wave equation,

$$\nabla^2 \Psi + k^2 \Psi = 0 \tag{A.1}$$

where $\Psi$ is a scalar and $k$ is the wavevector given by,

$$k = \frac{2\pi}{\lambda} \tag{A.2}$$

The solution can be found by the method of separation of variables, by letting

$$\Psi = R(r)\Theta(\theta)Z(z) \tag{A.3}$$

Substituting (A.3) into the expanded form of the Helmholtz equation for

cylindrical coordinates,

$$\frac{1}{r}\frac{\partial}{\partial r}\left( r\frac{\partial \Psi}{\partial r} \right) + \frac{1}{r^2}\frac{\partial^2 \Psi}{\partial \theta^2} + \frac{\partial^2 \Psi}{\partial z^2} + k^2 \Psi = 0 \tag{A.4}$$

and dividing by $\Psi$ gives,

$$\frac{1}{rR}\frac{\partial}{\partial r}\left( r\frac{\partial R}{\partial r} \right) + \frac{1}{r^2 \Theta}\frac{\partial^2 \Theta}{\partial \theta^2} + \frac{1}{Z}\frac{\partial^2 Z}{\partial z^2} + k^2 = 0 \tag{A.5}$$

Since the first three terms are independent of the other two variables not contained

in the term, the terms must also be independent of their own variable to be constants and

add up to zero. Thus, beginning with the third term, let

$$\frac{1}{Z}\frac{\partial^2 Z}{\partial z^2} = -k_z^2 \tag{A.6}$$

Substituting (A.6) into (A.5),

$$\frac{1}{rR}\frac{\partial}{\partial r}\left( r\frac{\partial R}{\partial r} \right) + \frac{1}{r^2 \Theta}\frac{\partial^2 \Theta}{\partial \theta^2} + k^2 - k_z^2 = 0 \tag{A.7}$$

and multiply by $r^2$ gives,

$$\frac{r}{R}\frac{\partial}{\partial r}\left( r\frac{\partial R}{\partial r} \right) + \frac{1}{\Theta}\frac{\partial^2 \Theta}{\partial \theta^2} + r^2(k^2 - k_z^2) = 0 \tag{A.8}$$

Setting the second term in (A.8) equal to a constant,

$$\frac{1}{\Theta}\frac{\partial^2\Theta}{\partial\theta^2} = -m^2 \tag{A.9}$$

and substituting this into (A.8) gives three equations,

$$r\frac{\partial}{\partial r}\left(r\frac{\partial R}{\partial r}\right) + R\left(r^2(k^2 - k_z^2) - m^2\right) = 0 \tag{A.10a}$$

$$\frac{\partial^2\Theta}{\partial\theta^2} + m^2\Theta = 0 \tag{A.10b}$$

$$\frac{\partial^2 Z}{\partial z^2} + k_z^2 Z = 0 \tag{A.10c}$$

The solutions for the last two equations are harmonic functions, denoted by har(f(x)). The first equation is Bessel's equation of order m. Letting

$$k_r^2 = k^2 - k_z^2 \tag{A.11}$$

then solutions are

$$\Psi_{k_r,m,k_z} = B_m(k_r r)\text{har}(m\theta)\text{har}(k_z z) \tag{A.12a}$$

where $B_m(k_r r)$ is any of the general Bessel functions.

For the cylindrical waveguides, the Bessel function must be nonsingular at the origin, so only $J_m(k_r r)$ will solve this boundary condition. Thus,

$$\Psi_{k_r,m,k_z} = J_m(k_r r)\text{har}(m\theta)\text{har}(k_z z) \tag{A.12b}$$

$$\Psi_{k_r,m,k_z} = J_m(k_r r)e^{jm\theta}e^{jk_z z} \tag{A.12c}$$

Writing Maxwell's equations in their symmetric form (current and magnetic sources), and assuming solutions of the form $e^{j\omega t}$ gives:

For Electric Sources:

$$\nabla \times \mathbf{H} = j\omega\varepsilon\mathbf{E} + \mathbf{J}_e \tag{A.13a}$$

$$-\nabla \times \mathbf{E} = j\omega\mu\mathbf{H} \tag{A.13b}$$

$$\nabla \cdot \mathbf{E} = \frac{\rho_e}{\varepsilon} \tag{A.13c}$$

$$\mu\mathbf{H} = \nabla \times \mathbf{A} \tag{A.13d}$$

For Magnetic Sources:

$$\nabla \times \mathbf{H} = j\omega\varepsilon\mathbf{E} \tag{A.14a}$$

$$-\nabla \times \mathbf{E} = j\omega\mu\mathbf{H} + \mathbf{J}_m \qquad (A.14b)$$

$$\nabla \cdot \mathbf{H} = \frac{\rho_m}{\mu} \qquad (A.14c)$$

$$\varepsilon\mathbf{E} = -\nabla \times \mathbf{F} \qquad (A.14d)$$

where the subscripts 'e' and 'm' denote electric or magnetic parts, respectively, $\mathbf{A}$ is the magnetic vector potential, and $\mathbf{F}$ is the electric vector potential.

For the TE (transverse electric) case, the solution can be found by letting the electric vector potential $\mathbf{F}$ be in the z-direction, and the magnetic potential $\mathbf{A} = 0$. This gives,

$$\mathbf{F} = F\hat{z} = \Psi\hat{z} \qquad (A.15a)$$

$$\mathbf{A} = 0 \qquad (A.15b)$$

$$\varepsilon\mathbf{E} = -\nabla \times \mathbf{F} \qquad (A.15c)$$

$\mathbf{H}$ is just the superposition of the above magnetic and current sources, and applying eqns. (A.15(a-c)),

$$\mu\mathbf{H} = \nabla \times \mathbf{A} + \frac{1}{j\omega}(-\nabla \times \mathbf{E} - \mathbf{J}_m) \qquad (A.16a)$$

$$\mu\mathbf{H} = -\frac{j}{\omega}(-\nabla \times \left(\frac{-\nabla \times \mathbf{F}}{\varepsilon}\right) - \mathbf{J}_m) \qquad (A.16b)$$

and since the magnetic current is zero for TE modes, you have,

$$\mathbf{H} = -\frac{j}{\mu\varepsilon\omega}(\nabla \times \nabla \times \mathbf{F}) = -\frac{j}{\mu\varepsilon\omega}(\nabla(\nabla\cdot\mathbf{F}) - \nabla^2\mathbf{F}) \qquad (A.17)$$

Using the Lorentz Gauge condition of

$$\nabla \cdot \mathbf{F} + \mu\varepsilon\frac{\partial\phi'}{\partial t} = 0 \qquad (A.18)$$

where $\phi'$ is an arbitrary scalar potental, gives the standard wave equation,

$$\nabla^2\mathbf{F} - \frac{1}{c^2}\frac{\partial^2\mathbf{F}}{\partial t^2} = 0 \Rightarrow \nabla^2\mathbf{F} = -\frac{\omega^2}{c^2}\mathbf{F} \qquad (A.19)$$

Placing (A.19) into equation (A.17),

$$\mathbf{H} = -\frac{j}{\mu\varepsilon\omega}\left(\nabla(\nabla\cdot\mathbf{F}) - \frac{\omega^2}{c^2}\mathbf{F}\right) \qquad (A.20a)$$

$$\mathbf{H} = -j\omega\mathbf{F} - \frac{j}{\mu\varepsilon\omega}\nabla(\nabla\cdot\mathbf{F}) \qquad (A.20b)$$

$$H = -j\omega F + \frac{1}{j\mu\varepsilon\omega} \nabla(\nabla\cdot F) \qquad (A.20c)$$

Now expand $E$ and $H$. For cylindrical coordinates,

$$\nabla \times F = \hat{r}\left(\frac{1}{r}\frac{\partial F_z}{\partial\theta} - \frac{\partial F_\theta}{\partial z}\right) + \hat{\theta}\left(\frac{\partial F_r}{\partial z} - \frac{\partial F_z}{\partial r}\right) + \hat{z}\left(\frac{1}{r}\left(\frac{\partial(rF_\theta)}{\partial r} - \frac{\partial F_r}{\partial\theta}\right)\right) \qquad (A.21)$$

Using (A.15a) gives

$$\nabla \times F = \hat{r}\left(\frac{1}{r}\frac{\partial F_z}{\partial\theta}\right) - \hat{\theta}\left(\frac{\partial F_z}{\partial r}\right) \qquad (A.22)$$

which gives the electric field components,

$$\varepsilon E_r = -\frac{1}{r}\frac{\partial\Psi}{\partial\theta} \qquad (A.23a)$$

$$\varepsilon E_\theta = \frac{\partial\Psi}{\partial r} \qquad (A.23b)$$

$$\varepsilon E_z = 0 \qquad (A.23c)$$

Notice this shows that $E_z = 0$, which is the condition for the transverse electric (TE) waves.

Now expanding the $H$ field,

$$H = -j\omega F_z + \frac{1}{j\mu\varepsilon\omega} \nabla(\nabla\cdot F) \qquad (A.24a)$$

$$\nabla\cdot F = \nabla\cdot F_z \hat{z} = \frac{\partial F_z}{\partial z} = \frac{\partial\Psi}{\partial z} \qquad (A.24b)$$

In cylindrical coordinates,

$$\nabla\zeta = \frac{\partial\zeta}{\partial r}\hat{r} + \frac{1}{r}\frac{\partial\zeta}{\partial\theta}\hat{\theta} + \frac{\partial\zeta}{\partial z}\hat{z} \qquad (A.25)$$

so,

$$\nabla(\nabla\cdot F) = \left(\frac{\partial}{\partial r}\hat{r} + \frac{1}{r}\frac{\partial}{\partial\theta}\hat{\theta} + \frac{\partial}{\partial z}\hat{z}\right)\left(\frac{\partial\Psi}{\partial z}\right) \qquad (A.26a)$$

$$\nabla(\nabla\cdot F) = \frac{\partial^2\Psi}{\partial r\partial z}\hat{r} + \frac{1}{r}\frac{\partial^2\Psi}{\partial\theta\partial z}\hat{\theta} + \frac{\partial^2\Psi}{\partial z^2}\hat{z} \qquad (A.26b)$$

which gives the $H$ components,

$$H_r = \frac{1}{j\mu\varepsilon\omega}\frac{\partial^2\Psi}{\partial r\partial z} \qquad (A.27a)$$

$$H_\theta = \frac{1}{j\mu\varepsilon\omega}\frac{1}{r}\frac{\partial^2\Psi}{\partial\theta\partial z} \qquad (A.27b)$$

$$H_z = -j\omega\Psi + \frac{1}{j\mu\epsilon\omega}\frac{\partial^2\Psi}{\partial z^2} = -j\left(\omega + \frac{1}{\mu\epsilon\omega}\frac{\partial^2}{\partial z^2}\right)\Psi$$

$$= -j\left(\omega + \frac{c^2}{\omega}\frac{\partial^2}{\partial z^2}\right)\Psi = -\frac{j}{\omega}\left(\omega^2 + c^2\frac{\partial^2}{\partial z^2}\right)\Psi = -\frac{jc^2}{\omega}\left(\frac{\omega^2}{c^2} + \frac{\partial^2}{\partial z^2}\right)\Psi$$

$$= -\frac{jc^2}{\omega}\left(k^2 + \frac{\partial^2}{\partial z^2}\right)\Psi \qquad (A.27c)$$

where the following relations for a plane wave in vacuum have been used,

$$\mu\epsilon = \frac{1}{c^2}, \quad k^2 = \frac{\omega^2}{c^2} \qquad (A.28)$$

Substituting $\Psi_{k_r,m,k_z}$ from equation (A12.b) into equations (A.23) and (A.27) gives,

$$E_r = -\frac{1}{\epsilon r}\frac{\partial(J_m(k_r r)e^{jm\theta}e^{jk_z z})}{\partial\theta} = -\frac{jm}{\epsilon r}J_m(k_r r)e^{jm\theta}e^{jk_z z} \qquad (A.29a)$$

$$E_\theta = \frac{1}{\epsilon}\frac{\partial(J_m(k_r r)e^{jm\theta}e^{jk_z z})}{\partial r} = \frac{k_r}{\epsilon}J_m'(k_r r)e^{jm\theta}e^{jk_z z} \qquad (A.29b)$$

$$E_z = 0 \qquad (A.29c)$$

$$H_r = \frac{1}{j\mu\epsilon\omega}\frac{\partial^2(J_m(k_r r)e^{jm\theta}e^{jk_z z})}{\partial r\partial z} = \frac{k_r k_z}{\omega\mu\epsilon}J_m'(k_r r)e^{jm\theta}e^{jk_z z} \qquad (A.29d)$$

$$H_\theta = \frac{1}{j\mu\epsilon\omega}\frac{1}{r}\frac{\partial^2(J_m(k_r r)e^{jm\theta}e^{jk_z z})}{\partial\theta\partial z} = -\frac{mk_z}{j\omega\mu\epsilon r}J_m(k_r r)e^{jm\theta}e^{jk_z z} \qquad (A.29e)$$

$$H_z = -\frac{jc^2}{\omega}\left(k^2 + \frac{\partial^2}{\partial z^2}\right)(J_m(k_r r)e^{jm\theta}e^{jk_z z}) = -\frac{jc^2}{\omega}k_r^2 J_m(k_r r)e^{jm\theta}e^{jk_z z} \qquad (A.29f)$$

Noting that

$$J_m'(k_r r) = \frac{\partial J_m(k_r r)}{\partial r} \qquad (A.30)$$

Using the amplitude constant of

$$B_{z0} = -\frac{jk_r^2}{\epsilon\omega} \qquad (A.31)$$

gives the following form of the field components which are comparable to [Ram65]

$$E_r = \frac{\omega m}{k_r^2 r}B_{z0}J_m(k_r r)e^{jm\theta}e^{jk_z z} \qquad (A.32a)$$

$$E_\theta = \frac{j\omega}{k_r} B_{z0} J_m'(k_r r)e^{jm\theta}e^{jk_z z} \tag{A.32b}$$

$$E_z = 0 \tag{A.32c}$$

$$B_r = \frac{jk_z}{k_r} B_{z0}J_m'(k_r r)e^{jm\theta}e^{jk_z z} \tag{A.32d}$$

$$B_\theta = -\frac{mk_z}{k_r^2 r} B_{z0} J_m(k_r r)e^{jm\theta}e^{jk_z z} \tag{A.32e}$$

$$B_z = B_{z0} J_m(k_r r)e^{jm\theta}e^{jk_z z} \tag{A.32f}$$

The Transverse Magnetic (TM) fields can similarly be derived by using $\mathbf{F} = 0$. The TM fields are listed in [Har61] and since they are not a prominent feature of the gyro-BWO, they are not presented here.

By applying the boundary condition for a TE wave of $E_\theta = 0$ at the radius of the cavity , r=a, one gets,

$$E_\theta = \frac{j\omega}{k_r} B_{z0} J_m'(k_r a)e^{jm\theta}e^{jk_z z} = 0 \tag{A.33}$$

$$J_m'(k_r a) = 0 \tag{A.34}$$

which implies that

$$k_r = \frac{\chi_{mn}'}{a} \tag{A.35}$$

where $\chi_{mn}'$ are the zeros of $J_m'(x)$.

Knowing that the dispersion relation for a plane wave in vacuum is

$$\omega^2 = k^2 c^2 \tag{A.36}$$

one can then derive the dispersion relation for cylindrical waveguides by placing equation (A.11)

$$k^2 = k_r^2 + k_z^2 \tag{A.37}$$

into (A.36)

$$\omega^2 = (k_r^2 + k_z^2) c^2$$

$$\omega^2 - k_r^2 c^2 - k_z^2 c^2 = 0 \tag{A.38}$$

The cutoff wavenumber occurs when the mode propagation constant goes to zero, $k_z \to 0$, so,

$$k_c = \frac{\chi'_{mn}}{a} \tag{A.39}$$

From (A.39), one can get the cutoff wavelength,

$$\lambda_c = \frac{2\pi}{k_c} = \frac{2\pi a}{\chi'_{mn}} \tag{A.40}$$

and the cutoff frequency,

$$f_c = \frac{c}{\lambda_c} = \frac{c}{2\pi a} \chi'_{mn} \tag{A.41}$$

The phase velocity can also be found,

$$v_p = \frac{\omega}{k_z} = \frac{\omega}{\sqrt{k^2 - k_c^2}} = \frac{c}{\sqrt{1 - \frac{k_c^2}{k^2}}} \tag{A.42}$$

With,

$$\frac{k_c}{k} = \frac{\left(\frac{2\pi}{\lambda_c}\right)}{\left(\frac{2\pi}{\lambda}\right)} = \frac{\lambda}{\lambda_c} = \frac{\left(\frac{c}{f}\right)}{\left(\frac{c}{f_c}\right)} = \frac{f_c}{f} \tag{A.43}$$

then the phase velocity becomes

$$v_p = \frac{c}{\sqrt{1 - \left(\frac{f_c}{f}\right)^2}} \tag{A.44}$$

The guide wavelength is defined as the distance in which the phase of E is increased by $2\pi$, that is, $k_z \lambda_g = 2\pi$. This gives,

$$\lambda_g = \frac{2\pi}{k_z} = \frac{2\pi v_p}{\omega} = \frac{2\pi c}{\omega \sqrt{1 - \left(\frac{f_c}{f}\right)^2}} = \frac{\lambda}{\sqrt{1 - \left(\frac{f_c}{f}\right)^2}} \tag{A.45}$$

The waveguide, or wave, impedance in the z direction for the TE modes can be found from

$$Z_z = Z_{TE} = \left| \frac{E_r}{H_\theta} \right| = \frac{\omega\mu}{k_z} = \frac{377\ \Omega}{\sqrt{1 - \left(\dfrac{f_c}{f}\right)^2}} \qquad (A.46)$$

where the free space value of the intrinsic impedance $\eta = (\mu/\varepsilon)^{-1/2} \cong 377\ \Omega$ has been used.

## APPENDIX B

## CONVENTIONAL BWO DISPERSION RELATION

For convenience, the conventional BWO dispersion relation is listed here. The derivation can be found in [Lei86]. As mentioned in Chapter I, the BWO is a slow-wave device and takes advantage of the axial bunching of the electrons to transfer the electron kinetic energy to the electromagnetic waves, which is similar to the Weibel mechanism described in Chapter II. In order to accomplish the axial bunching, a strong uniform axial magnetic field is used to guide the electrons and force the azimuthal rotation of the beam to go to zero (that is, $\alpha \sim 0$). When this occurs, the electrons then interact with the slow TM (Transverse Magnetic) waves of the slow-wave structure. Figure B.1 depicts a typical slow-wave structure used as the interaction cavity in the BWO experiments.
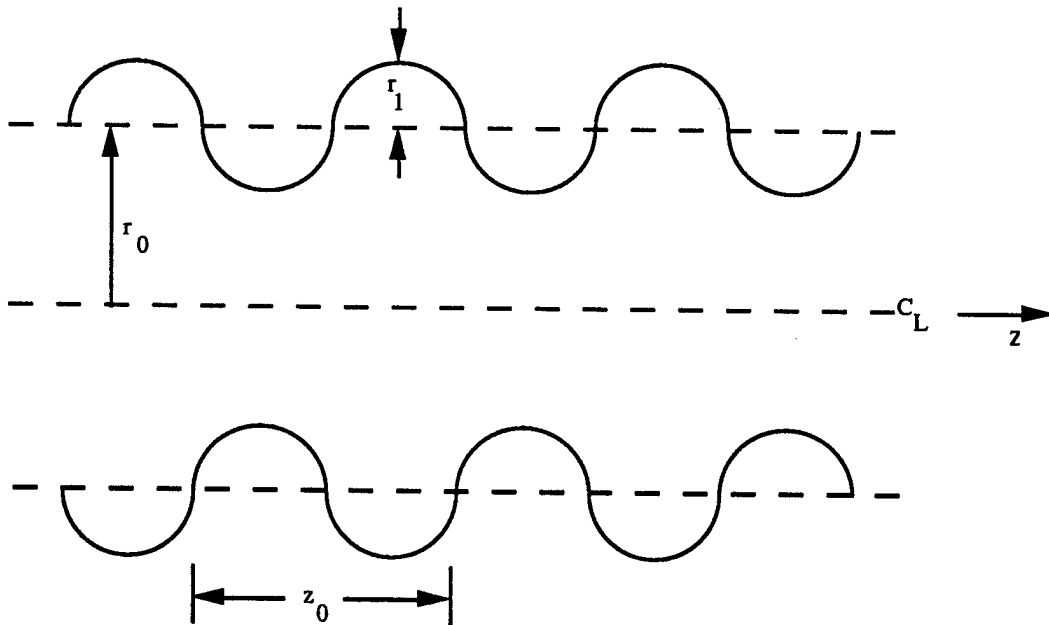
**Figure B.1.** **The slow-wave structure typically employed in conventional BWO devices.**

The slow-wave structure is a cylindrical waveguide with a sinusoidal varying wall radius,

$$r_w(z) = r_0 + r_1 \sin(h_o z) \tag{B.1}$$

where $h_0 = 2\pi / z_0$, and $z_0$ is the periodicity of the ripple.

Floquet's theorem of periodicity,

$$E_0 e^{(i\omega t)} = E_0 e^{(i(\omega + 2\pi)t)} \tag{B.2}$$

shows that if a waveguide is perturbed with a period $z_0$, then $\omega$ will also be periodic in k

(k being the wavenumber) such that

$$\omega(k + nh_0) = \omega(k) \tag{B.3}$$

where n is any integer.

Floquet's Theorem is then used to expand the electric and magnetic fields, and in

a similar derivation for the ECM [Fli86] with a thin annular beam, the conventional BWO

dispersion relation for a $TM_{0m}$ is given by

$$D_{mn} = \frac{\omega^2 - k_n k_c c^2}{\Gamma_n^2 c^2} \left[ I_{mn}^J - \varepsilon \frac{\Gamma_n c}{\omega - k_n v_b}^2 J_0(\Gamma_n r_b) \left[ I_{mn}^J N_0(\Gamma_n r_b - I_{mn}^N J_0(\Gamma_n r_b)) \right] \right] \tag{B.4}$$

where

$$I_{mn}^J = \frac{1}{2\pi} \int_{-\pi}^{\pi} e^{[i(n-m)u]} J_0[\Gamma_n r_b(1 + \zeta \sin u) du \tag{B.5}$$

$$I_{mn}^N = \frac{1}{2\pi} \int_{-\pi}^{\pi} e^{[i(n-m)u]} N_0[\Gamma_n r_b(1 + \zeta \sin u) du \tag{B.6}$$

and

$$\Gamma_n^2 = \frac{\omega^2}{c^2} - k_n^2 \tag{B.7}$$

$$\zeta = \frac{r_1}{r_0} \tag{B.8}$$

$$k_n = k_0 + nh_0 \tag{B.9}$$

$$k_c = \frac{\mu_{0m}}{r_w} \tag{B.10}$$

with $k_0$ limited to lie between 0 and $h_0$.

$\varepsilon$ is the beam strength given by

$$\varepsilon = \frac{\pi I_b}{\beta_b \gamma_b^3 I_A} \tag{B.11}$$

$$\beta_b = \frac{v_b}{c} \tag{B.12}$$

$$\gamma_b = \frac{1}{\sqrt{1 - \beta_b^2}} \tag{B.12}$$

where $v_b$ is the beam velocity, $I_b$ is the beam current, $J_0$ is the Bessel function of the first kind, $N_0$ is the Bessel function of the second kind, and the Alfven current is $I_A = 17.1$ kA.

One can notice that the dispersion relation given by equation (B.4) must be solved numerically, and is much more complicated than the dispersion relation for the gyro-BWO given in equation (2.18). Approximate decoupled ($\varepsilon = 0$) dispersion relations for the waveguide modes can be found using equation (B.3), and the approximate intersections with the dispersion relation of the slow-wave mode of the electron beam can be estimated. See [Lei86].

# APPENDIX C

## TEKTRONIX DSA 602 / IBM DATA TRANSFER PROGRAM

The following BASIC program enables the Tektronix DSA 602 oscilloscope to converse with an IBM computer via the GPIB (IEEE-488) convention. The program is stored on both the IBM hard disk (under the DSA directory) and a backup data disk as 'TRA2.BAS'. Lines 10 - 130 set up a dimensioned variable to receive the data from the scope. Lines 150 - 220 configure the IEEE-488 board (hardware located in the computer, the board is a MetraByte MBC-488, available from MetraByte Corp., 440 Myles Standish Blvd., Taunton, MA, 02780, Phone: (508) 880 - 3000). More information on configuring the board is available in the "DV488 User's Guide", also available from MetraByte. Lines 222 - 590 ask for and receive the data from the DSA 602, and store the information onto the hard disk of the IBM. Lines 600 - 680 are a basic error checking routine, based on a similar routine described in the "DV488 User's Guide". Lines 3000 - 3500 displays the current trace (in actuality the displayed trace is a previously stored trace) on the DSA 602 screen that is being transferred from the DSA 602 scope. Line 5000 is the statement necessary to enable the MBC-488 board to send commands to the DSA 602 scope. These commands are DSA 602 standard commands, available from the DSA 602 programmer's manual. Lines 6000 - 6500 retrieve the actual data of the current trace displayed on the DSA 602 scope. Lines 7000 - 7100 ask for the beginning and ending storage numbers of the stored traces on the DSA 602 scope, so that several traces can be sequentially received with a single run of the program. Lines 8000 - 9100 are a 'space checking' routine, which is necessary when writing files to the IBM (to follow the MS-DOS format). The stored labels for each particular stored trace can have 10 alphanumeric characters, some of which are incompatable with MS-DOS. In order to be successful in conversing with the DSA 602 scope, two programs must be located in the DSA directory of the IBM hard disk: 1) VI.SYS and 2) DV488.SYS, which are available on a disk that accompanies the DV488 User's Guide. The location of these two

programs on the IBM hard disk may be changed by changing the configuration file
(config.sys) on the IBM hard disk. To run the BASIC program, type BASICA
TRA2.BAS at the > prompt, and type in the appropriate begin/end store numbers
information that the program prompts for at the beginning of its run.

```
10 DIM XW(15)
20 FOR I=1 TO 15:XW(I)=0: NEXT I
70 DIM DV%(16500)
100 CLS:KEY OFF
130 LOCATE 1,1
135 GOSUB 7000
150 OPEN "$DV488" FOR OUTPUT AS #1
160 PRINT #1, "BUFFERCLEAR"
170 OPEN "$DV488" FOR INPUT AS #2
180 ON ERROR GOTO 600
190 PRINT #1, "SYSCON MAD1=3 CIC1=1 BA1=&H300"
200 PRINT #1, "REMOTE 1"
210 A%=100
220 PRINT #1, "TIMEOUT", A%
222 CMD$="PAT OFF":GOSUB 5000
225 CMD$=STP3$:GOSUB 5000
226 LABEL$="":FIL$=""
227 CMD$="WFM? LAB":GOSUB 5000
228 PRINT #1, "ENTER 1 $"
229 INPUT #2, FIL$: GOSUB 8000
232 CMD$="WFM? LAB,DATE,TIME":GOSUB 5000
235 PRINT #1, "ENTER 1 $"
240 FOR I=1 TO 3: INPUT #2,LABEL$:PRINT #3, LABEL$:NEXT I
250 CMD$="WFM? NR.PT":GOSUB 5000
255 PRINT #1, "ENTER 1 $":INPUT #2, N$:NPTS=VAL(N$)
260 CMD$="ABB ON":GOSUB 5000
270 CMD$="PAT ON":GOSUB 5000
280 CMD$="WFM?":GOSUB 5000
290 PRINT #1, "ENTER 1 $"
300 FOR I=1 TO 4
310 INPUT #2, XINC$:PRINT #3,XINC$
320 INPUT #2, XINC$:PRINT #3,XINC$
330 NEXT I
400 GOSUB 3000
580 CLOSE #3
590 GOSUB 9000:GOTO 222
600 IF ERR<>68 AND (ERR<>57) THEN PRINT "BASIC ERROR #";ERR;"
        IN LINE";ERL
610 IF ERR<>68 AND (ERR<>57) THEN STOP
620 INPUT #2, E$
630 PRINT "$DV488 DRIVER RETURNED ERROR NUMBER- ", E$
640 INPUT #2, E$
650 PRINT E$
660 INPUT #2,E$
```

```
670 PRINT E$
680 END
3000 'SHOW TRACES
3005 XK=NPTS/512
3010 CMD$=STP7$:GOSUB 5000
3015 FOR III = 1 TO 1000: NEXT III
3020 ALPH%=0
3030 ADJ$="ADJ1 HMA:":XKP$=STR$(XK):HPO$=",HPO:"
3040 FOR II=1 TO XK
3050 EPT$=STR$((II-1)*512)
3060 ADJ1$=ADJ$+XKP$+HPO$+EPT$
3070 CMD$=ADJ1$:GOSUB 5000
3080 A%=300:PRINT #1, "TIMEOUT" ,A%
3090 GOSUB 6000
3100 ALPH%=ALPH%+1
3110 NEXT II
3180 FOR I=1 TO NPTS:PRINT #3, DV%(I): NEXT I
3500 RETURN
5000 PRINT #1,"OUTPUT 1 $ +", CMD$:RETURN
6000 CMD$="OUTPUT TRA1":GOSUB 5000
6120 CMD$="ENC WAV:ASC":GOSUB 5000
6130 CMD$="PAT OFF":GOSUB 5000
6135 A%=300:PRINT #1, "TIMEOUT", A%
6140 CMD$="CURV?":GOSUB 5000
6150 ISTAR%=ALPH%*512+1
6160 ISTOP%=ISTAR%+511
6165 A%=300:PRINT #1, "TIMEOUT", A%
6167 PRINT #1, "ENTER 1 $"
6170 FOR I=ISTAR% TO ISTOP%
6190 INPUT #2, ABC$:DV%(I)=VAL(ABC$)
6200 NEXT I
6500 RETURN
7000 PRINT "STO NUMBER BEGIN (A NUMERIC VALUE)": INPUT STP$
7010 PRINT "STO NUMBER END ":INPUT STPE$
7020 STP2$="OUTPUT STO":STP3$=STP2$+STP$
7030 STP4$="TRA1 DESC:'STO":STP5$=STP4$+STP$
7040 STP6$="'":STP7$=STP5$+STP6$
7050 COLOR 4,1,0: PRINT "RAPPIN' WITH THE SCOPE....."
7100 RETURN
8000 'SPACE CHECKING ROUTINE (ASSUMING LABEL <> "")
8010 XY=LEN(FIL$)
8011 IF XY > 8 THEN GOSUB 8500
8020 IF FIL$="" THEN PRINT "NO LABEL SAVED, PROGRAM
     ABORT":END
8030 FOR JJ = 1 TO XY
8040 IF MID$(FIL$,JJ,1) <> " " GOTO 8060
8050 XW(JJ)=1
8060 NEXT JJ
8070 TE$=""
8080 FOR JJ=1 TO XY
8090 IF XW(JJ)=0 THEN TE$=TE$+MID$(FIL$,JJ,1)
8100 NEXT JJ
8110 IF TE$ <> "" THEN FIL$=TE$
8115 FOR I = 1 TO 15: XW(I) = 0: NEXT I
```

```
8120 OPEN "O", #3, FIL$
8199 RETURN
8500 'MAKING LABEL = 8 LETTERS.
8510 FIL$=RIGHT$(FIL$,8)
8515 XY=8
8520 RETURN
8600 'SPACE CHECKING ROUTINE (ASSUMING LABEL <> "")
8610 XZ=LEN(FIL$)
8620 IF STP$="" THEN PRINT "NO LABEL SAVED, PROGRAM
     ABORT":END
8630 FOR JJ = 1 TO XZ
8640 IF MID$(STP$,JJ,1) <> " " GOTO 8660
8650 XW(JJ)=1
8660 NEXT JJ
8670 TE$=""
8680 FOR JJ=1 TO XZ
8690 IF XW(JJ)=0 THEN TE$=TE$+MID$(STP$,JJ,1)
8700 NEXT JJ
8710 IF TE$ <> "" THEN STP$=TE$
8715 FOR I = 1 TO 15: XW(I) = 0: NEXT I
8799 RETURN
9000 'GET NEXT STORED WAVEFORM NUMBER
9010 HH%=VAL(STP$)
9020 HH%=HH%+1
9030 IF HH%>VAL(STPE$) THEN CLS:PRINT"ALL DONE":END
9040 STP$=STR$(HH%)
9045 GOSUB 8600
9050 STP3$=STP2$+STP$
9060 STP5$=STP4$+STP$
9070 STP7$=STP5$+STP6$
9100 RETURN
```

## APPENDIX D

## DIODE CLOSURE ANALYSIS USING MICROSOFT EXCEL 2.2

The following describes the diode closure analysis set up using Microsoft Excel 2.2

[Mic89] on a Macintosh computer. Shot M1876 is used as a base example. The

workspace that interconnects the worksheet and charts is m1876.work. The worksheet is

radialclosure.m1876txl. The diode/total model comparison chart shown in Figure 3.20 is

1/sqrt(p)diode.1876t. The anode/planar model chart (see Figure 3.13b) is

AkAnode.m1876t. The wall/radial chart (see Figure 3.13c) is 1/sqrt(p)wall.m1876t.

Double click on m1876.work (the workspace), and click 'no' for the 'update references'

request. The worksheet radialclosure.m1876txl is outlined below, and the charts are

automatically updated as changes to the worksheet are made. For notation purposes, R1C1

refers to Row 1, Column 1 (one of XL 2.2 row and column notations). The outline for the

diode closure worksheet is:

| | | |
|---|---|---|
| (1) | R1C4 | Closure Veloity (cm/$\mu$s) |
| (2) | R2C4 | Effective Plasma Radius (cm) |
| (3) | R2C7 | AK-Gap (cm) |
| (4) | R1C7 | Constant from radial C-L (equation 3.9) |
| (5) | R2C10 | Constant from planar C-L (equation 3.4) |
| (6) | R5C1 - R105C1 | Time (ns) |
| (7) | R5C2 - R105C2 | Voltage (kV, measured) |
| (8) | R5C3 - R105C3 | Time (ns) |
| (9) | R5C4 - R105C4 | Diode Current (kA, measured) |
| (10) | R5C5 - R105C5 | Measured Diode Perveance (equation 3.6) |
| (11) | R5C6 - R105C6 | Measured Diode 1/sqrt(P) |
| (12) | R5C7 - R105C7 | Time - [user supplied quantity] to equal 50 ns |
| (13) | R5C9 - R105C9 | y = ln(d/velocity*time*0.0001) (in equation 3.10) |
| (14) | R5C10 - R105C10 | beta (eqation 3.10) |
| (15) | R5C11 - R105C11 | Radial theory 1/sqrt(P) (from equation 3.9) |
| (16) | R5C12 - R105C12 | Measured 1/sqrt(P) (from 11 above) |
| (17) | R5C13 - R105C13 | Planar theory 1/sqrt(P) (from equation 3.5) |
| (18) | R5C14 - R105C14 | Theory Radial Perveance (equation 3.9) |
| (19) | R5C15 - R105C15 | Theory Planar Perveance (equation 3.5) |
| (20) | R5C16 - R105C16 | Theory Total Perveance (equation 3.11) |
| (21) | R5C17 - R105C17 | Time (ns) from R5C7 - R105C7 |
| (22) | R5C18 - R105C18 | Total 1/sqrt(P) from R5C16 - R105C16 (eqn. 3.11) |
| (23) | R5C19 - R105C19 | Measured Diode 1/sqrt(P) from R5C12 - R105C12 |
| (24) | R5C20 - R105C20 | Time (ns) from R5C7 - R105C7 |
| (25) | R5C21 - R105C21 | Theory AK-Gap (d) in cm (equation 3.3) |
| (26) | R5C22 - R105C22 | Measured Planar AK-Gap (d) in cm (equation 3.7) |

| | |
|---|---|
| (27) R108C1 - R208C1 | Time (ns) |
| (28) R108C2 - R208C2 | Voltage (kV, measured) |
| (29) R108C3 - R208C3 | Time (ns) |
| (30) R108C4 - R208C4 | Anode Current (kA, measured) |
| (31) R108C5 - R208C5 | Measured Anode Perveance (equation 3.6) |
| (32) R108C6 - R208C6 | Measured Anode 1/sqrt(P) |
| (33) R108C7 - R208C7 | Time - [user supplied quantity] to equal 50 ns |
| (34) R108C9 - R208C9 | $y = \ln(d/velocity*time*0.0001)$ (in equation 3.10) |
| (35) R108C10 - R208C10 | beta (eqation 3.10) |
| (36) R108C11 - R208C11 | Radial theory 1/sqrt(P) (from equation 3.9) |
| (37) R108C12 - R208C12 | Measured 1/sqrt(P) (from 32 above) |
| (38) R108C13 - R208C13 | Planar theory 1/sqrt(P) (from equation 3.5) |
| (39) R108C14 - R208C14 | Theory Radial Perveance (equation 3.9) |
| (40) R108C15 - R208C15 | Theory Planar Perveance (equation 3.5) |
| (41) R108C16 - R208C16 | Theory Total Perveance (equation 3.11) |
| (42) R108C17 - R208C17 | Time (ns) from R108C7 - R208C7 |
| (43) R108C18 - R208C18 | Total 1/sqrt(P) from R108C16 - R208C16 (eqn.( 3.11) |
| (44) R108C19 - R208C19 | Measured Anode 1/sqrt(P) from R108C12 - R20(8C12 |
| (45) R108C20 - R208C20 | Time (ns) from R108C7 - R208C7 |
| (46) R108C21 - R208C21 | Theory AK-Gap (d) in cm (equation 3.3) |
| (47) R108C22 - R208C22 | Measured Planar AK-Gap (d) in cm (equation 3.7) |
| (48) R215C1 - R315C1 | Time (ns) |
| (49) R215C2 - R315C2 | Voltage (kV, measured) |
| (50) R215C3 - R315C3 | Time (ns) |
| (51) R215C4 - R315C4 | Wall Current (kA, measured) |
| (52) R215C5 - R315C5 | Measured Wall Perveance (equation 3.6) |
| (53) R215C6 - R315C6 | Measured Wall 1/sqrt(P) |
| (54) R215C7 - R315C7 | Time - [user supplied quantity] to equal 50 ns |
| (55) R215C9 - R315C9 | $y = \ln(d/velocity*time*0.0001)$ (in equation 3.10) |
| (56) R215C10 - R315C10 | beta (eqation 3.10) |
| (57) R215C11 - R315C11 | Radial theory 1/sqrt(P) (from equation 3.9) |
| (58) R215C12 - R315C12 | Measured 1/sqrt(P) (from 53 above) |
| (59) R215C13 - R315C13 | Planar theory 1/sqrt(P) (from equation 3.5) |
| (60) R215C14 - R315C14 | Theory Radial Perveance (equation 3.9) |
| (61) R215C15 - R315C15 | Theory Planar Perveance (equation 3.5) |
| (62) R215C16 - R315C16 | Theory Total Perveance (equation 3.11) |
| (63) R215C17 - R315C17 | Time (ns) from R215C7 - R315C7 |
| (64) R215C18 - R315C18 | Total 1/sqrt(P) from R215C11 - R315C11 (eqn. 3.9) |
| (65) R215C19 - R315C19 | Measured Wall 1/sqrt(P) from R215C12 - R315C12 |
| (66) R215C20 - R315C20 | Time (ns) from R215C7 - R315C7 |
| (67) R215C21 - R315C21 | Theory AK-Gap (d) in cm (equation 3.3) |
| (68) R215C22 - R315C22 | Measured Planar AK-Gap (d) in cm (equation 3.7) |

Lines (1) - (3) in the above list are the variables that can be changed by the user to obtain the 'best fit' described in chapter III. Lines (6) - (26) are the diode/total model set up, and the 1/sqrt(P)diode.1876t chart is automatically updated from lines (21) - (23) in the above list. Lines (27) - (47) are the anode/planar model set up, and the AkAnode.m1876t chart is automatically updated from lines (45) - (47) in the above list. Lines (48) - (68) are

the wall/radial model set up, and the 1/sqrt(p)wall.m1876t chart is automatically updated from lines (63) - (65) from the above list. The measured voltage, diode current, and anode current (along with the corresponding time (in ns) ) must be provided by the user. The set up uses 100 data points from the measured voltage, diode current, and anode current. The measured voltage data points must be pasted in lines (7), (28), and (49) referenced in the above list. The corresponding voltage time is pasted in lines (6), (27), and (48). The measured diode current is placed in (9) referenced in the above list, with the corresponding time in (8). The measured anode current is pasted in (29) referenced in the above list, with the corresponding time in (28). The measured wall current is automatically computed from the given diode and anode currents in (9) and (29). Line (12) in the above list must also be manipulated by the user, so that the time comes out to 50 (strictly arbitrary) ns (use the 'fill down' command of XL 2.2 to save time). This is done since equation (3.10) would have a divide by zero error if the time was actually zero.

126

# APPENDIX E
# VLASOV-ANTENNA ADAPTER FLANGE DESIGN

The following figures show the S-Band (WR-284) Vlasov-antenna flange dimensions. Figure E.1 shows the 'front side' of the adapter flange, which mates with a standard MDC 6" nominal OD flange. Figure E.2 shows the 'back side' of the adapter flange, which mates with a standard S-Band (WR-284) circular flange (UG-53/U). The center of the adapter flange is drilled out to match a standard S-Band (WR-284) rectangular waveguide. Figure E.3 shows the 'side view' of the adapter flange.
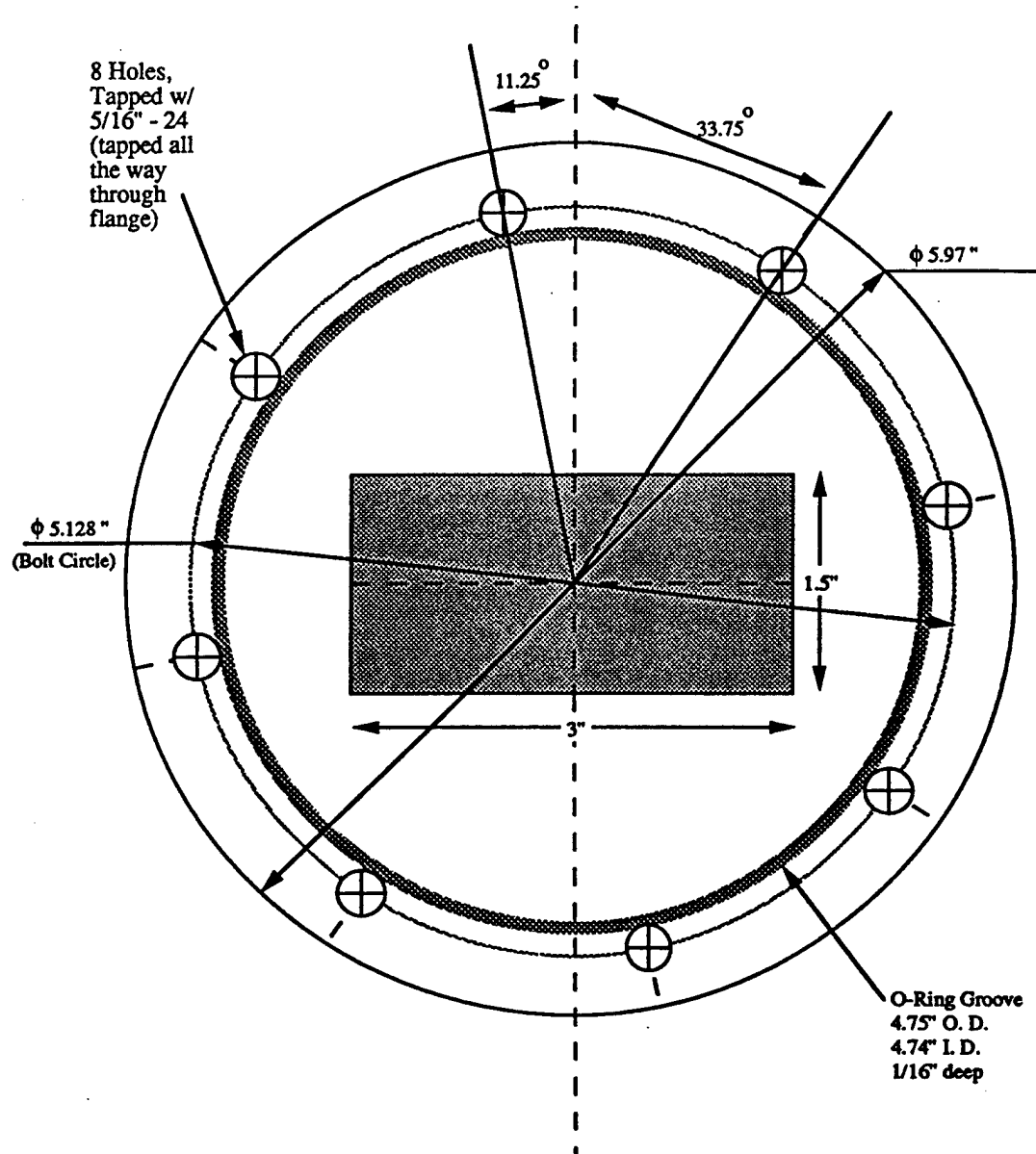
**Figure E.1.** The 'front side' of the Vlasov-antenna adapter flange.

**8 Holes,**
**Tapped w/**
**5/16" - 24**
**(tapped all**
**the way**
**through**
**flange)**

22.5°    22.5°

φ 5.97 "

φ 4.750 "
**(Bolt Circle)**

1.5"

3"

**8 Holes,**
**Tapped w/**
**1/4" - 20**
**(tapped**
**1/2" deep)**
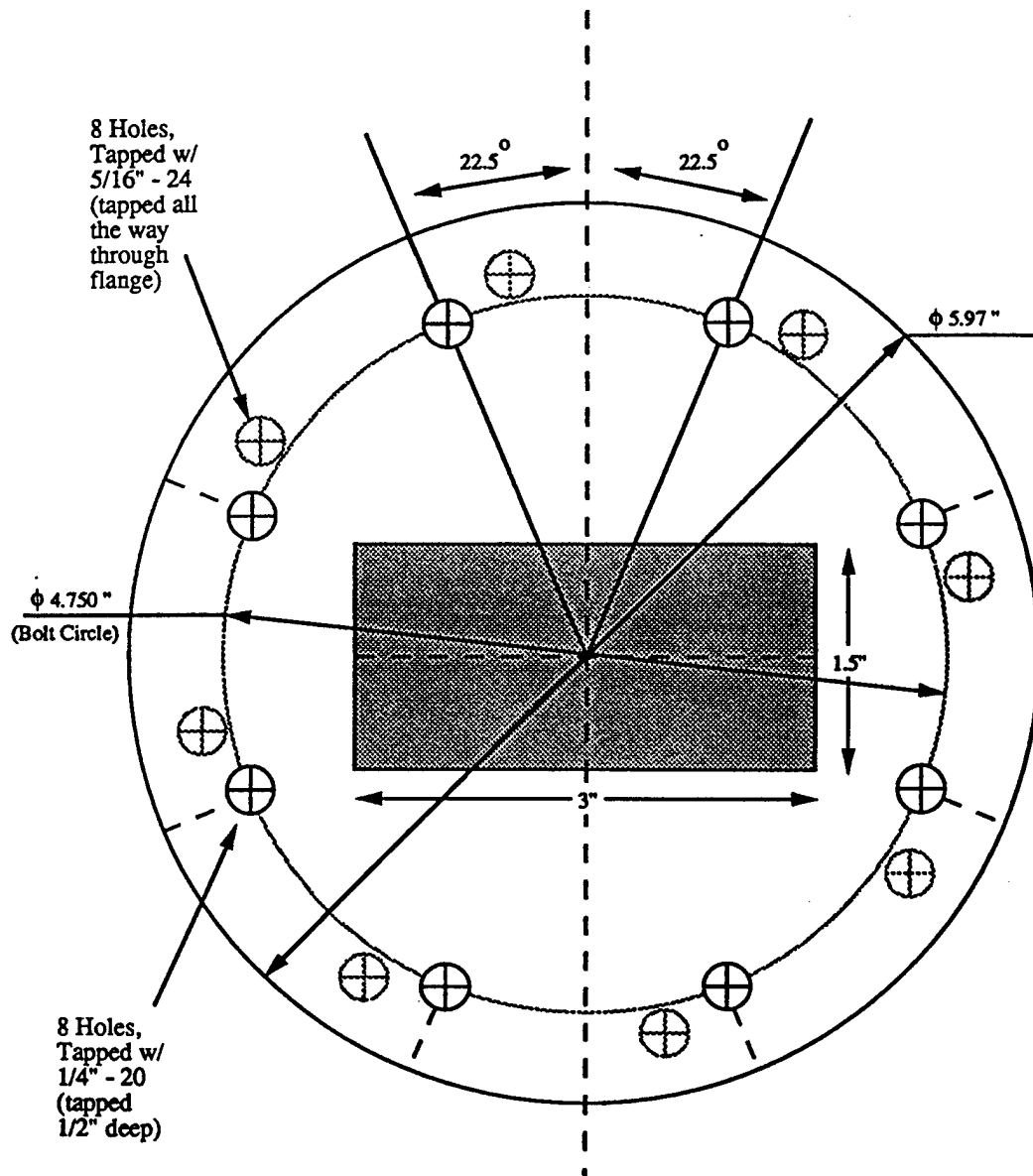
**Figure E.2.   The 'back side' of the Vlasov-antenna adapter flange.**
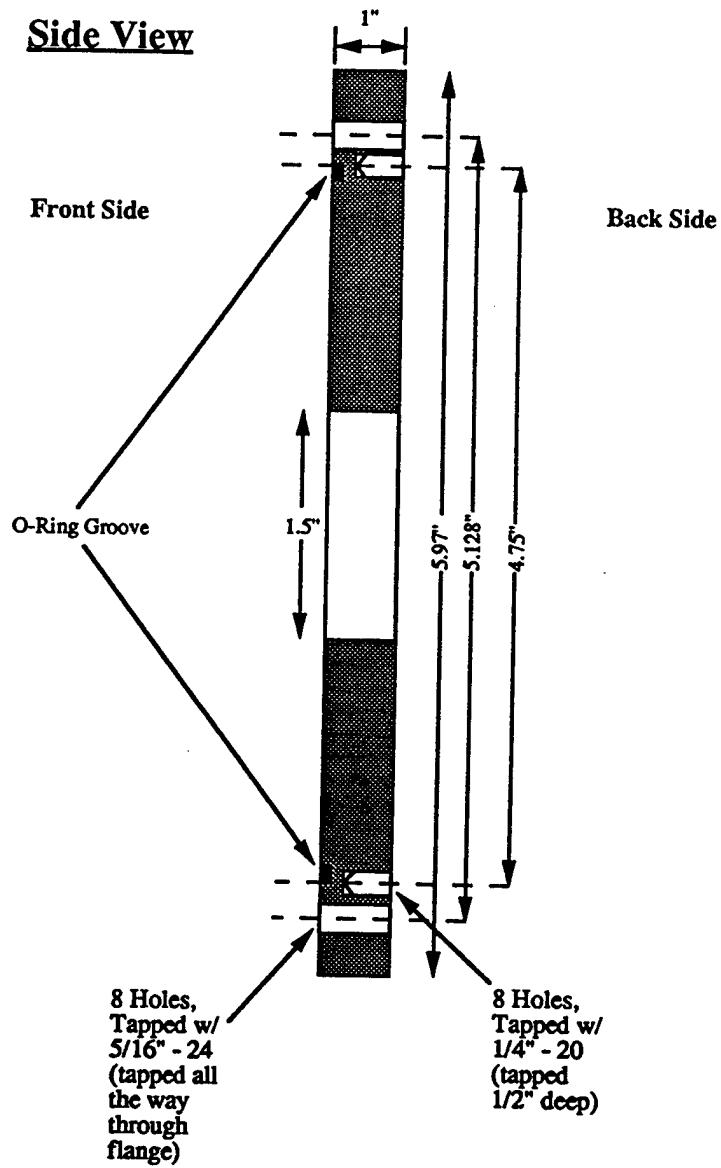
**Figure E.3.** The 'side view' of the Vlasov-antenna adapter flange.

# APPENDIX F

## S-BAND WAVEGUIDE CALIBRATION

The following figures show the S-Band (WR-284) waveguide frequency spectrum calibration.  Figure F.1 shows the S-Band frequency spectrum, and the operating $TE_{10}$ mode frequency of 2.6 to 3.95 GHz.  Figure F.2 shows the frequency spectrum for the 20 dB S-Band directional coupler.  Figure F.3 shows the frequency spectrum for the 30 dB S-Band directional coupler.  Figure F.4 shows the frequency spectrum for two 30 dB S-Band directional couplers connected in series to provide a total of 60 dB S-Band attenuation.  Figures F.2 - F.4 show the uncertainty in the attenuation outside the recommended $TE_{10}$ mode operating frequency range.  Thus the wavguide system depicted in Figure 3.32 which has the recommended $TE_{10}$ mode operating frequency range that matches the frequency range of the experiments was employed.  See Table 3.6 for the specifications of the waveguide detection system used in the gyro-BWO experiments.
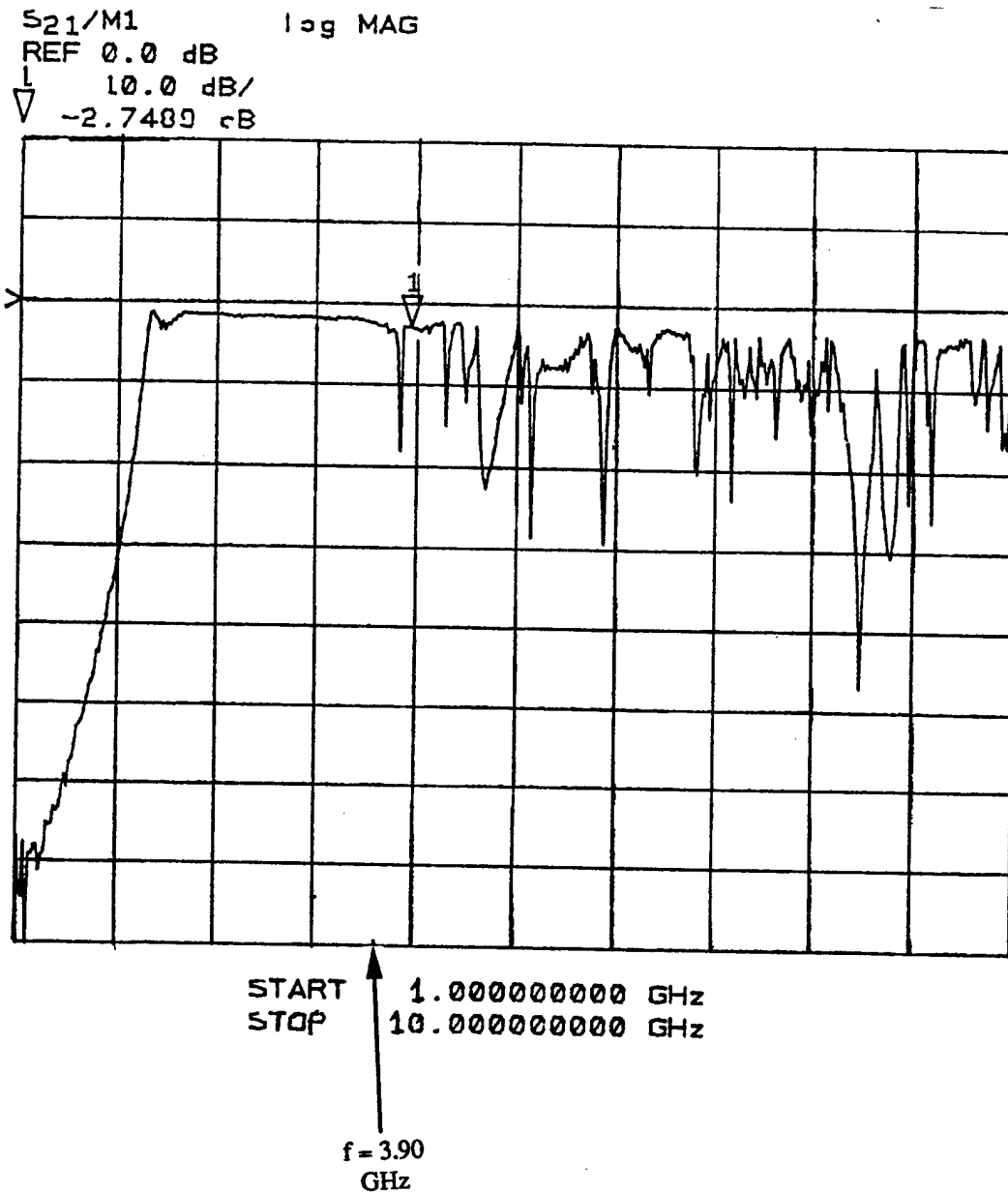
**Figure F.1.  The S-Band frequency spectrum.**

S$_{21}$/M1          log MAG
REF 0.0 dB
1      10.0 dB/
∇   −5.9346 dB

MARKER 1
    4.8925 GHz

START  1.000000000 GHz
STOP  10.000000000 GHz

f = 3.61
GHz
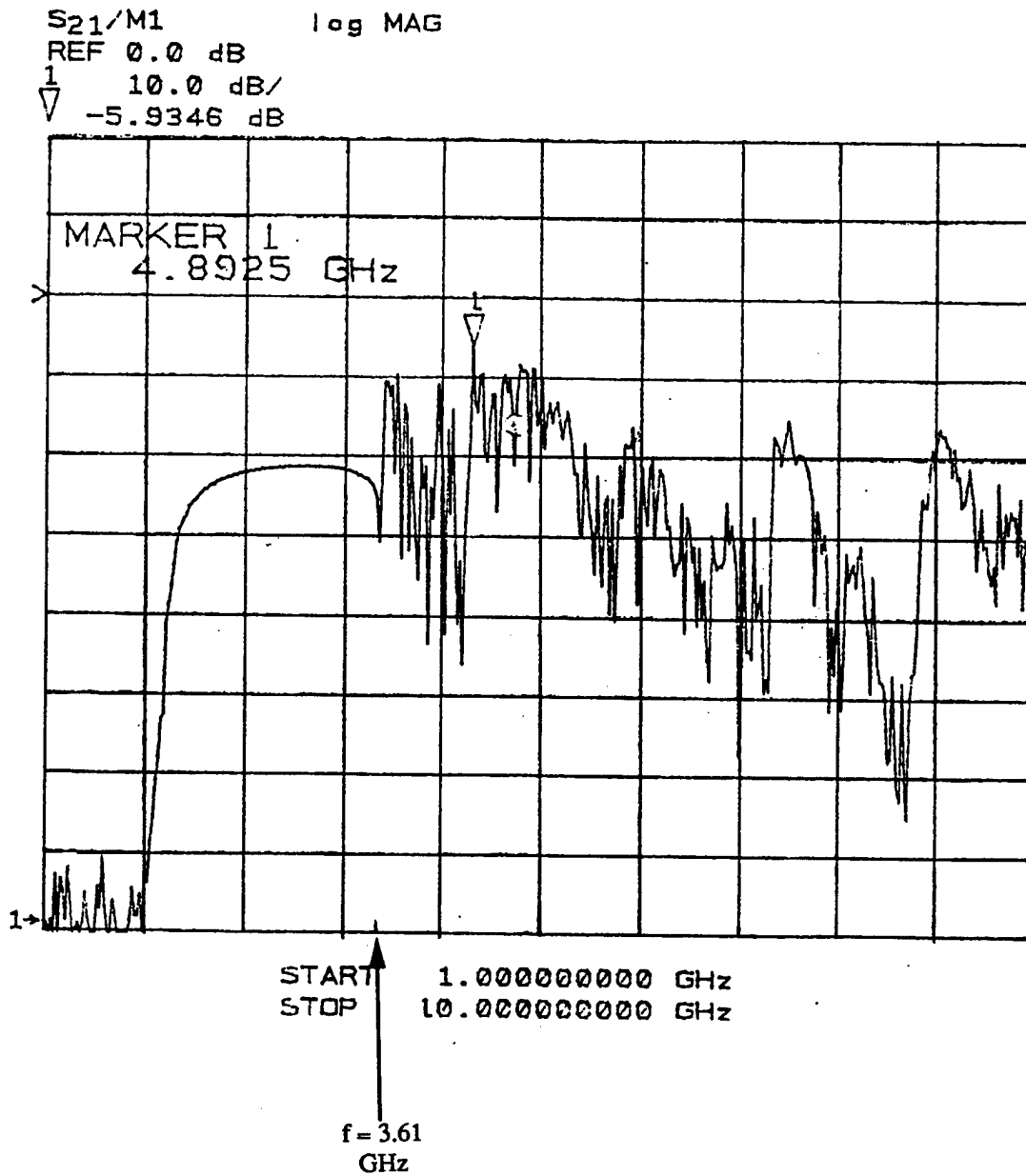
**Figure F.2.  The frequency spectrum for the 20 dB S-Band directional coupler.**

133
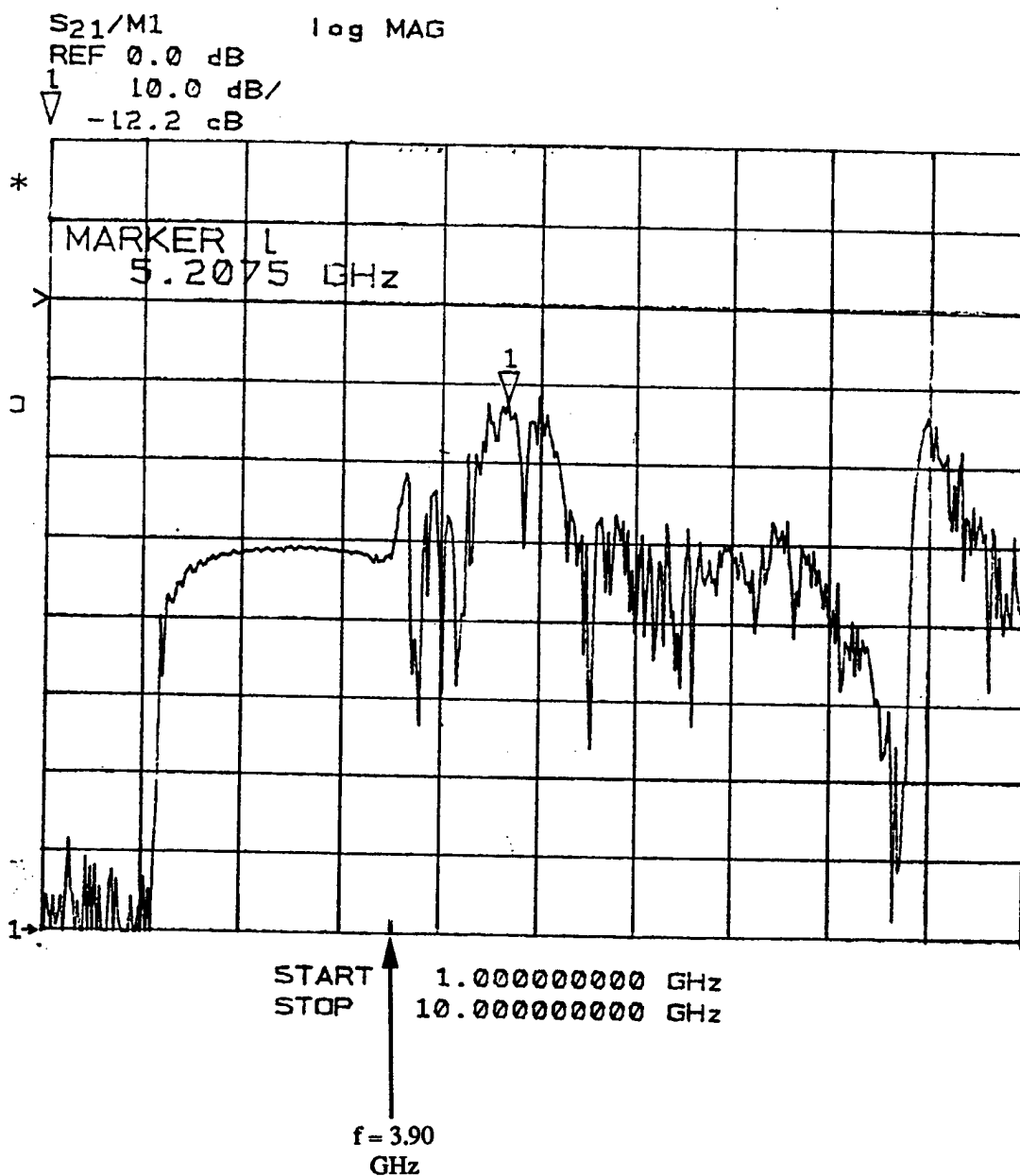


**Figure F.3.   The frequency spectrum for the 30 dB S-Band directional coupler.**

134
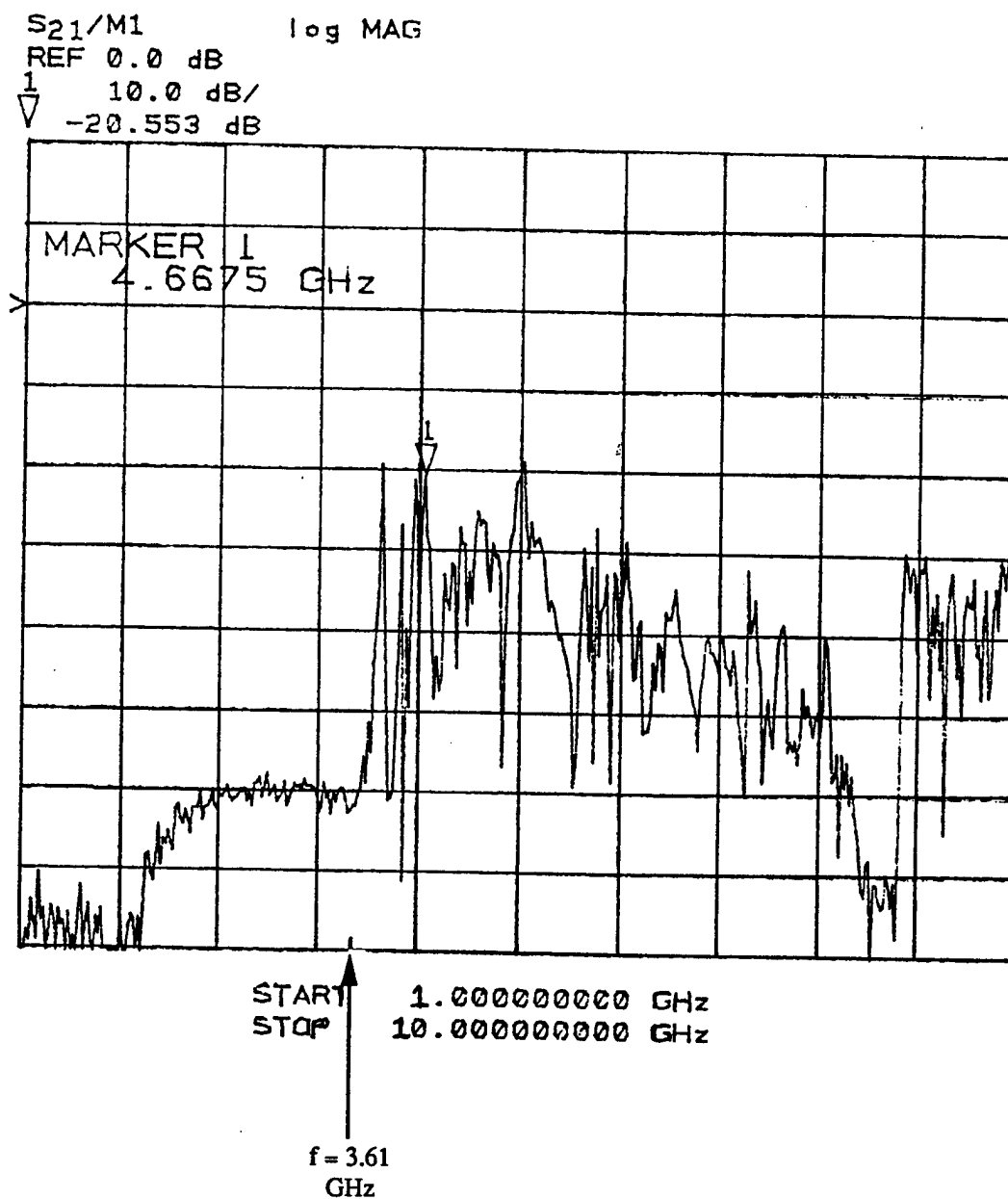


Figure F.4. The frequency spectrum for two 30 dB S-Band directional couplers connected in series to provide 60 dB attenuation.

# APPENDIX G

## FIELD LINES FOR THE TE$_{11}$ AND TE$_{21}$ MODES IN A CYLINDRICAL CAVITY

Figure G.1 shows the electric and magnetic field lines for a cylindrical cavity with radius r.
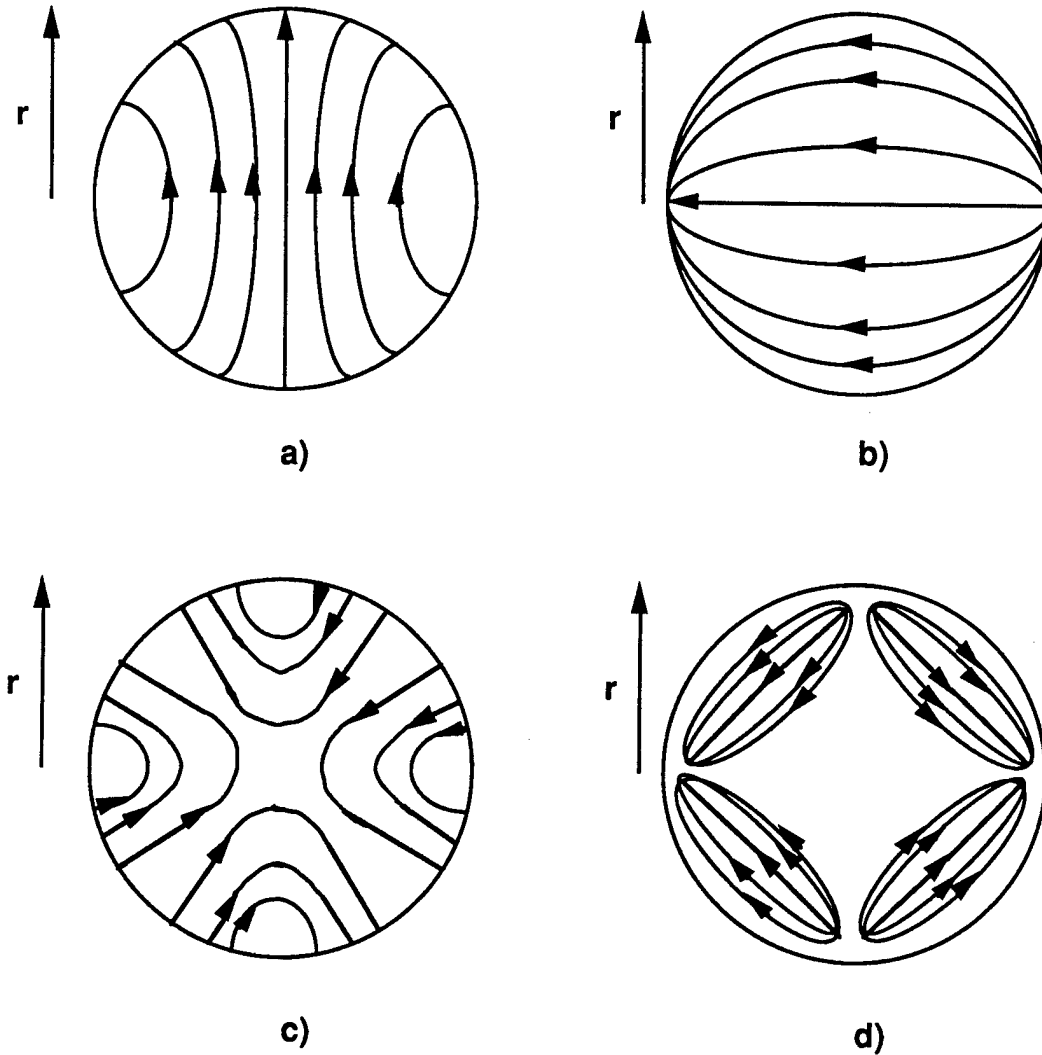


**Figure G.1.** Some of the electric and magnetic field lines for the TE$_{11}$ and TE$_{21}$ modes in a cylindrical cavity of radius r: a) electric field lines for the TE$_{11}$ mode, b) the corresponding magnetic field lines for the TE$_{11}$ mode, c) electric field lines for the TE$_{21}$ mode, and d) the corresponding magnetic field lines for the TE$_{21}$ mode.

# BIBLIOGRAPHY

# BIBLIOGRAPHY

Abr64    Abramowitz, M. , and I. Stegan, *Handbook of Mathematical Functions*, New York: Dover Publications, p. 355, 1964

Abr77    Abramyan, E. A., B. A. Altercorp, and G. D. Kuleshov, "Microsecond Intensive Electron Beams", in *Proc. of the 2nd Int. Topical Conference on High Power Electron and Ion Beam Research and Technology*, Vol. 2, pp. 755 - 760, Oct. 3-5, 1977

And78    Andronov, A. A., V. A. Flyagin, A. V. Gaponov, A. L. Goldenberg, M. I. Petelin, V. G. Usov, V. K. Yulpatov, " The Gyrotron-High-Power Source of Millimetre and Submillimetre Waves", Report for Submillimetre Waves '78, Institute of Applied Physics, The Academy of Sciences of the USSR, Gorky, USSR, pp. 1-21, 1978

Bai87    Baird, J. Mark, "Gyrotron Theory" in *High Power Microwave Sources*, V. L. Granatstein and I. Alexeff, Eds. Norwood, MA: Artech, pp. 103-184, 1987

Bak89    Bakshaev, Yu. L., A. B. Basmonov, P. I. Blinov, B. N. Bragin, and Yu. G. Kalinin, "Evolution of the Structure of Microsecond Relativistic Electron Beams", Sov. J. Plasma Phys., 15 (8), pp. 575-579, August 1989

Bas90    Baston, M. A., W. C. Guss, K. E. Kriescher, R. J. Temkin, M. Caplan, and B. Kulke, "Operation of a 140 GHz Backward-Wave Oscillator", *Fifteenth International Conference on Infrared and Millimeter Wave*, pp. 575-577, 1990

Bek87    Bekefi, G. , A. Dirienzo, C. Leibovitch, and B. G. Danley, "A 35 GHz Cyclotron Autoresonance Maser Amplifier", Appl. Phys. Lett. 54(14), pp. 1302-1304, 1989

Bra73    Bratman, V. L., M. A. Molseev, M. I. Petelin, and R. E. Erm, "Theory of Gyrotrons with a Nonfixed Structure of the High-Frequency Field", Radiofiz., Vol. 16, No.4, pp. 620-630, April 1973

Bra81    Bratman, V. L. , N. S. Ginsburg, G. S. Nusinovich, M. I. Petelin, and P. S. Strelkov, "Relativistic Gyrotrons and Cyclotron Autoresonce Masers", Int. J. Electron., 51(4),.pp. 541-567, 1981

Bra82    Brand, G. F., "Gyrotron or electron cyclotron maser: An introduction", Am. J. Phys., 50(3), pp. 254-258, 1982

Bra87    Bratman, V. L., G. G. Denisov, M. M. Ofitserov, S. D. Korovin, S. D. Polevin, and V. V. Rostov, "Millimeter-Wave HF Relativistic Electron Oscillators", I.E.E.E. Trans. Plasma Sci., PS-15(1), pp. 2-15, 1987

Bra90    Brand, G. F., P. W. Fekete, K. Hong, K. J. Moore, and T. Idehara, "Operation of a tunable gyrotron at the second harmonic of the electron cyclotron frequency", Int. J. Electronics, Vol. 68, No. 6, pp.1099 -1111, 1990

Cap87    Caplan, M., "Design of an Electronically Tunable Millimeter Wave Gyrotron Backward Wave Oscillator," *Twelth International Conference on Infrared and Millimeter Waves*, pp. 276-277, Dec. 14-18, 1987.

Car90a   Carmel, Y., K. Minami, W. Lou, R. A. Kehs, W. W. Destler, V. L. Granatstein, D. K. Abe, and J. Rodgers, "High-Power Microwave Generation by Excitation of a Plasma-Filled Rippled Boundary Resonator", IEEE Trans. on Plasma Sci., Vol. 18, No. 3, pp. 286 - 300, June 1990

Car90b   Carmel, Y., H. Guo, W. R. Lou, D. Abe, V. L. Granatstein, and W. W. Destler, "Novel method for determining the electromagnetic dispersion relation of slow wave structures", Appl. Phys. Lett. 57 (13), pp. 1304-1306, 24 September 1990

Cha73    Chang, T. Y., "Improved Uniform-Field Electrode Profiles for TEA Laser and High-Voltage Applications", Rev. Sci. Inst., Vol. 44, No. 4, pp. 405-408, April 1973

Che89    Chen, C. , and J. S. Wurtele, "Efficiency enhancement in cyclotron autoresonance maser amplifiers by magnetic field tapering", Physical Review A, Vol. 40, No. 1, pp. 489-492, 1 July 1989

Cho91    Choi, Jin Joo, "Bragg Resonator Cyclotron Resonance Maser Experiments Driven by a Microsecond, Intense Electron Beam Accelerator", Ph. D. Dissertation, University of Michigan, 1991

Chu81    Chu, K. R., "Analysis of a basic electron cyclotron maser model", J. of C. I. of Eng., 4(2), pp. 85-90, 1981

Dav89    Davies, J. A., "Condition for absolute instability in the cyclotron resonance maser", Phys. Fluids B, 1(3) pp. 663-669, 1989

Dav90    Davies, J. A., R. C. Davidson, and G. L. Johnston, "Pulse Shapes For Absolute and Convective Cyclotron-Resonance-Maser Instabilities", IEEE Trans. on Plasma Sci., Vol. 18, No. 3, pp. 286 - 300, June 1990

Did76    Didenko, A. N. , A. G. Zherlitsyn, V. I. Zelentsov, A. S. Sulakshin, G. P. Fomenko, Yu. G. Shtein, and Yu. G. Yushkov, "Generation of Gigawatt microwave pulses in the nanosecond range", Sov. J. Plasma Phys., Vol. 2, No. 3, pp. 283-285, May-June 1976

Fli86    Fliflet, A. W. , "Linear and Non-Linear Theory of the Doppler-Shifted Cyclotron Resonance Maser Based on TE and TM Waveguide Modes", Int. J. Electron. , 61(6) , pp. 1049-1080, 1986

Fli88    Fliflet, A. W., S. H. Gold, and W. M. Manheimer, "Design of a High Voltage Multi-Cavity 35 GHz Phase-Locked Gyrotron Oscillator", NRL Memorandum Report 6065, pp.1-46, 1 November 1988

Fly77       Flyagin, V. A. , A. V. Gaponov, M. I. Petelin, and V. K. Yulpativ, "The Gyrotron", IEEE Trans. MTT-25, pp. 514-527, June 1977

Fri72a      Friedman, M. and M. Herndon, "Microwave Emission Produced by the Interaction of an Intense Relativistic Electron Beam with a Spatially Modulated Magnetic Field", Phys. Rev. Lett., Vol. 28, No. 4, pp. 210-212, 24 January 1972

Fri72b      Friedman, M., and M. Herndon, "Emission of Coherent Microwave Radiation from a Relativistic Elecron Beam Propagating in a Spatially Modulated Field", Phys. Rev. Lett., Vol. 29, No. 1, pp. 55-58, 3 July 1972

Fri73       Friedman, M. , D. A. Hammer, W. M. Manheimer, and P. Sprangle, "Enhanced Microwave Emission Due to the Transverse Energy of a Relativistic Electron Beam", Physical Review Lett. Vol. 31, No. 12, pp. 752-755, 17 September 1973

Gan89       Ganguly, A. K., and S. Ahn, "Optimization of the efficiency in gyrotron backward-wave oscillator via a tapered axial magnetic field", Appl. Phys. Lett. 54 (6), pp. 514-516, 6 February 1989

Gap59       Gaponov, A. V., Addendum. Izvestiya VUZ. Radiofizika, 2, p. 837, 1959

Gil80       Gilgenbach, R. M., M. E. Read, K. E. Hackett, R. F. Lucey, Jr., B. Hui, V. L. Granatstein, and K. R. Chu, "Heating at the electron cyclotron frequency in the ISX-B tokamak," Phys. Rev. Lett. 44 (10), pp. 647 - 650, 1980.

Gil81       Gilgenbach, R. M., M. E. Read, K. E. Hackett, R. F. Lucey, Jr., V. L. Granatstein, A. C. England, C. M. Loring, J. B. Wilgen, R. C. Isler, Y-K. M. Peng, K. H. Burrell, O. C. Eldridge, M. P. Hacker, P. W. King, A. G. Kulchar, M. Murakami, and R. K. Richards, "Electron cyclotron/upper hybrid resonant pre-ionization in the ISX-B tokamak," Nuclear Fusion 21 (3), pp. 319 - 327, 1981.

Gil85       Gilgenbach, R. M., L. D. Horton, R. F. Lucey, Jr., S. Bidwell, M. Cuneo, J. Miller, and L. Smutek, "Microsecond Electron Beam Diode Closure Experiments", in Digest of Technical Papers of the Fifth IEEE Pulsed Power Conference, 1985

Gin79       Ginzburg, N. S., V. I. Krementsov, M. I. Petelin, P. S. Strelkov, and A. K. Shkvarunets, "Experimental investigation of a high-current relativistic cyclotron maser", Sov. Phys. Tech. Phys 24(2), February 1979

Gin81       Ginzburg, N. S., I. G. Zarnitsyna, and G. S. Nusinovich, "Theory of relativistic cyclotron resonance maser amplifiers", Radiophys. Quant. Electon., 24, pp. 331-338, 1981

Gol87       Gold, S. H., A. W. Fliflet, W. M. Manheimer, R. B. McCowan, W. M. Black, R. C. Lee, V. L. Granatstein, A. K. Kinkead, D. L. Hardesty, and M. Sucy,"High Peak Power Ka-Band Gyrotron Oscillator Experiment", Phys. Fluids 30(7), pp. 2226-2238, July 1987

Gra82    Granatstein, V. L., M. E. Read, and L. R. Barnett, "Measured Performance of Gyrotron Oscillators and Amplifiers" in *Infrared and Millimeter Waves*, Vol. 5 "Coherent Sources and Applications Part I", Ed. Kenneth J. Burton, New York, Academic Press, pp. 267-304, 1979

Gra87    Granatstein, V. L. , "Gyrotron Experimental Studies", in *High Power Microwave Sources*, V. L. Granatstein and I. Alexeff, Eds. Norwood, MA: Artech, pp. 185-206, 1987

Gus89    Guss, W. C., K. E. Kriescher, R. J. Temkin, M. Caplan, and D. Pirkle, "Operation of a 140 GHz Tunable Backward Wave Gyrotron Oscillator," *Fourteenth International Conference on Infrared and Millimeter Wave*, pp. 369-370, 1989.

Har61    Harrington, R. F. , *Time-Harmonic Electromagnetic Fields*, McGraw-Hill, New York, 1961

Hem79    Hermannsfeldt, W. B. , "Electron Trajectory Program", SLAC-226, 1979

Hir64    Hirshfield, J. L., and J. M. Wachtel, "Electron Cyclotron Maser", Phys. Rev. Lett., 12(19), pp. 533-536, 1964

Hir77    Hirshfield, J. L., and V. L. Granatstein, "The Electron Cyclotron Maser - An Historical Survey", IEEE Trans. Microwave Theory And Techniques, pp. 522-527, June 1977

Hir79    Hirshfield, J. L., "Gyrotrons" in *Infrared and Millimeter Waves*, *Vol. 1*, Academic Press, pp. 1-54, 1979

Hum86    Humfries, Stanley, Jr. , *Principles of Charged Particle Acceleration*, New York: John Wiley & Sons, New York, 1975

Ide91    Idehara, T., T. Tatsukawa, I. Ogawa, T. Mori, S. Wada, G. F. Brand, and M. H. Brennan, "Competition between fundamental and second-harmonic operations in a submillimeter wave gyrotron", Appl. Phys. Lett. **58** (15), pp. 1594-1596, 15 April 1991

Jac75    Jackson, J. D. , "Classical Electrodynamics", Second Addition, John Wiley & Sons, New York, 1975

Kan79    Kantorowicz, G. and P. Palluel, "Backward Wave Oscillators", in *Infrared and Millimeter Waves, Vol. I*, Academic Press, pp. 185-212, 1979

Kho88    Kho, T. H., A. T. Lin, and Liu Chen, "Gyrophase-Coherent Electron Cyclotron Maser", Phys Fluids **31**(10), pp. 3120-3126, October 1988

Kho90    Kho, T. H., and A. T. Lin, "Efficiency Dependence on beam current and input power in a cyclotron autoresonance maser amplifier", Phys. Fluids B **2** (4), pp. 822-827, April 1990

Kra86    Krall, N. A. , and A. W. Trivelpiece, "Principles of Plasma Physics", New York: McGraw-Hill, 1986

Kre78    Krementsov, V. I., M. I. Petelin, M. S. Rabinovich, A. A. Rukhadze, P. S. Strelkov, and A. G. Shkvarunets, "Plasma-filled gyrotron with a relativistic supervacuum electron beam", Sov. Phys. JETP 48(6), pp. 1084-1085, December 1978

Kuo88    Kuo, S. P., K. K. Tiong, P. E. Miller, and W. Namkung, "A Comparative Study for an eigth harmonic cusptron tube operarting in the $\pi$ mode and $2\pi$ mode", Phys. Fluids 31 (6), pp. 1821-1823, June 1988

Lau81    Lau, Y.Y., K. R. Chu, L. R. Barnett, and V. L. Granatstein, "Gyrotron Traveling Wave Amplifier: I. Analysis of Oscillations," *Inter. J. Infr. and Millimeter Waves* , Vol. 2, No. 3, pp. 373-393, 1981.

Lau87    Lau, Y. Y., "Theory of Cross Field Devices and a Comparative Study of Other Radiation Sources", NRL Memorandum Report 6029, pp. 1-60, 21 July 1987

Law91    Lawson, W., J. P. Calame, B. Hogan, P. E. Latham, M. E. Read, V. L. Granatstein, M. Reiser, and C. D. Striffler, "Efficient Operation of a High Power X-BAnd Gyroklystron", submitted to Phys. Rev. Lett., 1991

Lee88    Lee, J. K., W. D. Bard, S. C. Chiu, R. C. Davidson, and R. R. Goforth, "Self-Consistent nonlinear evolution of the cyclotron autoresonance maser", Phys. Fluids 31 (6), pp. 1824-1826, June 1988

Lei86    Leifeste, Gordon T., Lawrence M. Earley, John A. Swegle, James W. Poulkey, R. Bruce Miller, Charles E. Crist, Charles B. Wharton, and William P. Ballard, "*Ku*-band radiation produced by a relativistic backward wave oscillator", J. Appl. Phys. 59 (4), pp. 1366-1378, 15 February 1986

Lin87    Lin, Anthony T., K. R. CHu, and A. Bromborsky, "The Stability and Tunabilty of a CARM Amplifier", I.E.E.E. Trans. Electron Devices, Vol. ED-34, No. 12, pp. 2621-2624, December 1987

Luc88    Lucey, R. F., "Long-Pulse Relativistic Electron Beam Generation and Propagation in Gases and in UV Laser Ionized Channels", Ph. D. Thesis, University of Michigan, 1988

McC91    McCurdy, A. H., and C. M. Armstrong, "Mode selection by priming in an overmoded electron cyclotron maser", Phys. Fluids B 3 (1), pp. 212 - 227, January 1991

Mic89    Microsoft Excel 2.2, *Microsoft Excel Reference*, Microsoft Corporation, Document Number AB0202-220-R00-0289, 1989

Mil82    Miller, R. B. , *An Introduction to the Physics of Intense Charged Particle Beams*, Plenum Press, New York, 1982

Par73    Parker, R. K., "Explosive Electron Emission and the Characteristics of High Current Electron Flow", Ph. D. Thesis, University of New Mexico, 1973

Par74    Parker, R. K., R. E. Anderson, and C. V. Duncan, "Plasma-induced field emission and the characteristics of high current flow", J. Appl. Phys., Vol. 45, No. 6, pp. 2463-2479, June 1974

Par84    Park, S. Y., V. L. Granatstein, R. K. Parker, "A Linear Design Study for a Gyrotron Backward-Wave Oscillator," Int. J. Electron., Vol. 57, pp. 1109-1123, 1984.

Par90    Park, S. Y., R. H. Kyser, C. M. Armstrong, R. K. Parker, and V. L. Granatstein, "Experimental Study of a $Ka$-Band Gyrotron Backward-Wave Oscillator", I.E.E.E. Trans. Plasma Sci., PS-18(3), 321-324, June 1990

Pen91    Pendergast, K. D., B. G. Danly, and R. J. Temkin, "Operation of a Long-Pulse CARM Oscillator", Submitted to Nuclear Instruments and Methods (special issue) 1991

PSI83    Pulse Sciences Report, "Electron Beam Accelerator", PSI-P-83-105, 7/84

Ram65    Ramo, S., J. R. Whinnery and T. Van Duzer, *Fields and Waves in Radio Communications*, John Wiley and Sons, New York, 1965

Rea80    Read, Michael E., Ronald M. Gilgenbach, Robert F. Lucy, Jr., Kwo Ray Chu, Adam T. Drobot, and Victor L. Granatstein, "Spatial and Temporal Coherence of a 35-GHz Gyromonotron Using the $TE_{01}$ Circular Mode", I.E.E.E. Trans Microwave Theory and Techniques, Vol. MTT-28, No. 8, pp. 875-878, August 1980

Saa71    Saad, T. S. editor, *Microwave Engineers' Handbook Volume I*, Artech House, Inc. 1971

Sch59    Schneider, J., "Stimulated emission of radiation by relativistic electrons in a magnetic field", Phys. Rev. Lett., 2(12), pp. 504-505, 1959

She81    Shefer, R. E., and G. Bekefi, "Cyclotron Emission from Intense Relativistic Electron Beams in Uniform and Rippled Magnetic Fields", Int. J. Electron., 51(4), 569-582, 1981

Shi89    Shiffler, D., John A. Nation, and C. B. Wharton, "High-power traveling-wave amplifier", Appl. Phys. Lett. 54 (7), pp. 674-676, 13 February 1989

Sul87    Sullavin, D. J., J. E. Walsh, and E. A. Coutsias, "Virtual Cathode Oscillator (VIRCATOR) Theory" in *High Power Microwave Sources*, V. L. Granatstein and I. Alexeff, Eds. Norwood, MA: Artech, pp. 441-505, 1987

Swe85    Swegle, John A., James W. Poulkey, and Gordon T. Leifeste, "Backward wave oscillators with rippled wall resonators: Analytic theory and numerical simulation", Phys. Fluids 28 (9), pp. 2882-2894, September 1989

Tho87    Thode, L. E., "Vitual-Cathode Microwave Device Research: Experiment and Simulation", in *High Power Microwave Sources*, V. L. Granatstein and I. Alexeff, Eds. Norwood, MA: Artech, pp. 507 - 562, 1987

Twi58    Twiss, R.Q., "Radiation Transfer and the Possibility of Negative Absorption in Radio Astronomy", Aust. J. Phys., **11**, pp. 564-579, 1958

Vor82    Voronkov, S. N., V. I. Krementsov, P. S. Strelkov, and A. G. Shkvarunets, "Stimulated Cyclotron Radiation at Millimeter Wavelengths from a High-Power Relativistic Electron Beam", Sov. Phys. Tech. **27** (1), pp.68-69, January 1982

Wac80    Wachtel, J. M., and E. J. Wachtel, "Backward wave oscillation in the gyrotron", Appl. Phys. Lett. **37** (12), pp. 1059-1061, 15 December 1980

Wan89    Wang, J. G., "Frequency-Tunable, High Power Microwave Emission From A Cyclotron Autoresonance Maser Oscillator", Ph. D. Dissertation, University of Michigan, 1989.